12-2013

Wide-area measurement and applications in power system dynamic modeling and control

Yong Liu
University of Tennessee - Knoxville, yliu66@utk.edu

To the Graduate Council:

I am submitting herewith a dissertation written by Yong Liu entitled "Wide-area measurement and applications in power system dynamic modeling and control." I have examined the final electronic copy of this dissertation for form and content and recommend that it be accepted in partial fulfillment of the requirements for the degree of Doctor of Philosophy, with a major in Electrical Engineering.

Yilu Liu, Major Professor

We have read this dissertation and recommend its acceptance:

Fangxing Li, Kai Sun, Joshua Fu

Accepted for the Council:

Carolyn R. Hodges

Vice Provost and Dean of the Graduate School

(Original signatures are on file with official student records.)

Wide-area measurement and applications in power system dynamic modeling and control

A Dissertation Presented for the
Doctor of Philosophy
Degree
The University of Tennessee, Knoxville

Yong Liu
December 2013

ACKNOWLEDGEMENTS

First and foremost, I would like to express my sincere gratitude to my advisor, Dr. Yilu Liu for her patient guidance and consistent encouragement in my academic and personal life. I cannot be luckier to have Dr. Liu as my Ph.D. advisor.

Next, thanks go to Dr. Fangxing Li, Dr. Kai Sun and Dr. Joshua Fu for their serving in my Ph.D. committee. I greatly appreciate their suggestions and comments on this dissertation.

Then, thanks are extended to all those graduated and current Power IT lab colleagues, for their consistent friendships and valuable suggestions. I am especially thankful for the patient help from Dr. Yingchen Zhang, Dr. Lang Chen, Dr. Yanzhu Ye, Dr. Zhenzhi Lin, Dr. Yuming Liu, Dr. Ke Zhang and Dr. Changgang Li. I also truly enjoy the friendship with Ye Zhang, Yong Jia, Lingwei Zhan, Gefei Kou, Jiahui Guo, Jidong Chai, Yin Lei, Dao Zhou, and so many other wonderful colleagues in the Power IT lab.

Finally, I would like to express my deepest love to my family: my father Fuhong Liu, my mother Aiying Wang, my sister Ling Liu, and my wife Chen Zhang, for their endless love and support.

ABSTRACT

Synchrophasor has been becoming the foundational element of power grid wide-area measurement system (WAMS) since first developed in 1980s. By utilizing global positioning system (GPS) time synchronization technique, synchrophasors offer highly accurate time-synchronized phasor measurements that can provide system operators with real-time information of operation status.

Frequency disturbance recorders (FDRs) are installed on the distribution level to measure power system dynamics and considered as a type of single-phase synchrophasors. In this dissertation, a detailed procedure for the FDRs' calibration is summarized and a preliminary test of their dynamic performance is carried out. Moreover, this dissertation investigates the impact of GPS signal availability on the FDR's measurement accuracy and demonstrates that high-sensitivity GPS receiver provides a more reliable timing for synchrophasors.

Among the various applications of synchrophasor measurements, wide-area control of renewable energy sources (such as the variable-speed wind generators and solar photovoltaic (PV) generators) for frequency regulation and inter-area oscillation damping has attracted significant attentions. In this dissertation, based on the user-defined wind/PV generator electrical control model and the 16,000-bus Eastern Interconnection (EI) dynamic model, the additional controllers for frequency regulation and inter-area oscillation damping are developed and the potential contributions of renewables to the EI system frequency regulation and inter-area oscillation damping are evaluated.

Measurement-based power system modeling is another important application of synchrophasor measurements, especially considering the fact that only a limited number of transfer functions or models are critical to system stability evaluation and real-time control. In this dissertation, how to construct a measurement-based power system dynamic model is discussed. Based on a linear model structure, a concept of dynamic response estimation is proposed and its overall performance is examined. Identifying

angular and voltage instability issues is also explored in this dissertation as an example of this measurement-based model's applications.

TABLE OF CONTENTS

LIST OF TABLES

LIST OF FIGURES

Chapter 1 INTRODUCTION OF FREQUENCY MONITORING NETWORK (FNET)

1.1 Frequency Monitoring Network Framework

As an academia-run wide-area measurement system (WAMS) of the power grids, frequency monitoring network (FNET) at the University of Tennessee, Knoxville (UTK) has been continuously providing the independent real-time observation of the main electric power grids in the world since 2003 [1]-[3].

As depicted in Figure 1-1, the FNET system consists of two major components: a) hundreds of frequency disturbance recorders (FDRs), the ground-level sensors that perform the GPS-synchronized power system phasor measurements and send data to the server through the Internet, and b) the information management system (IMS), which includes data collection and storage service, data communication service, database operation service, and web services.

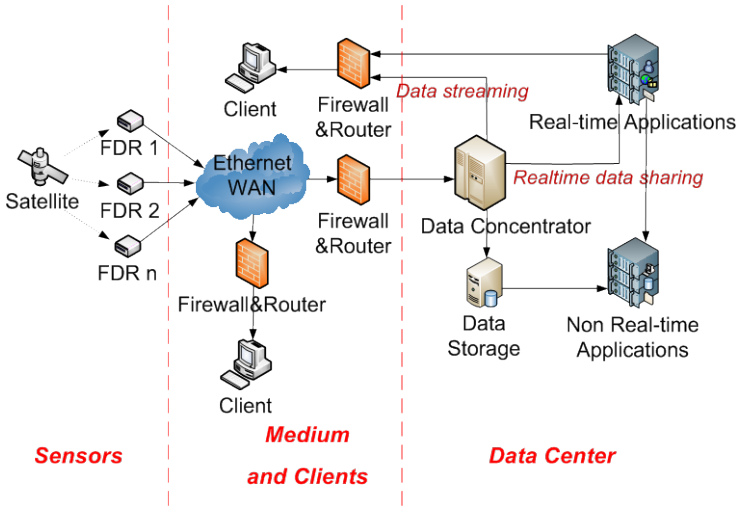

Figure 1-1 FNET Architecture

1.2 Frequency Disturbance Recorder

The sensors FNET uses to capture the electric power grid dynamics (frequency, voltage and phase angle) are essentially one type of the single-phase synchrophasors and usually referred to as frequency disturbance recorders (Figure 1-2). Since the FDR sensors are installed on the distribution level (120 V in the U.S.), they do not require the extensive installation efforts as what phasor measurement units (PMUs, the commercial version of synchrophasors) need at the high voltage substations. FDR sensors are low-cost, easy to install, and thus are widely installed in offices, residential households and renewable generation sites of North America, Europe, East Asia and Brazil (Sensor deployment map is given in Figure 1-3).

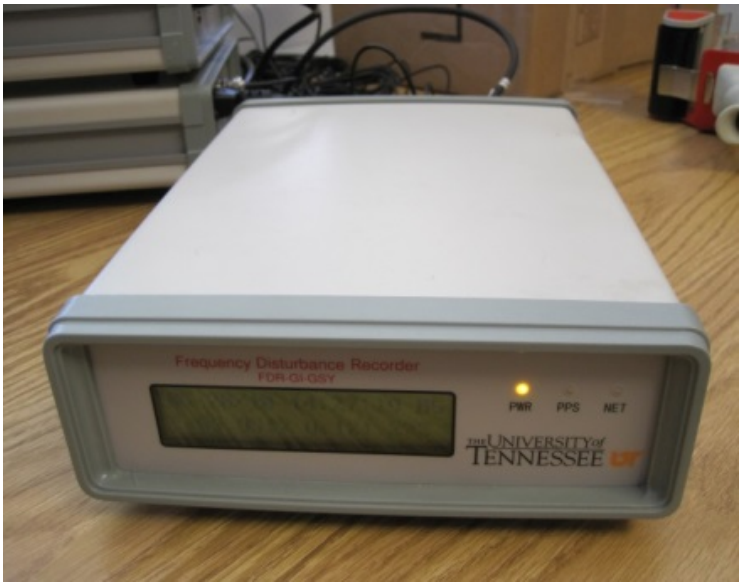

Figure 1-2 Second-Generation FDR

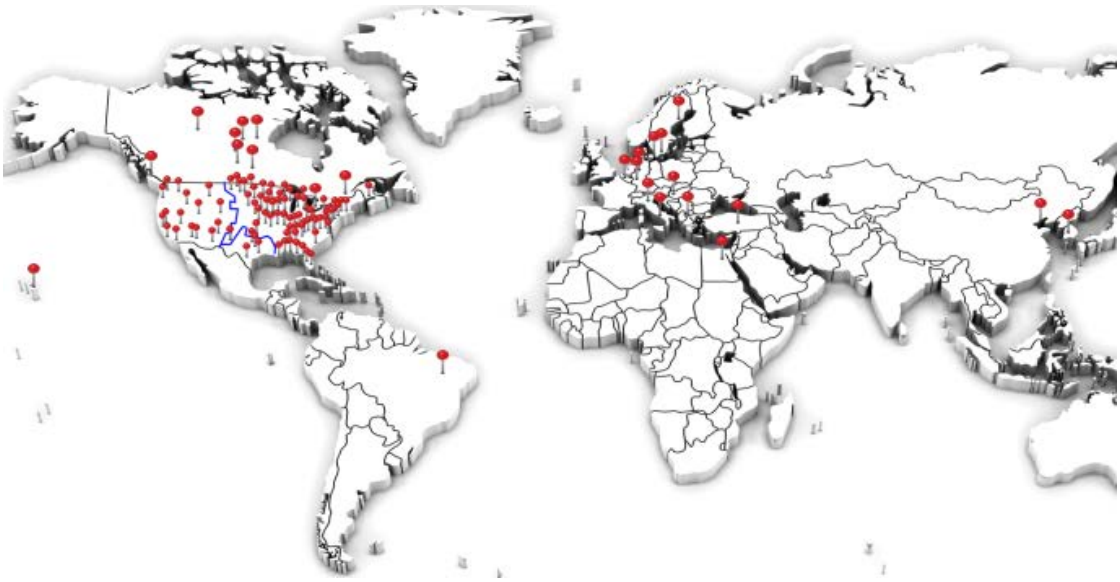

Figure 1-3 World-wide Deployments of FDRs

Chapter 2 FREQUENCY DISTURBANCE RECORDER CALIBRATION AND TEST

2.1 Hardware Structure of Frequency Disturbance Recorder

Compared to its commercial counterparts, the FDR's hardware structure is relatively simple, which consists of a step-down voltage transformer, an analog low-pass filter, an analog to digital (A/D) converter, a GPS receiver, a microcontroller, a digital signal processor (DSP) and a network communication module, as shown in Figure 2-1.

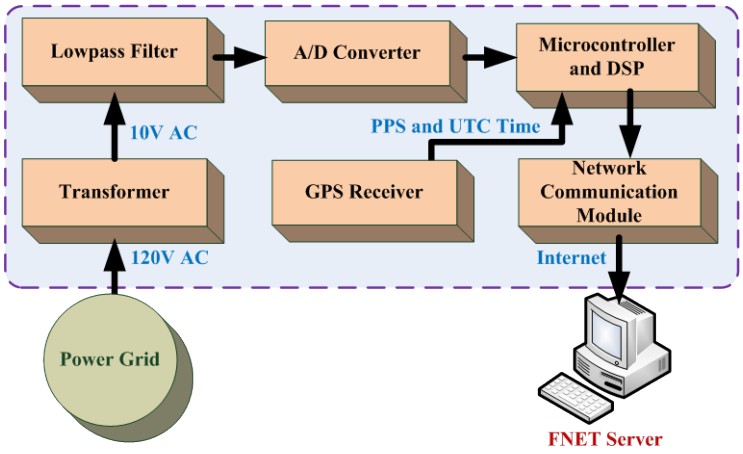

Figure 2-1 FDR Hardware Structure

PMUs are usually installed in the high voltage substations (110 kV and above) and thus high-precision potential transformer (PT) or current transformer (CT) is indispensable to attenuate the kV-level voltage or kA-level current to 100 V or 5 A in order for voltage or current measurement. Comparatively, as a low-cost synchrophasor deployed on the distribution level, the FDR only needs a simple step-down voltage transformer to take the voltage waveform from the 110 V wall outlets. Then, the analog low-pass filter inside the FDR eliminates the high-frequency components of the voltage waveform, and the A/D

converter transforms the analog signal into digital. The microcontroller is used to generate the sampling pulses that are synchronized to the pulse per second (PPS) signal from the GPS receiver and then, the phase angle, frequency, and voltage magnitude are all computed in the digital signal processor. As the last step, the computed values are time-stamped in the microcontroller, packaged (maybe also encrypted) in the network communication module and then transmitted to the data server via the Internet.

2.2 Calibration of Frequency Disturbance Recorder

The technical specifications of the second-generation FDR are listed in Appendix A. In order to make sure all the FDRs meet the same measurement accuracy criteria, the calibration process need to be carefully carried out before the actual field installation. In this section, three aspects of calibrations, including "saw teeth" calibration, voltage magnitude calibration and voltage angle calibration, will be introduced respectively.

1) Saw Teeth

For the second-generation FDRs, the sampling rate of the voltage waveform signal is 1440/s while the clock frequency of the microcontroller is 30 Million/s. Therefore, the number of clock pulses in each sampling period can be calculated as:

$$\boldsymbol{N_{clkpus\_sampling} = floor\left(\frac{N_{clkpus\_PSS}}{M}\right) = floor\left(\frac{30{,}000{,}000}{1440}\right) = 20833} \qquad 2\text{-}1$$

$N_{clkpus\_sampling}$ is the number of clock pulses between two adjacent samplings, N_{clkpus_PPS} is the number of the system clock pulses within one second (between two adjacent PPS signals), and M is the voltage waveform sampling rate. $floor(N_{clkpus\_PSS}/M)$ stands for the largest integer that's smaller than N_{clkpus_PSS}/M. Obviously, a residue of 480 clock pulses exists in the end of each second, since N_{clkpus_PPS} cannot be divided by M, as shown below:

$$\boldsymbol{Residue = 30{,}000{,}000 - (1440 * 20833) = 480} \qquad 2\text{-}2$$

This residue amounts to 16 μs for the second-generation FDR. Though it appears to be negligible, it results in the accumulation of measurement error and the sudden change of the voltage angle measurement (referred to as "saw teeth") in the end of each second due to the correction effect of a new PSS signal. Luckily, considering that the angle "saw teeth" error within each second is fixed and also proportional to the output data point number within each second (which is the number of tenths of a second since the output rate is 10/s), the errors can be calculated and eliminated. Note that a constant frequency deviation from the nominal value also causes the angle measurements to increase/decrease linearly. Therefore, the effect of frequency deviation must be taken into account during the calibration process.

The illustration of the "saw teeth" error in the presence of a constant frequency deviation is given in Figure 2-2. The solid line is the original angle measurement with "saw teeth", and the dashed line is the actual angle value. This calibration process is to bring the measurement from the solid line to the dashed line. For example, the original measurement point $10k + 6$ needs to be moved to the corresponding dot on the dashed line after the calibration, as directed by the arrow in Figure 2-2. In other words, the slope difference between the solid line and the dashed line β needs to be eliminated within each second. From Figure 2-2, it is easy to see that the slope difference β can be obtained by adding the slope of the solid line χ and the slope of the dashed line α, which can be calculated by the following equations:

$$\boldsymbol{\chi} = \frac{\boldsymbol{Angle}[\mathbf{10}\boldsymbol{k}+\mathbf{9}]-\boldsymbol{Angle}[\mathbf{10}\boldsymbol{k}]}{\mathbf{9}} \quad 2\text{-}3$$

$$\boldsymbol{\alpha} = \frac{\boldsymbol{Angle}[\mathbf{10}(\boldsymbol{k}+\mathbf{1})]-\boldsymbol{Angle}[\mathbf{10}\boldsymbol{k}]}{\mathbf{10}} \quad 2\text{-}4$$

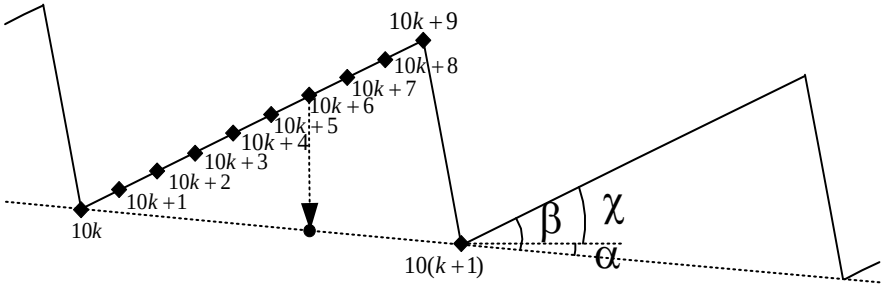

Figure 2-2 “Saw Teeth” Issue and Its Correction

After the slope difference β is obtained, for the $k\,th$ output data point within each second, subtract $k\beta$ from the original value to obtain the calibrated angle value. In this way, the “saw teeth” issue can be addressed. As shown in Figure 2-3, the “saw teeth” within each second can be noticed on the angle curves of the PSU and Bismarck FDRs that are not calibrated. However, they are no longer noticeable on the angle curves of ARI, FSU, and ISONE FDRs, which have been calibrated before their installations. Thus, it proves that the “saw teeth” problem can be satisfactorily resolved by the technique mentioned above.

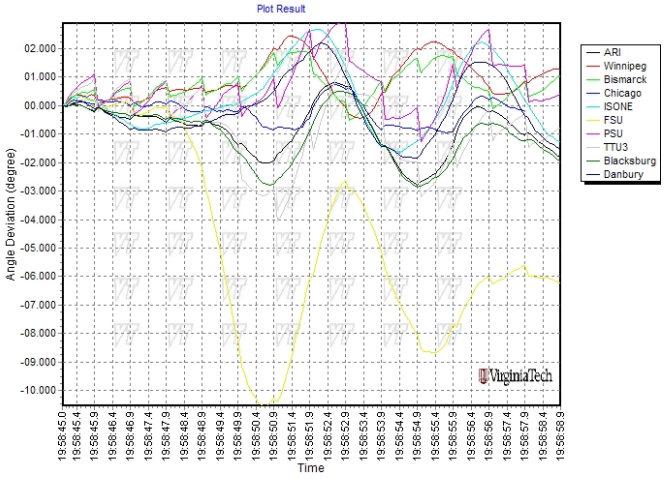

Figure 2-3 Result of “Saw Teeth” Elimination

2) Voltage Magnitude Coefficient

Due to the difference between the electronic circuits, it is also necessary to calibrate the voltage magnitude in the calculation process. If a standard 120 V/60 Hz/0° voltage source is connected to the FDRs during the calibration process, the voltage magnitude measurements V_i $(i = 1,2, \dots, n)$ can be collected during a period of time and the voltage magnitude correction coefficient V_{coff} can be calculated by

$$\boldsymbol{V_{coff} = \frac{120n}{\sum_{i=1}^{n} V_i}} \qquad 2\text{-}5$$

where n is the number of total measurement points. Then, the algorithm is modified in the DSP through multiplying the original voltage magnitude measurement by V_{coff} to obtain the calibrated measurement. Figure 2-4 shows the voltage magnitudes measured by one FDR before and after calibration. The original voltage measurement is around 119.934 V, and then the voltage magnitude coefficient can be calculated by Equation 2-5 and is equal to 1.00055. As seen from Figure 2-4, the voltage magnitude after calibration is almost equal to 120 V.

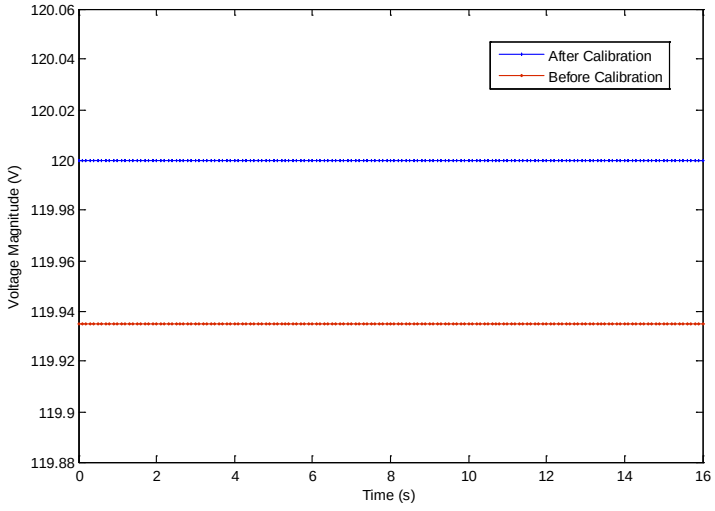

Figure 2-4 Voltage Magnitudes before and after Calibration

3) Voltage Angle Shift

Similar to voltage magnitude, voltage angle shift may be generated due to the different characteristics of electronic circuits. After calibrating the voltage magnitude and eliminating the "saw teeth" on the angle curve, the last step of calibration is to eliminate the angle shift. If a standard 60 Hz/0° voltage source is connected during the calibration process, the angle shift correction coefficient φ_{shift} can be calculated as follows:

$$\boldsymbol{\varphi_{shift} = 2\pi - \frac{1}{n}\sum_{i=1}^{n}\varphi_i \ (i = 1, 2, \dots, n)} \qquad 2\text{-}6$$

where n is the number of voltage angle measurement points. Then, the angle shift correction coefficient φ_{shift} is added to each angle measurement in the algorithm so that all the FDRs can be calibrated to the same angle reference. The voltage angles of one FDR before and after calibration are shown in Figure 2-5. The original voltage angle is around 2.8223 rads. The angle shift correction coefficient φ_{shift} is calculated by Equation 2-6 and is equal to 3.46084 rad. As seen from Figure 2-5, the voltage angle after calibration is almost equal to 0 rad.

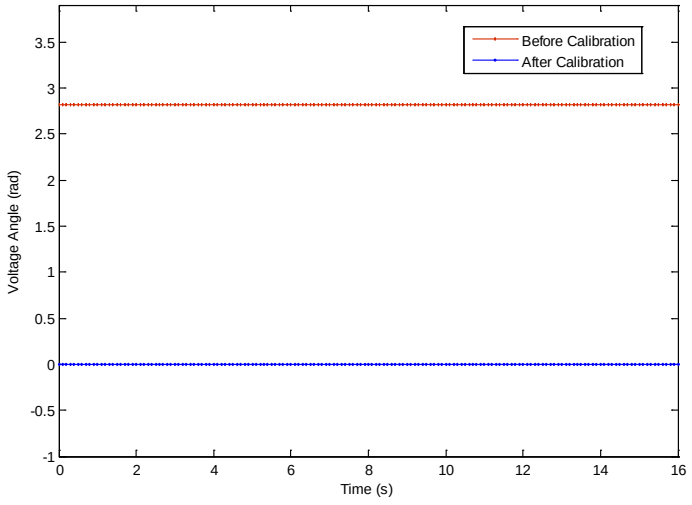

Figure 2-5 Voltage Angle before and after Calibration

2.3 Dynamic Test of Frequency Disturbance Recorder

IEEE C37.118-2005 standard states that different PMUs behave differently and "Behavior under transient conditions is not mandated"[4]-[5]. However, the dynamic accuracy of synchrophasors is very important for power system dynamics analysis. Therefore, this section will introduce the preliminary dynamic test method of FDRs.

1) Step Test

Step test is a basic method to test the dynamic performance of the FDRs during transient conditions. Both positive and negative step tests of voltage and frequency are considered in this section. Figure 2-6 shows the results associated with the step test of voltage magnitude. As shown in Figure 2-6, the voltage signal has an initial period of constant magnitude, which is followed by several periods of magnitude step changes. It can be seen that the testing FDR can respond simultaneously to the sudden positive and negative step change of voltage with the standard FDR that has been previously tested by other methods.

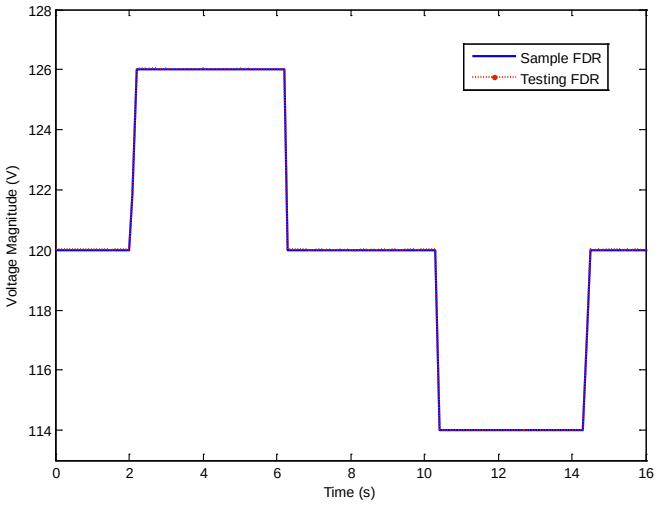

Figure 2-6 Step Test of Voltage Magnitude

Figure 2-7 shows the results associated with the step test of frequency. It can also be seen that the testing FDR can quickly respond to the sudden positive and negative step of frequency.

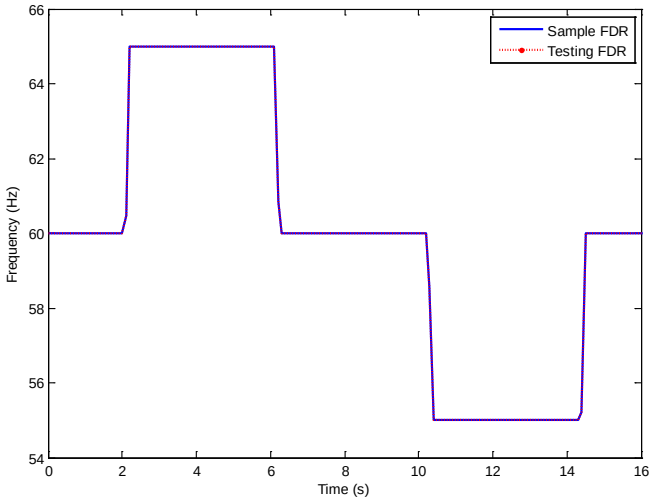

Figure 2-7 Step Test of Frequency

2) Ramp Test

Ramp test is another test method considered in this section. In this test, the start frequency f_{start} in Figure 2-8 is set to 60 Hz and the stop frequency f_{stop} is set to 55 Hz or 65 Hz. The ramp, hold and return times are all set to 5 seconds according to literature [6]. A case study of the frequency ramp test is shown in Figure 2-9, from which it can be seen that the testing FDR can pass the frequency ramp test easily.

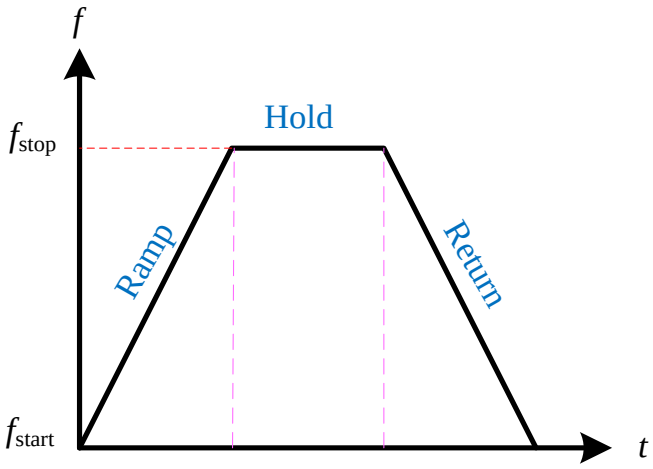

Figure 2-8 Frequency Ramp Test Method

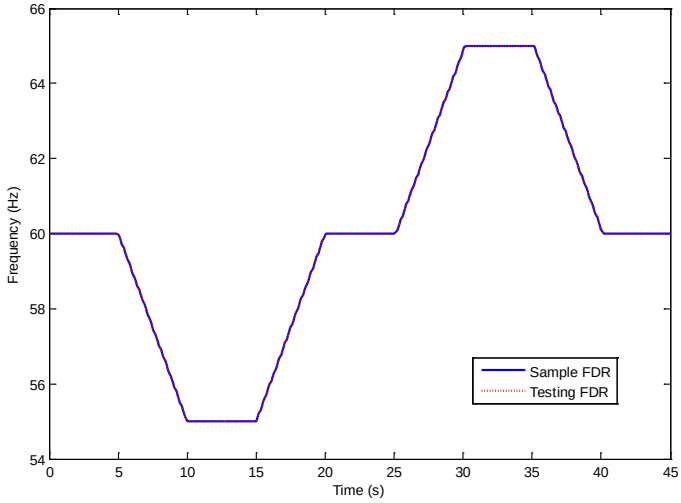

Figure 2-9 Ramp Test of Frequency

2.4 GPS Signal Loss Test of Frequency Disturbance Recorder

Global position system (GPS) is made up of a constellation of twenty-four active satellites orbiting approximately 20, 200 kilometers above the surface of the earth.

Originally deployed by the United States Department of Defense (DOD), all of these satellites have onboard atomic clocks that synchronize to within 3 ns of the official atomic clock located at the United States Naval Observatory (USNO). Furthermore, the basic accuracy of each GPS receiver is within 0.2 μs of Coordinated Universal Time (UTC). The GPS signals can be received across the globe, and a position solution can be solved by acquiring at least four satellites. And once an accurate position solution is given, the receiver will only need one satellite for clock synchronization. The unique fact that the signals from these satellites are synchronized with the atomic clock allows the end users of the system to receive synchronized time information. Besides the initial prerequisite of acquiring a fix with four satellites, there exist a number of factors that could affect its performance in providing accurate timing. Most importantly, the GPS antenna position plays a crucial role. For optimal performance, the antenna should have an unobstructed view of the horizon in all directions. This will enable the receiver to monitor the maximum number of satellites simultaneously, and to provide a more stable GPS lock. On the other hand, there are some factors that affect GPS performance which are uncontrollable. These factors can include atmospheric delays, signal multi-path interference, satellite geometry and satellites orbital errors. Overall, the drawbacks of GPS as a timing reference are overshadowed by the overall accuracy and that makes the GPS a top candidate for time synchronization in synchrophasor measurements [7].

For example, the current FDR design is based on Motorola® M12+ GPS receiver to provide timing synchronization. With these receivers, the timing accuracy is specified to reach below 10 nanoseconds [8]. However, as mentioned above, there are a series of complex factors that affects the availability of GPS signals. Based on the previous experiences of FNET system, the GPS receiver tends to lose signals at times even when the antenna is placed in a location with the unobstructed view of the satellites. Therefore, it’s necessary to study the synchrophasor measurement accuracy when the GPS receiver cannot obtain the stable satellite signals.

2.4.1 Test Preparation

The test is designed and completed on the FDRs. A block diagram of the test's layout is presented in Figure 2-10. Specifically, Doble Power System Simulator F6150 (GPS antenna included) is used as the standard voltage source that provides the standard 110 V/60 Hz/0° voltage signal and the measurement data from the FDR units are sent to the local data server via the Internet.

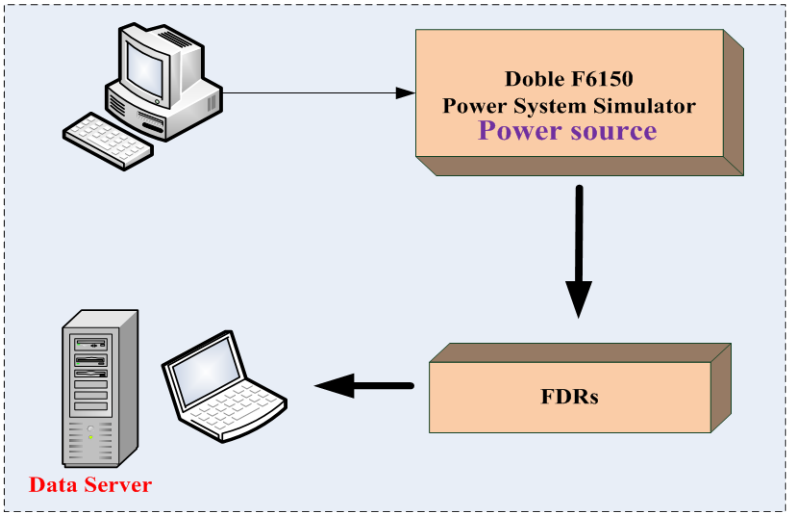

Figure 2-10 Block Diagram of the GPS Signal Loss Test

2.4.2 Test Procedures and Results

As mentioned previously, the FDRs measure the voltage phase angle, voltage magnitude, and system frequency at a very precise level with the help of GPS synchronization. However, among the three parameters measured by FDRs, the accuracy of voltage angle measurement is what we concern most, simply because the frequency is not directly measured but calculated through the rate of voltage angle change [9]. Furthermore, voltage angle is also the most sensitive parameter to GPS signal loss. Therefore, voltage

angle is chose as the test parameter to reflect the influence of GPS signal loss on the measurement accuracy.

This test involves 4 FDR units. The first FDR, unit 762, has a stable lock on the GPS satellites during the whole test procedure in order to ensure the measurement accuracy. Therefore, its measurement can be considered as the reference in this test. For FDR unit 756, its antenna will be kept unplugged for 15 minutes to emulate the GPS signal loss and then will be re-plugged to let the GPS receiver pick up the stable GPS signals. After that, the antenna of unit 756 will be unplugged again and kept for another 30 minutes. For FDR unit 763 and unit 787, their antennas will be kept unplugged for 60 minutes and 120 minutes, respectively. The voltage angle data recorded by FDR units 756,763, 787 are deducted from the reference value provided by unit 762 and the results are shown in Figure 2-11, Figure 2-12 and Figure 2-13, respectively. It should be noted that all the FDR units have been calibrated and working normally before the test.

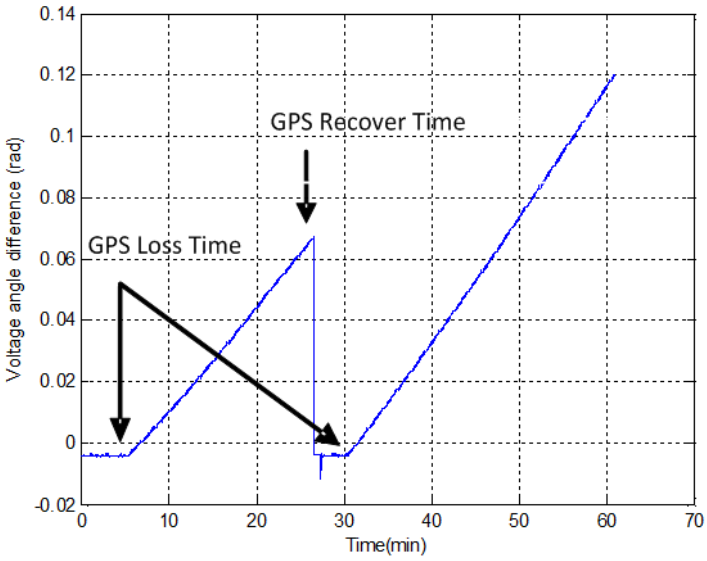

Figure 2-11 Voltage Angle Difference between Unit 756 and 762

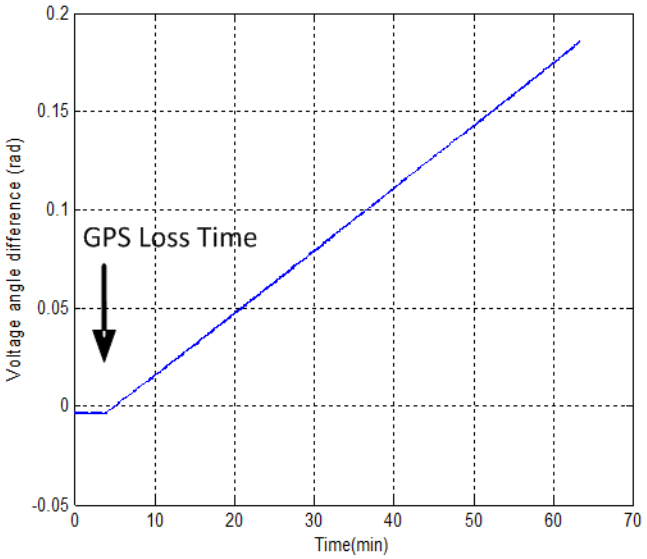

Figure 2-12 Voltage Angle Difference between Unit 763 and 762

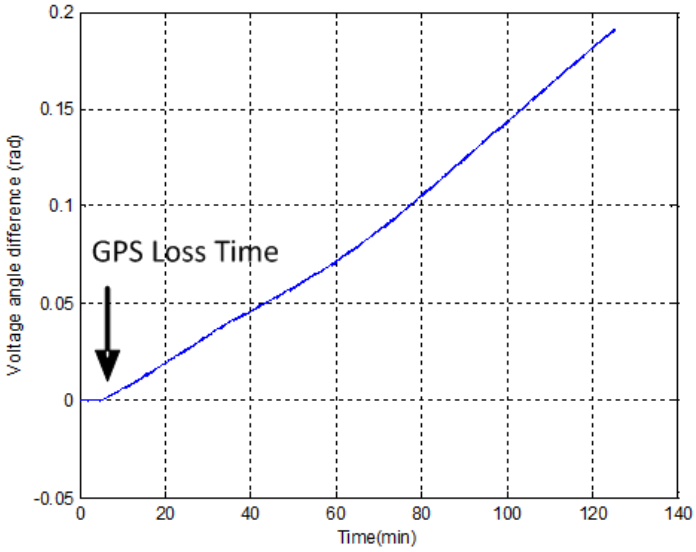

Figure 2-13 Voltage Angle Difference between Unit 787 and 762

From the results shown above, it's obvious that the voltage angle measurement errors of FDR units increase with the GPS loss duration time. This is due to the fact that the sampling process is no longer synchronized with the GPS signal and the error will

accumulate continuously over time. Furthermore, it's important to note that, despite the similar linear relations between measurement error and GPS loss duration time, the angle difference curve slope that represents the error accumulating rate is quite different for different FDR units. For example, the slope of FDR unit 756 is about 0.0043 rads/min while those of units 763 and 787 are about 0.0030 and 0.0016 rads/min. Considering the fact that FDR units have to depend on the internal clock of GPS receiver M12+ for synchronization after losing GPS signals, it can be concluded that the GPS receiver oscillator clock is not accurate enough for phasor measurements. Hence, once the GPS receiver loses the satellite signals, the voltage angle measurements should not be trusted. However, from Figure 2-11, it demonstrates that despite the large errors caused by the GPS signal loss, the FDR angle measurement can be corrected as soon as the GPS signal is picked up again. Thus, it proves that the angle measurement accuracy of the FDRs is highly dependent on the acquisition of GPS signals.

Despite the obvious error of angle measurement, it can be seen from Figure 2-14 and Figure 2-15 that the frequency and voltage magnitude difference between unit 787 and 762 are almost unnoticeable, which implies that the measurement errors of frequency and voltage are much smaller than that of the angle.

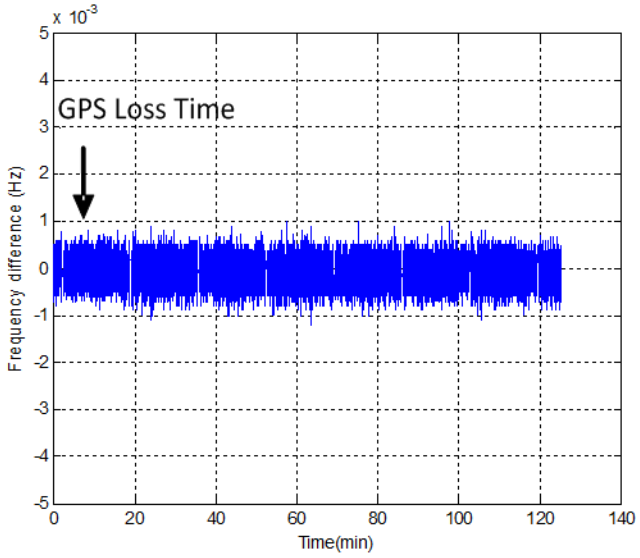

Figure 2-14 Frequency Difference between Unit 787 and 762

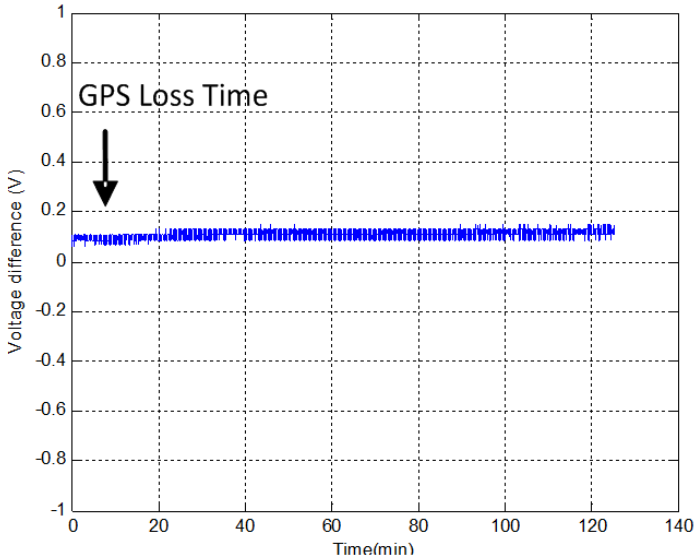

Figure 2-15 Voltage Magnitude Difference between Unit 787 and 762

2.4.3 Comparison between High-sensitivity and Conventional GPS Receivers

As demonstrated above, the GPS signal loss issue impairs the synchrophasor measurement accuracy significantly and thus, how to ensure the availability of GPS signals for synchrophasors will be discussed in this section.

The high-sensitivity GPS receiver, usually known as the indoor GPS, uses a large number of correlators and additional digital signal processing techniques to search for GPS signals [10]; thus, it can be used to provide position or time information under conditions where GPS signals are extremely weak. As a possible solution to the GPS signal loss problem, it is worthwhile to test the high-sensitivity GPS receiver for synchrophasor measurement. In this section, the performance of a high-sensitivity GPS receiver, Navsync® CW12, is tested in different environments (see Figure 2-16) using the commercial GPS evaluation software Winoncore® 12. The comparison results with the conventional GPS receiver (Motorola® M12+, the one used in the current FDRs) are shown in Figure 2-17 and Figure 2-18, respectively.

Near the unobstructed window

In the office drawer

Figure 2-16 GPS Receiver and Antenna Placement Locations

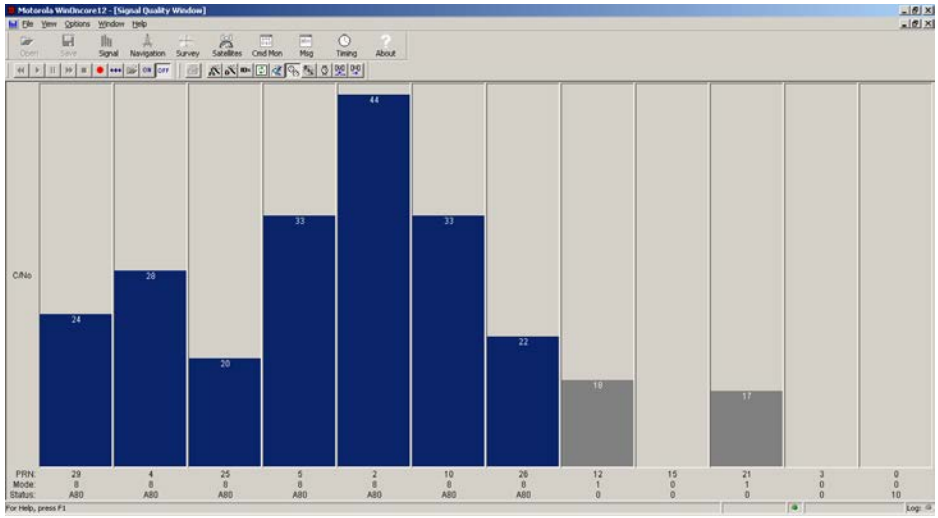

(a) Signal Quality of GPS Receiver CW12 near the Window

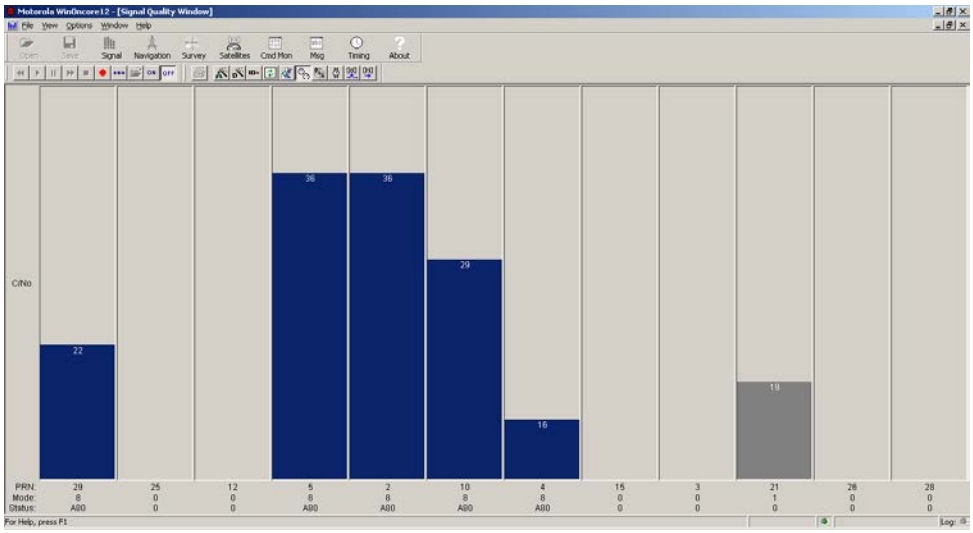

(b) Signal Quality of GPS Receiver M12+ near the Window

Figure 2-17 Signal Quality of GPS receivers near the Window

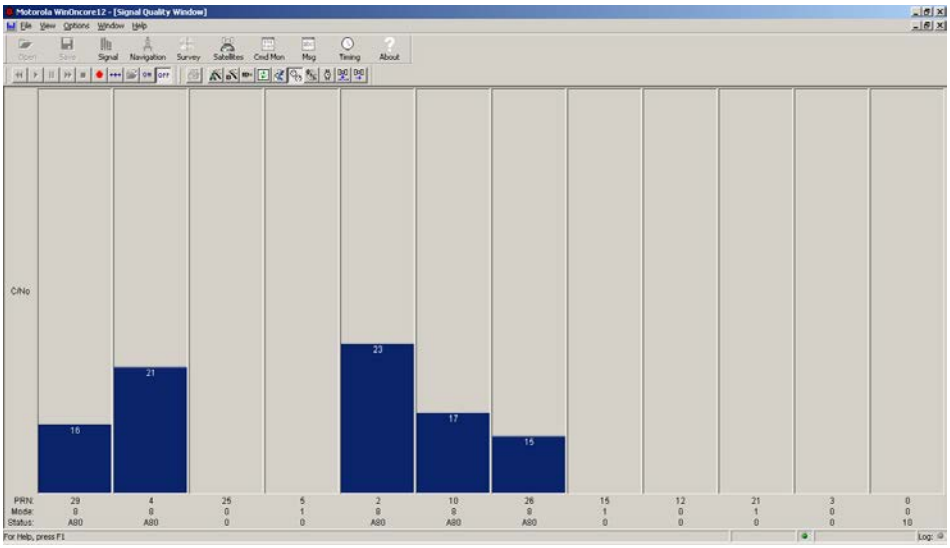

(a) Signal Quality of CW12 in the Office Drawer

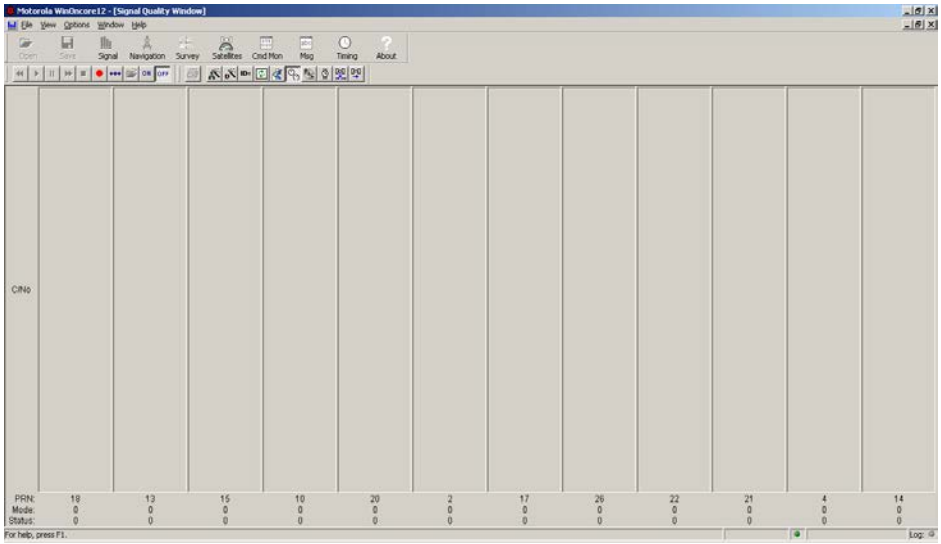

(b) Signal Quality of M12+ in the Office Drawer

Figure 2-18 Signal Quality of GPS Receivers in the Office Drawer

The blue bars represent the values of carrier to noise ratio (C/No), which is a measure of GPS signal quality of each satellite tracked by the GPS receiver. From Figure 2-17, it can be seen that both GPS receivers obtained the stable lock on more than four satellites near the window while the high-sensitivity GPS receiver CW12 is able to track more. However, when the antenna was placed in the office drawer, the M12+ could not track

any satellite while the CW12 could still obtain the stable lock on several satellites (see Figure 2-18). Apparently, the high-sensitivity GPS is capable of providing more reliable GPS signals. This test result may well justify the future application of high-sensitivity GPS receiver in synchrophasor measurements.

However, Figure 2-18(a) shows that the acquired GPS signals were attenuated dramatically due to the various factors such as multipath and reflections from obstructions and therefore there may be times when the indoor GPS receiver would have difficulty in acquiring any signals. In that case, the non-GPS based timing technologies needs to be considered, such as the enhanced Loran® system. It is an internationally-standardized positioning, navigation, and timing (PNT) service for use by many modes of transport and in other applications [11]. This technology utilizes AM radio signal instead of GPS signal to offer wide-area locating and timing service and the antennas are given in Figure 2-19. This technology has great potentials to become a reliable supplement of GPS.

E-field Antenna H-field Antenna

Figure 2-19 Receiving Antennas of eLoran System

2.5 Conclusions

Some FDR calibration and test results were presented in this chapter, including the FDR's calibration and dynamic test, the GPS signal loss test and the comparison test between conventional and high-sensitivity GPS receivers. Test results proved the FDR's relatively good dynamic performance and showed that the measurement accuracy of FDRs with conventional GPS would be dramatically impaired after losing GPS signal and the high-sensitivity GPS receiver can provide a more reliable GPS timing.

Considering the drawbacks associated with GPS time synchronization, the non-GPS based time synchronization methods, such as the eLoran® technology, can be considered as a backup in the future.

Chapter 3 WIDE-AREA CONTROL OF VARIABLE-SPEED WIND GENERATORS FOR FREQUENCY REGULATION AND OSCILLATION DAMPING IN THE EASTERN INTERCONNECTION (EI)

3.1 Introduction

Today, most of major power systems around the world are experiencing a steady increase of wind in their generation mix. This is causing concerns over the stability of the grid and other difficulties in system operation. Though some subjects such as voltage and reactive power control, power quality requirements, fault ride-through capability, have already been carefully examined and corresponding technical solutions may also be commercially available now[12]-[16], some other rising issues still remain to be addressed. For example, conventional synchronous generators play the pivotal role in primary frequency control and all other frequency regulations; however, due to the absence of synchronization torque for variable-speed wind generators, higher penetration of wind generation may continuously lead to the decrease of overall system inertia as well as the reduction of frequency regulation capabilities [17]-[21].

Another serious issue is the inter-area oscillation. Many studies have repeatedly shown that replacing conventional generation with DFIG-based wind farms has a significantly negative effect on the damping of inter-area oscillation modes of the interconnected system [22]-[25]. Moreover, for the Eastern Interconnection (EI), the majority of wind generation is now and in the near future will be located in the Northwest of the system, which is far from the load centers in the Northeast. Thus, new transmission lines may be necessary to transmit wind energy from western generation centers to eastern load centers, which may introduce new, difficultly damped inter-area oscillation modes as well as influence the existing ones.

However, thanks to the development of modern power electronics technology, the answer to the mentioned problems that wind generation causes may lie in wind generation itself.

Though the steady-state active power delivered to the grid solely depends on the mechanical energy transferred from the wind turbines, the electrical power of variable-speed wind generators can be effectively controlled by modern power electronics devices in a fast manner. As a result, wind generators have significant control capabilities to engage in bulk power system frequency regulation and oscillation damping, especially when the wind penetration is considerably high.

In this chapter, fast active power control techniques of variable-speed wind generators will be discussed and how to apply those controls to the EI system frequency regulation and oscillation damping will be introduced. This Chapter is structured as follows: In Section 3.2, fast active power control techniques of variable-speed wind generators will be summarized and discussed; in Section 3.3, the wind generator and power system model used in this chapter's simulation will be introduced; and in Section 3.4 and 3.5, the potential contributions of variable-speed wind generators to the EI system frequency regulation and oscillation damping will be studied respectively.

3.2 Fast Active Power Control Techniques of Variable-speed Wind Generators

Variable-speed wind generators mainly refer to permanent-magnet synchronous generators (PMSGs) and doubly-fed induction generators (DFIGs). A PMSG contains a multi-pole magnetic rotor and a back-to-back AC/DC/AC converter attached to the stator. The energy is transmitted through the converter from the stator to the grid and consequently, the generator is fully decoupled from the grid. DFIGs are more common, whose rotors that supply the AC excitation current are connected to the power system through the converters and stators are connected directly to the power system. During normal conditions, power electronics converters enable the variable-speed wind generators to capture wind energy over a wide range of wind speeds to their maximum extent (the maximum power point tracking, MPPT), improve power quality and regulate both active and reactive power.

During transient conditions, additional controllers could be installed on the converters or pitch controllers to achieve the fast active power controls [26]-[33]. In some studies, variable-speed wind generators can transiently support system frequency by implementing the kinetic energy-based active power control techniques, such as "hidden" inertia emulation or inertia droop control, to enable wind generators to have the “artificial” inertial response that behaves in a manner similar to conventional generators [33]. This type of control utilizes the kinetic energy stored in wind turbines to inject more active power into the power grid in seconds. The active power output of wind farms are only increased temporally, thus the normal operation point of wind generators remains unchanged. In fact, General Electric ® already has a commercial inertia droop control product known as WindINTERIA® [34]. Besides the inertial response, the function of power system stabilizer (PSS) in conventional generators could also be emulated utilizing the kinetic energy-based active power control techniques [35]-[42]. In this case, variable-speed wind generators can also contribute to the power system small-signal stability effectively. It should be noted that the sustained loss of kinetic energy would cause the rotational speed of a wind turbine to decrease and the turbine to stall if the rotational speed falls too low. Consequently, appropriate limits need to be imposed to avoid removing too much the kinetic energy.

As discussed above, wind generators usually works in the MPPT mode in order to utilize the wind power to the maximum extent, since wind energy is both environment-friendly and low-cost. However, if wind turbines operate in the “de-load” mode instead of the MPPT and saves some of the available power as reserve by pitch control or increasing the rotational speed from the MPPT value (usually referred to as “over-speed”, shown in Figure 3-1, where P is the mechanical power delivered by wind turbine and ω_r is the wind turbine rotational speed), certain control techniques can be implemented to enable wind generators to emulate the frequency droop characteristics (“governor response”) of conventional generators. In fact, the time constant of pitch control is relatively large to be implemented in practice and frequent adjustment of pitch blades would radically reduce their lifetime. Therefore, pitch control is neither practical nor economical for fast active power control purpose. Conversely, rotational speed control is provided by the power

electronics converter, thus it acts in a considerably fast manner, which makes possible the utilization of power reserve saved by “over-speed” to balance the instantaneous power consumption and provide support for the long-term frequency regulation [26]. Furthermore, though no research has covered this topic yet, wind generators may also act to automatic generation control (AGC) regulation order from the operator as effectively as conventional generators with the help of fast active power control if reserves exist.

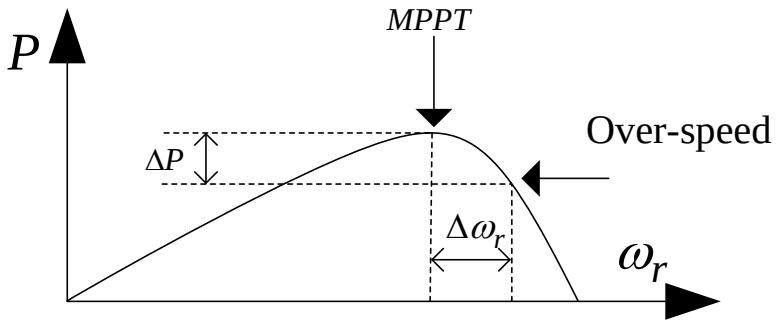

Figure 3-1 Over-speed Working Condition of the Wind Turbine

In sum, by implementing fast active power control techniques, variable-speed wind generators can emulate the inertial and governor responses of conventional generators to provide frequency regulation service and PSS function to contribute to the power system small-signal stability.

3.3 Variable-speed Wind Generator and Power System Model

3.3.1 Wind Generator Model

This chapter evaluates the potential contributions of variable-speed wind generators to frequency regulation and oscillation damping in the EI system. PSS/E has the capability of handling both large-scale power system dynamic simulation and wind generation

system modeling, thus is employed in this chapter's simulation. The variable-speed wind generator model used in this chapter's simulation and the buildup of the EI simulation scenarios are introduced in this section. Since DFIG is the most common wind generator type nowadays, variable-speed wind generators are simulated as DFIGs in this chapter. WT3 wind turbine stability model was developed in PSS/E to simulate the performance of a wind turbine employing a doubly-fed induction generator (DFIG) with the active control by a power converter connected to the rotor terminals [43]. There are four basic components for WT3 model (shown in Figure 3-2), namely:

- WT3G: generator/converter model
- WT3E: electrical control model
- WT3T: mechanical control (wind turbine) model
- WT3P: pitch control model.

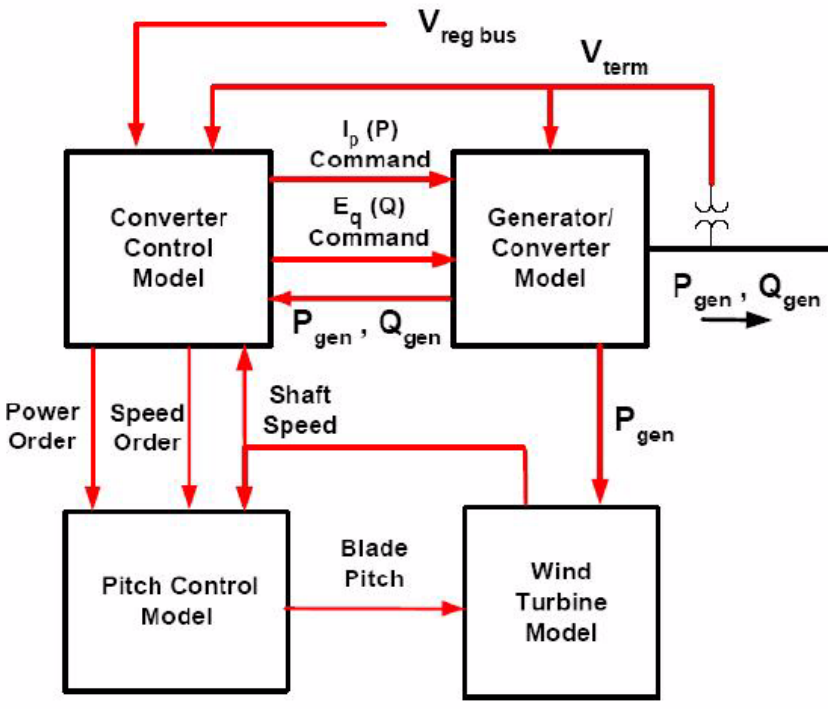

Figure 3-2 Structure of WT3 Wind Turbine Stability Model in PSS/E

Typical parameters of a GE® 1.5 MW wind generator from PSS/E are employed in the simulations of this study. And in order to realize the mentioned fast active power control techniques, a user-defined electrical control model has to be developed in PSS/E based on the original WT3E model (Parameters and control structure given in Appendix B). Please note that since pitch control and reactive power control are not considered in this study, WT3P part is ignored and constant reactive power control mode is selected in all the simulations.

3.3.2 Power System Model

The Eastern Interconnection (EI) is one of the two major alternating current power grids in North America. It reaches from central Canada eastward to the Atlantic coast (excluding Quebec), south to Florida, and back west to the foot of Rocky Mountain (excluding most of Texas). Its 16, 000-bus dynamic model is selected as the base case in this study's simulation. The total generation capacity of this model is around 590 GW, which includes more than 3,000 generators (This model is protected by non-disclosure agreement with Tennessee Valley Authority (TVA), thus no detailed information is allowed to be released). However, no wind generation is modeled in the original model; therefore a simulation scenario with wind penetration needs to be developed in this section.

3.3.3 Simulation Scenario Construction

To simulate a relatively realistic penetration of wind generation in the EI system, 5% of the EI generation capacity is converted to wind generators in this study. Their locations are roughly shown in Figure 3-3. Though most of current wind generators are located in the Northwest of the EI, a significant number of off-shore wind farms are expected to be installed in the near future, as shown in Figure 3-3. And one thing should be noted that is that wind generators are and will be mostly located on the edges of the EI system, which gives them greater potential to help damp the inter-area oscillations. Since wind generator is used to replace the same amount of conventional generators in the EI model, the original power flow remains unchanged.

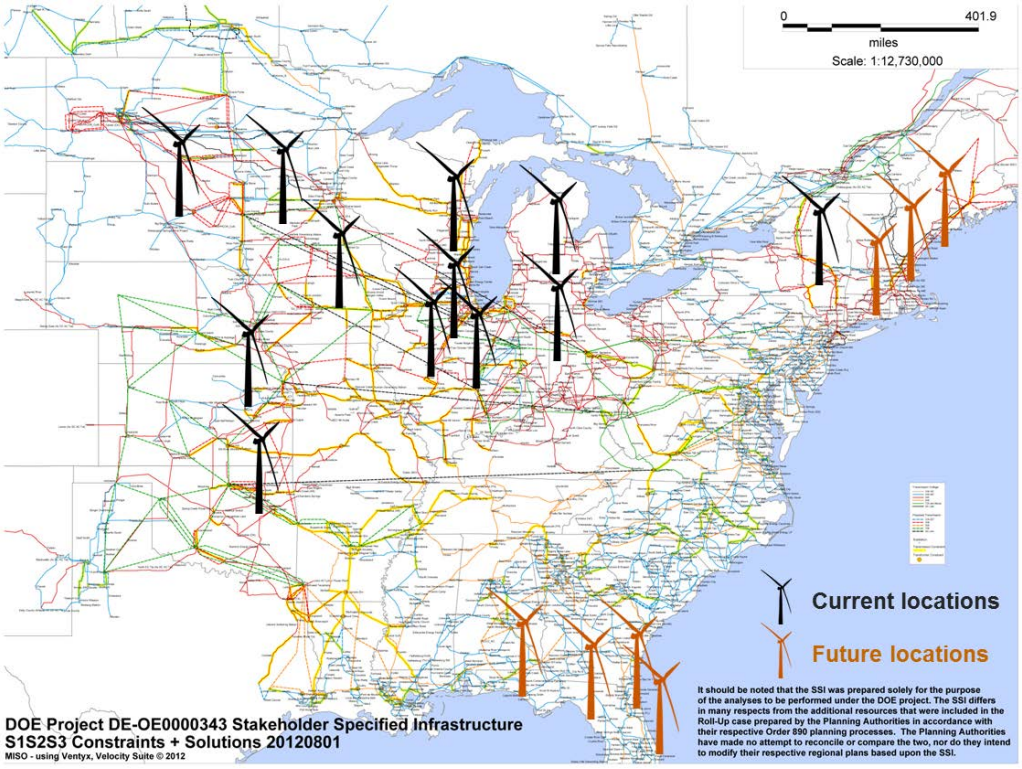

Figure 3-3 Major Wind Farm Locations in the Created EI System Simulation Scenario

3.4 Contribution of Wind Generators to the EI Frequency Regulation

In order to enable variable-speed wind generators engage in frequency regulation, several active power control techniques are employed in the user-defined PSS/E WT3 electrical control model, including wind inertia control, wind governor control and wind AGC control, which are introduced respectively in this section.

3.4.1 Wind Inertia Control

The wind inertia control here is of the same philosophy as GE WindINERTIA® technology, whose objective is to let variable-speed wind generators provide similar inertial response to the conventional generators'. Droop control is utilized to produce an active power output change that is proportional to the frequency deviation, which is given

by

$$\Delta \boldsymbol{f} = \boldsymbol{f}_{\boldsymbol{meas}} - \boldsymbol{f}_{\boldsymbol{ref}} \quad 3\text{-}1$$

where f_{meas} is the measured system frequency and f_{ref} is the reference frequency. The structure of wind inertia droop control is shown in Figure 3-4, in which frequency deviation goes through the low-pass and washout components. And the descriptions of parameters are given in Table B-2 in Appendix B.

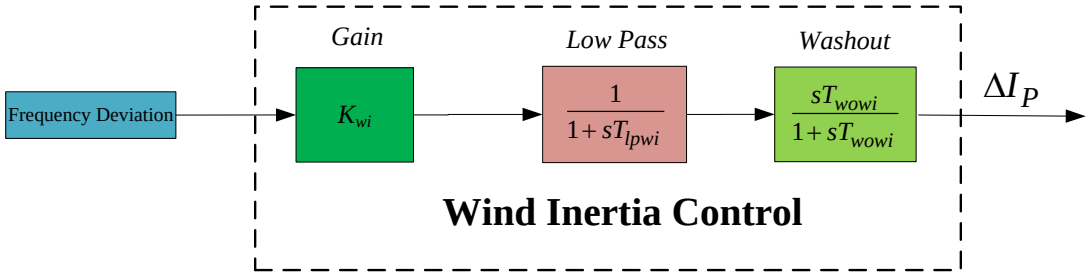

Figure 3-4 Wind Inertia Control Structure

3.4.2 Wind Governor Control

As discussed in Section 3.2, if working in “over-speed” zone, wind turbines can decrease the rotational speed to release the power reserve in seconds. Therefore, governor response can be achieved for wind generators utilizing the wind power reserve. Again, droop control is used and the wind governor control is shown in Figure 3-5. And the parameters are given in Table B-3 in Appendix B.

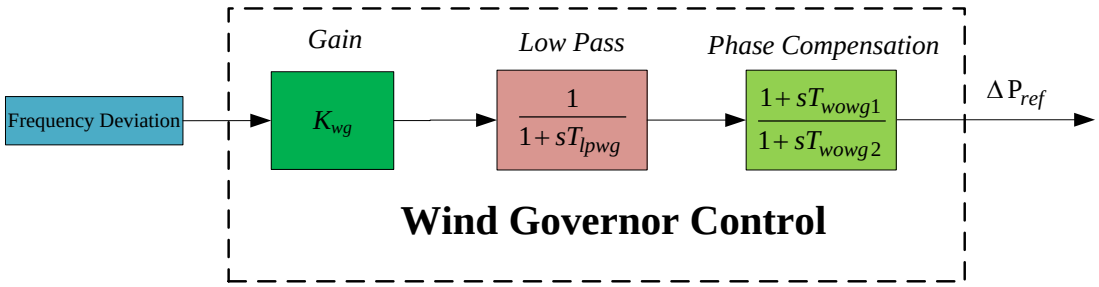

Figure 3-5 Wind Governor Control Structure

3.4.3 Wind AGC Control

Automatic generation control maintains the long-term balance of system generation and consumption in the bulk power system. Though no paper has covered this topic yet, wind generator can act to the AGC regulation order from the operator as effectively as conventional generators as long as the reserve is available. Actually, thanks to the fast response speed of power electronics converters, the power output of wind generators ramps up/down quickly, which makes wind generation system great candidates for the AGC regulation. The only disadvantage is the waste of wind energy due to the reserve during normal conditions.

3.4.4 Case Study-Generation Trip

To evaluate the potential contribution of wind generators to the EI system frequency regulation, a case of 1000 MW generation trip is simulated in the 16,000-bus EI system under various control scenarios in this section. The frequency responses following this event are shown in Figure 3-6 and the active power outputs of a typical wind farm are shown in Figure 3-7.

From Figure 3-6 and Figure 3-7, if only with wind inertia control (green line), the wind generator increases its active power temporally in the several seconds following the generation trip by use of the kinetic energy stored in the wind blades. However, as discussed above, the active power increase cannot be sustained and after the temporal

active power surge, the wind generator active power output will go through a “dip”, during which the inertial energy of turbine blades is “recharged”. As a result, the turbine speed can be observed to go through the phase of “deceleration” to release certain amount of kinetic energy and the phase of “acceleration” to “recharge”, which is shown in Figure 3-8. Apparently, though the wind inertia control function does not contribute to the long-term frequency recovery, it does help reduce the frequency drop nadir, which is shown clearly in Figure 3-6.

If only deployed in wind governor control mode, wind generators behave just like the conventional generators but in a much faster manner (red line in Figure 3-7): the wind generator active power output will ramp up to a higher level because of the existence of the “governor” function and the wind reserve will be put into utilization by moving the operation point away from “over-speed” zone to some extent. In this way, the governor control helps reduce not only the nadir but also the longer-term frequency deviation.

If the inertia and governor control are applied simultaneously, the frequency nadir will be reduced further and the steady-state frequency deviation will also decrease as a result (light green line in Figure 3-7). However, in order to eliminate the steady-state frequency deviation, AGC control should be considered. In the last scenario of Figure 3-6 and Figure 3-7, all the wind generators receive the AGC order at 10-th second to increase their active power outputs. In this case, the steady-state frequency deviation is reduced further, almost back to the nominal value.

Furthermore, as shown in Figure 3-9, reactive power outputs of variable-speed wind generators in all cases are similar because the constant reactive power control mode is selected for all of them.

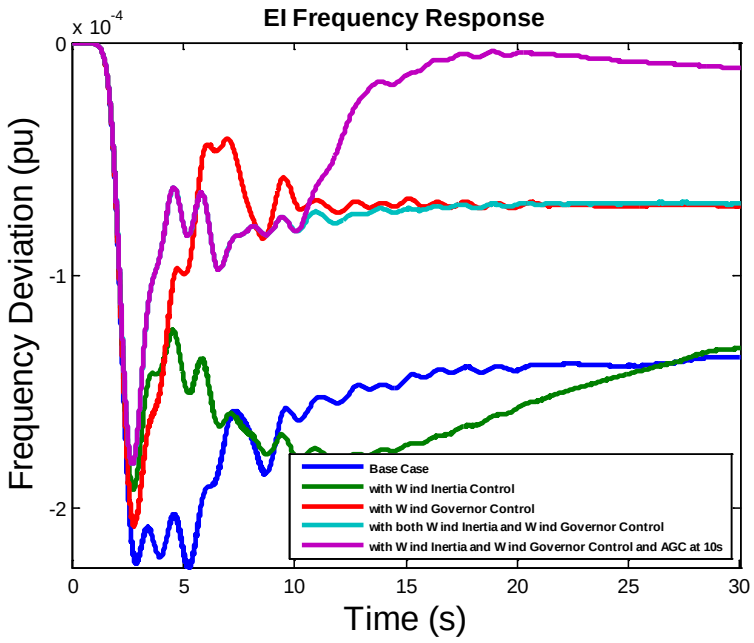

Figure 3-6 Frequency Responses of the EI after a Generation Trip with Different Wind Generator Controls

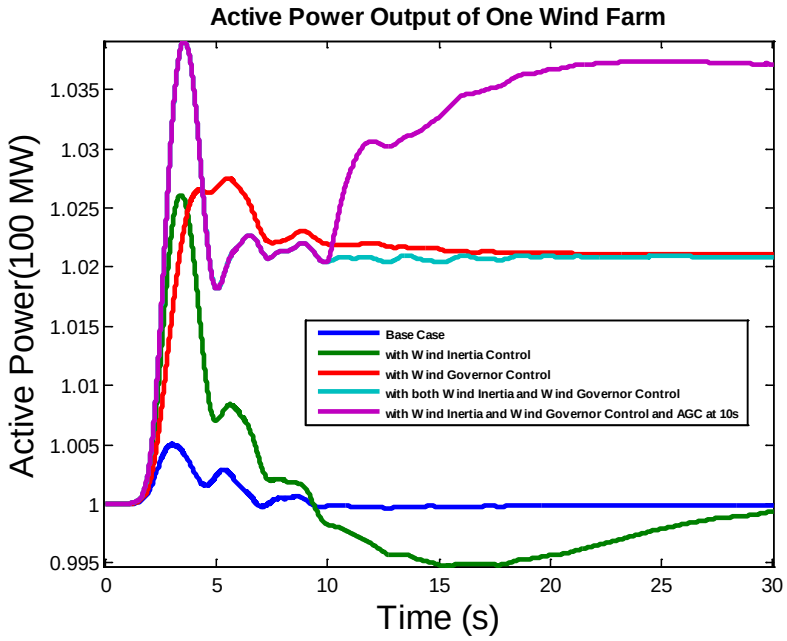

Figure 3-7 Active Power Outputs of a Typical Wind Farm after a Generation Trip with Different Wind Generator Controls

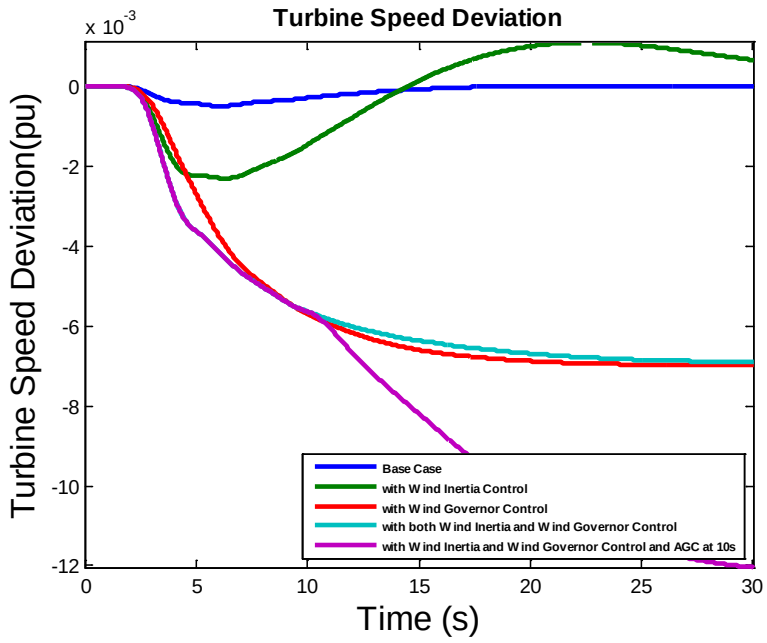

Figure 3-8 Turbine Speed Deviations of a Typical Wind Farm after a Generation Trip with Different Wind Generator Controls

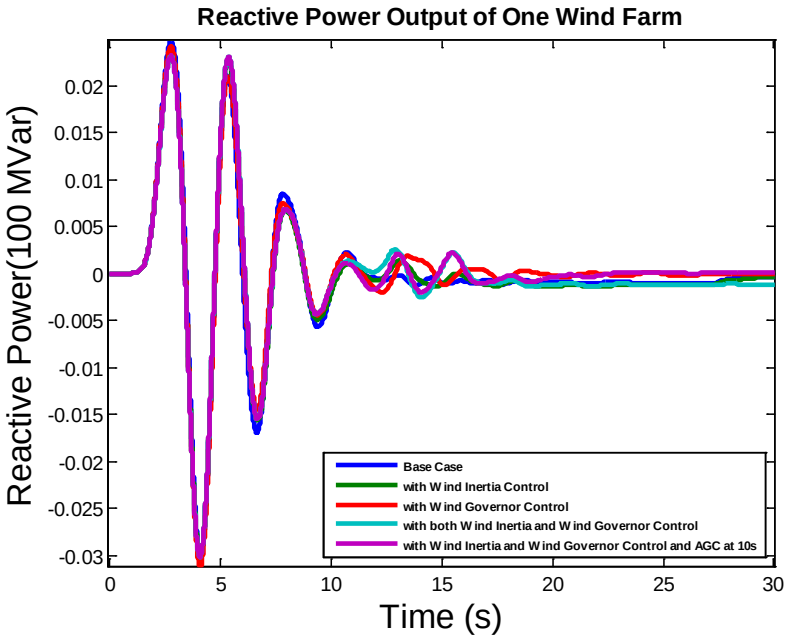

Figure 3-9 Reactive Power Outputs of a Typical Wind Farm after a Generation Trip with Different Wind Generator Controls

3.4.5 Case Study-Load Shedding

Not surprisingly, wind generators can also contribute to the frequency response improvement in load shedding cases. In this case, instead of decreasing wind turbine speed and release the reserve, wind turbines accelerate to store more energy in the blades and save more reserve so that the frequency excursion will be reduced. To demonstrate this effect, a load shedding event of 724 MW is simulated. Similar to the generation trip case, the EI system frequency response, active/reactive power and turbine speed of a typical wind farm are given below from Figure 3-10 to Figure 3-13.

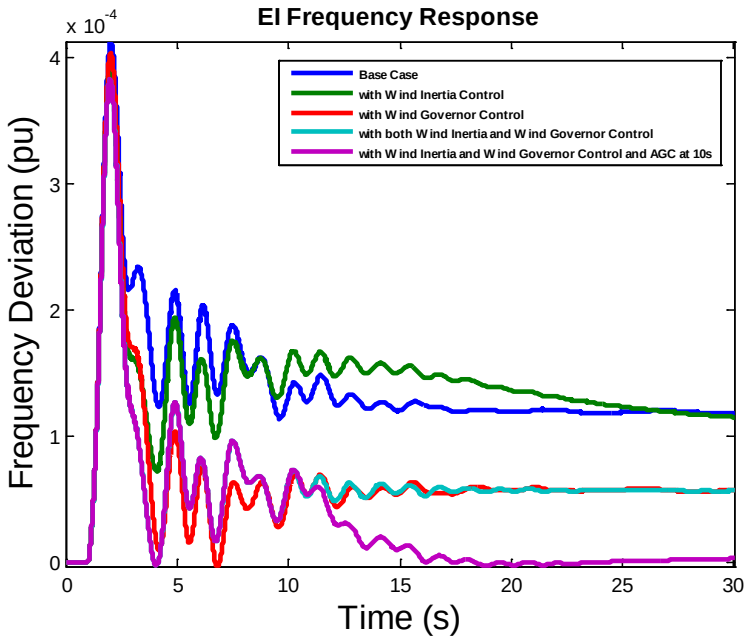

Figure 3-10 Frequency Responses of the EI after a Load Shedding with Different Wind Generator Controls

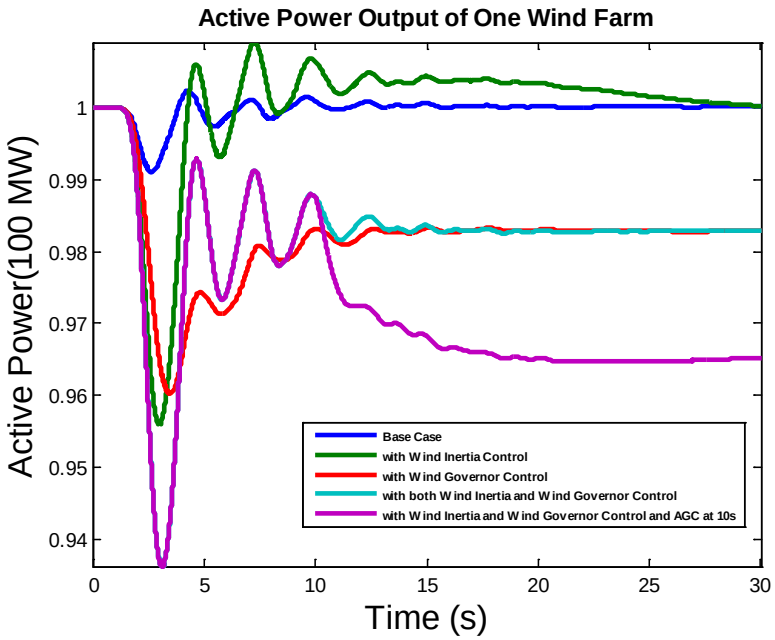

Figure 3-11 Active Power Outputs of a Typical Wind Farm after a Load Shedding with Different Wind Generator Controls

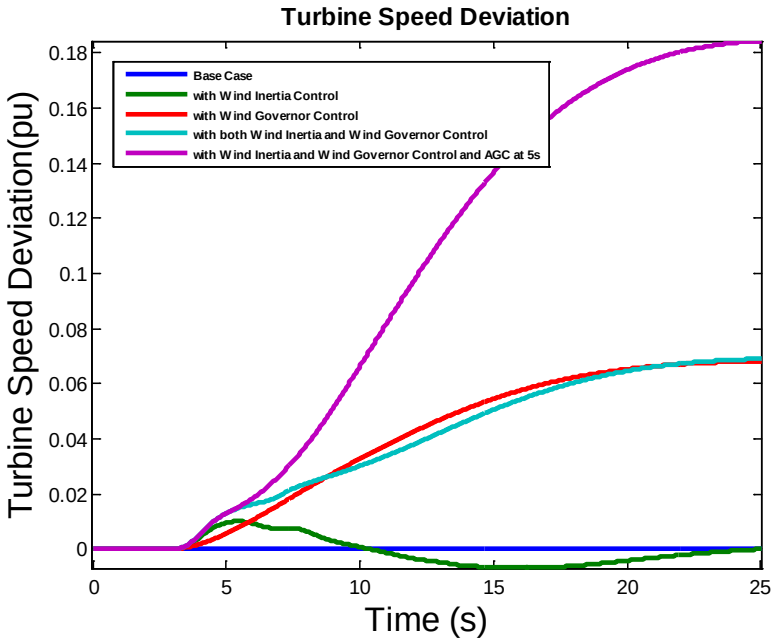

Figure 3-12 Turbine Speed Deviations of a Typical Wind Farm after a Load Shedding with Different Wind Generator Controls

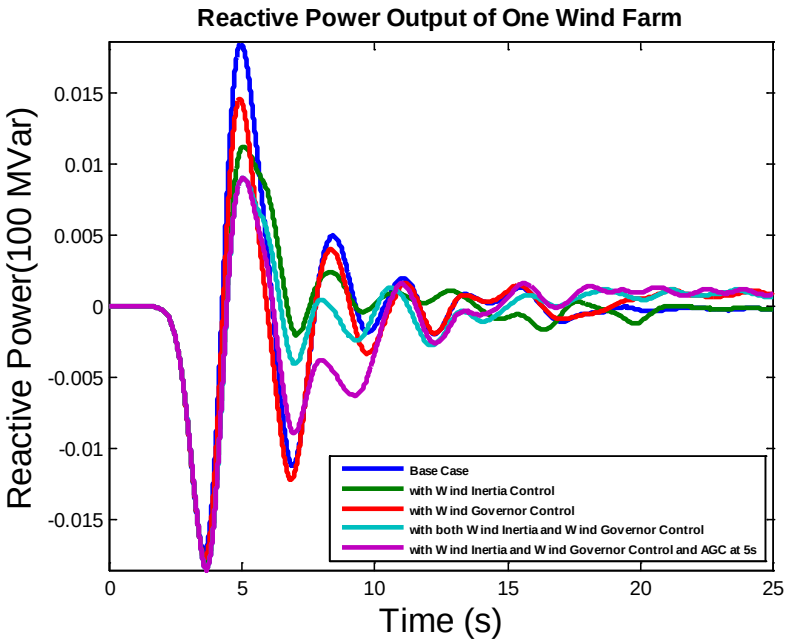

Figure 3-13 Reactive Power Outputs of a Typical Wind Farm after a Load Shedding with Different Wind Generator Controls

3.4.6 Frequency Regulation Movie Display

To demonstrate the overall effect of wind generator control on the EI frequency regulation, a movie is made in this subsection based on the EI simulation data, a snapshot of which is given below in Figure 3-14. Each red dot in the map on the right side of the movie snapshot stands for one monitoring point in the EI system and contour drawing method is used here to obtain the whole picture of the EI. From Figure 3-14, it's clear that the EI system frequency response can be improved dramatically in terms of both frequency drop nadir and steady-state frequency deviation.

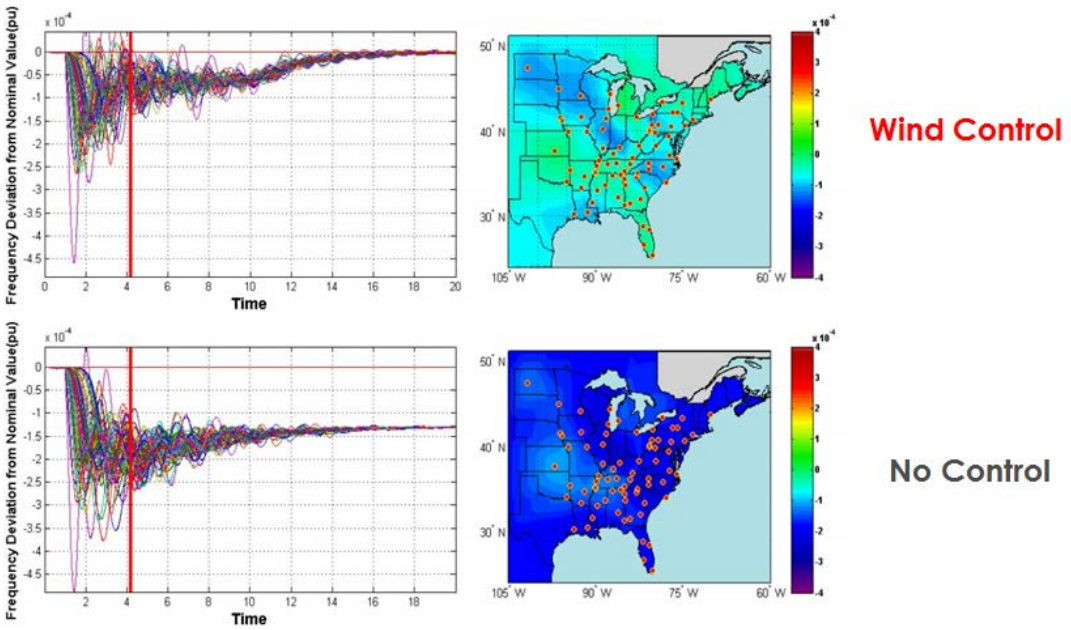

Figure 3-14 Movie Display of the EI System Wind Generator Control for Frequency Regulation

3.4.7 Discussion

Nowadays, though the wind penetration is still very low (3.4% of all generated electric energy in the U.S. in 2012 and 5% of total capacity in this scenario), variable-speed wind generators already acquire the ability to contribute to the frequency regulation effectively. If the wind penetration finally reaches 20% of the U.S. electricity by 2030 as expected by the U.S. Department of Energy's 2008 report, wind generation will become the game-changer of frequency regulation service market and therefore the corresponding regulation policies should be carefully studied.

3.5 Contribution of Wind Generators to the EI Oscillation Damping

Inter-area oscillation is another serious issue that increasing wind generation brings about. The wind generation's potential in oscillation damping has already been noticed by many researchers [35]-[42]. In this section, the potential of variable-speed wind generators' contribution to oscillation damping in the EI will be investigated.

3.5.1 *Wind PSS Control*

For conventional generators, power system stabilizer (PSS) adds damping to the generator rotor oscillations by producing a component of electrical torque in phase with the rotor speed deviations. A control structure similar to conventional generator PSS can be employed by variable-speed wind generators for oscillation damping, which is referred to as Wind PSS (the control structure is given in Figure 3-15) in this study. The signal washout block serves as a high-pass filter, with time constant T_{wowp} high enough to allow signals associated with oscillations to pass unchanged. Either a local or wide-area control signal can be used as the input to this wind PSS controller.

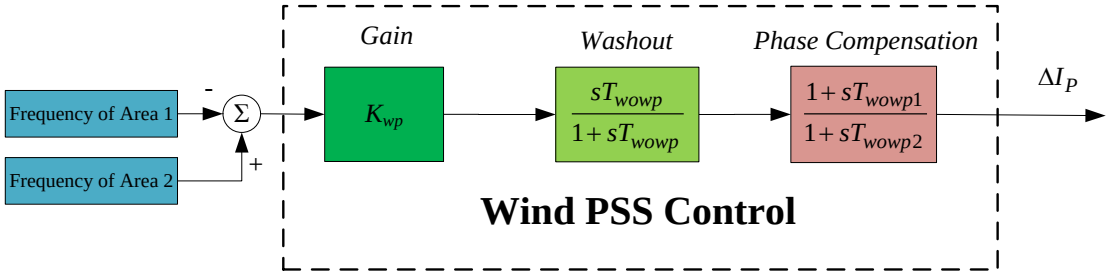

Figure 3-15 Wind PSS Control Structure

3.5.2 *Oscillation Damping Using Local Signals*

Fed by local frequency signal, wind PSS control can efficiently damp the local frequency fluctuation or oscillation. Figure 3-16 presents a case study of the EI system wind generator control in damping local frequency oscillation that is triggered by a local line trip. It's obvious that the local frequency oscillation can be dramatically damped. The corresponding wind generator active power fluctuation is shown in Figure 3-17, from which it's clear that the wind generator provides an effective damping electrical torque in order to damp the local frequency oscillation.

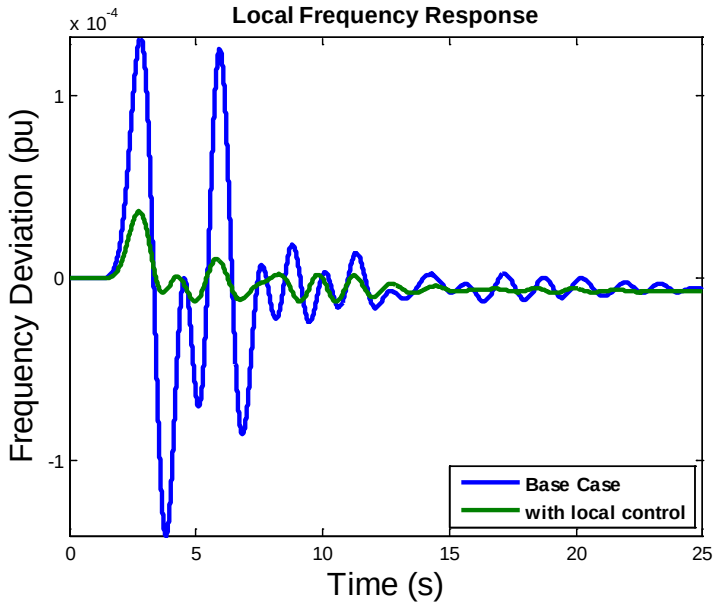

Figure 3-16 Local Frequency Oscillation Damping with Wind PSS Control Fed by Local Signals

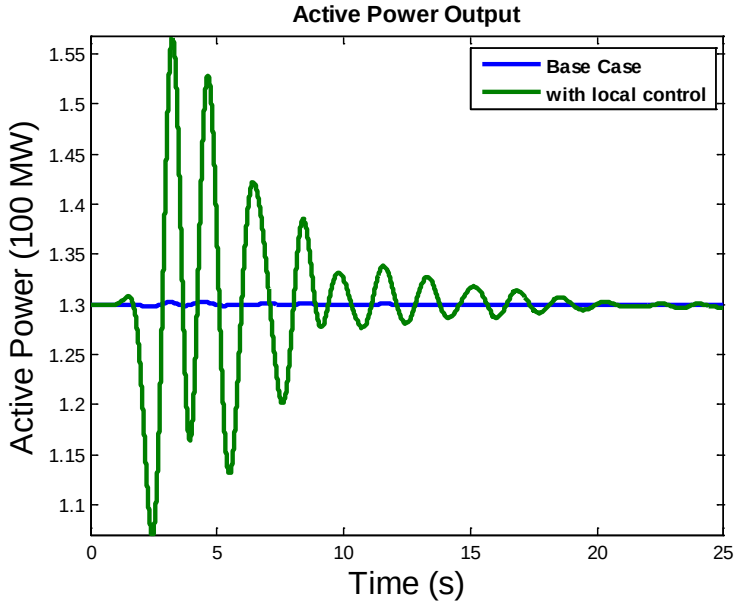

Figure 3-17 Active Power Output of a Wind Farm with Wind PSS Control Fed by Local Signals

Just like conventional PSS, wind PSS can also play a significant role in the inter-area oscillation damping. In the following case study, a generation trip of 814 MW in Florida is simulated in the 16,000-bus EI system to trigger the inter-area oscillation between the Northwest and South (NW-South) regions of the EI, as monitored by FNET system in the actual system [44]. Even fed by local frequency signal, the inter-area oscillation damping effect of wind PSS is significant, as shown in Figure 3-18.

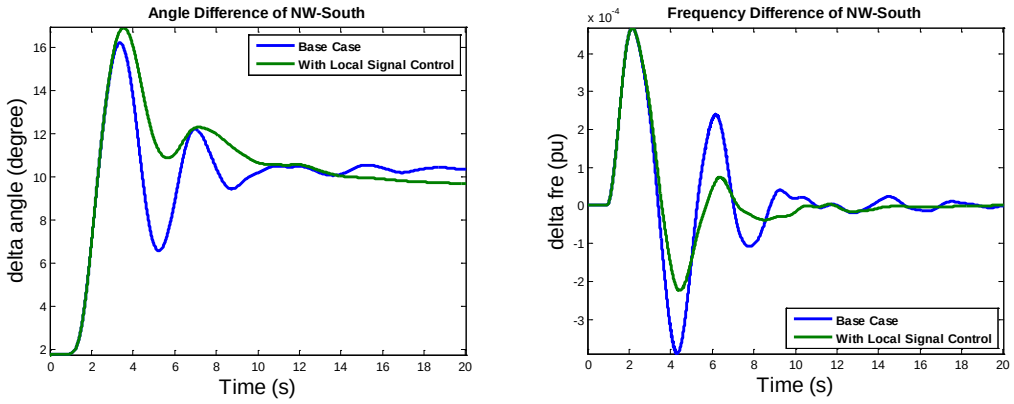

Figure 3-18 NW-South Inter-area Oscillation Damping with Wind PSS Control Fed by Local Signals

3.5.3 Inter-area Oscillation Damping Using Wide-area Signals

Nevertheless, previous studies have demonstrated that introducing wide-area signal to PSSs improves the inter-area oscillation damping effect to a great extent [45]-[46]. In this case study, if introducing the frequency difference of NW-South as the input signal to wind PSS, the NW-South inter-area oscillation can be damped much more effectively than just using local frequency signal, which is shown in Figure 3-19. It should be pointed out that the Northwest-Northeast (NW-NE) inter-area oscillation is negatively influenced in this particular case (Figure 3-20), which implies the necessity of the coordinated wide-area control.

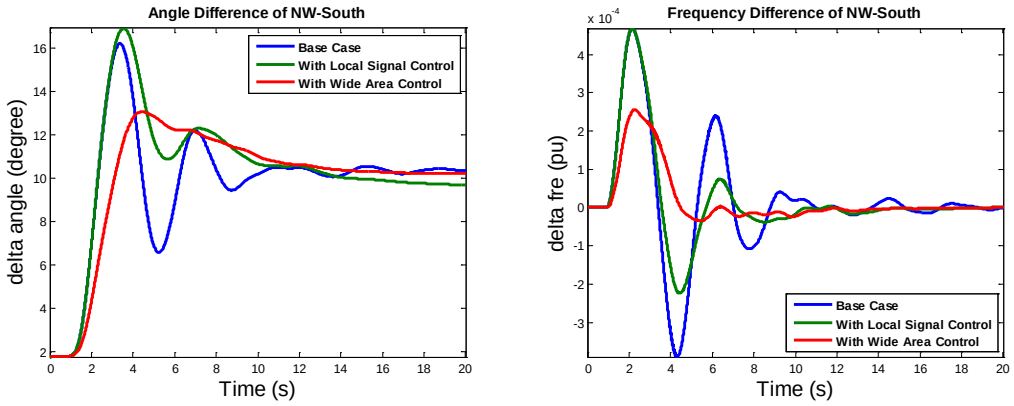

Figure 3-19 NW-South Inter-area Oscillation Damping with Wind PSS Control Fed by Wide-area Signals

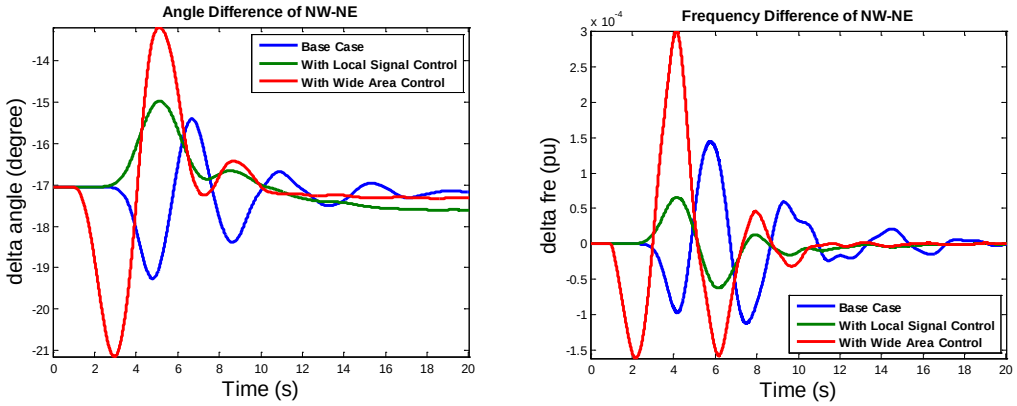

Figure 3-20 NW-NE Inter-area Oscillation Influenced by Wind PSS Control

3.5.4 Coordinated Inter-area Oscillation Damping Using Wide-area Signals

To further improve the overall oscillation damping effect, a simple coordinated strategy is developed in this section. As long monitored by FNET system [44], the main inter-area oscillations in the EI involves three main areas: NW (Northwest), NE (Northeast) and South. The coordinated wide-area wind PSS controller of each wind generator proposed in this section automatically compares the frequency differences between itself and the

other two areas, such as NW-South and NW-NE, and always chooses the larger one to damp. In this way, a coordinated oscillation damping effect can be achieved.

The same 814 MW generation trip is simulated in the Florida region of the EI to incite the NW-South and NE-South inter-area oscillations. The inter-oscillation damping results using both local signal control and coordinated wide-area control are shown in Figure 3-21. As demonstrated by the results, using local signal already damps the oscillations significantly but if with the proposed coordinated wide-area control, the inter-area oscillations between any two large regions can be damped almost completely.

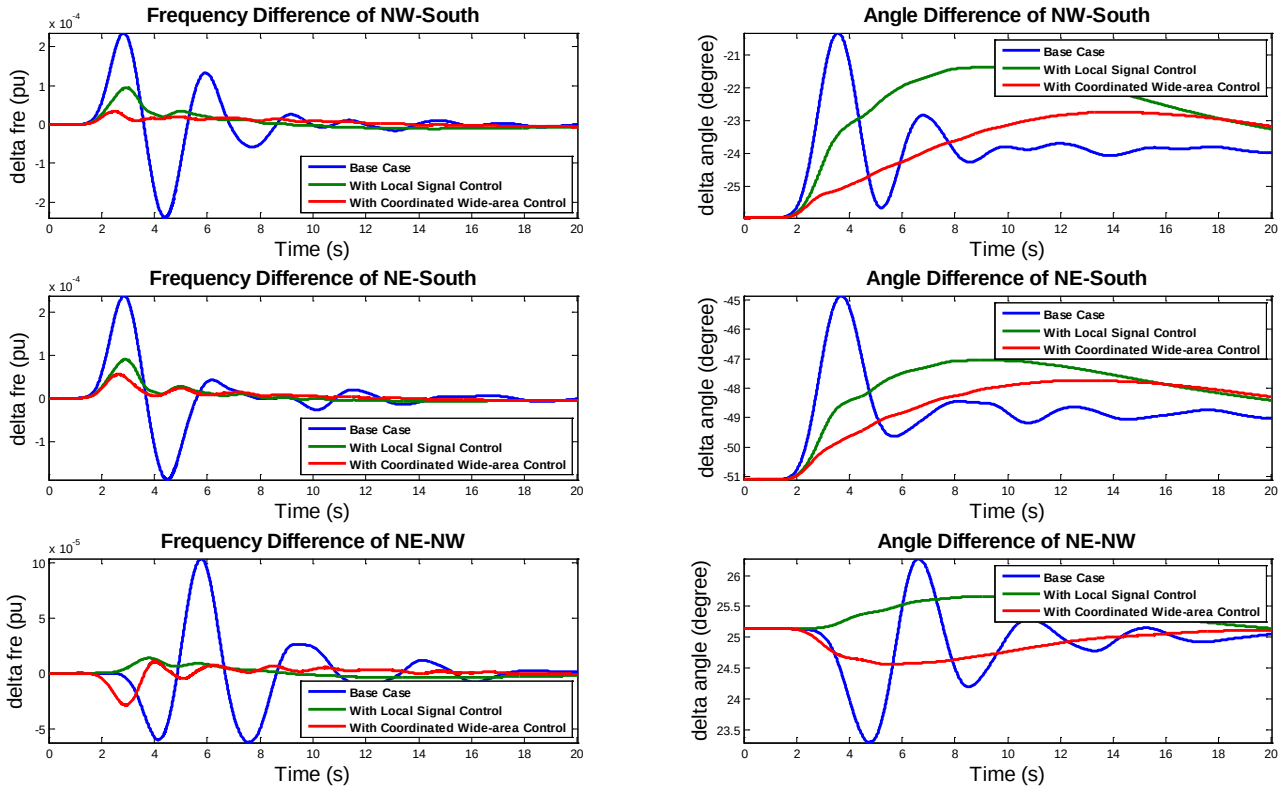

Figure 3-21 Inter-area Oscillation Damping using Coordinated Wide-area Wind PSS Control

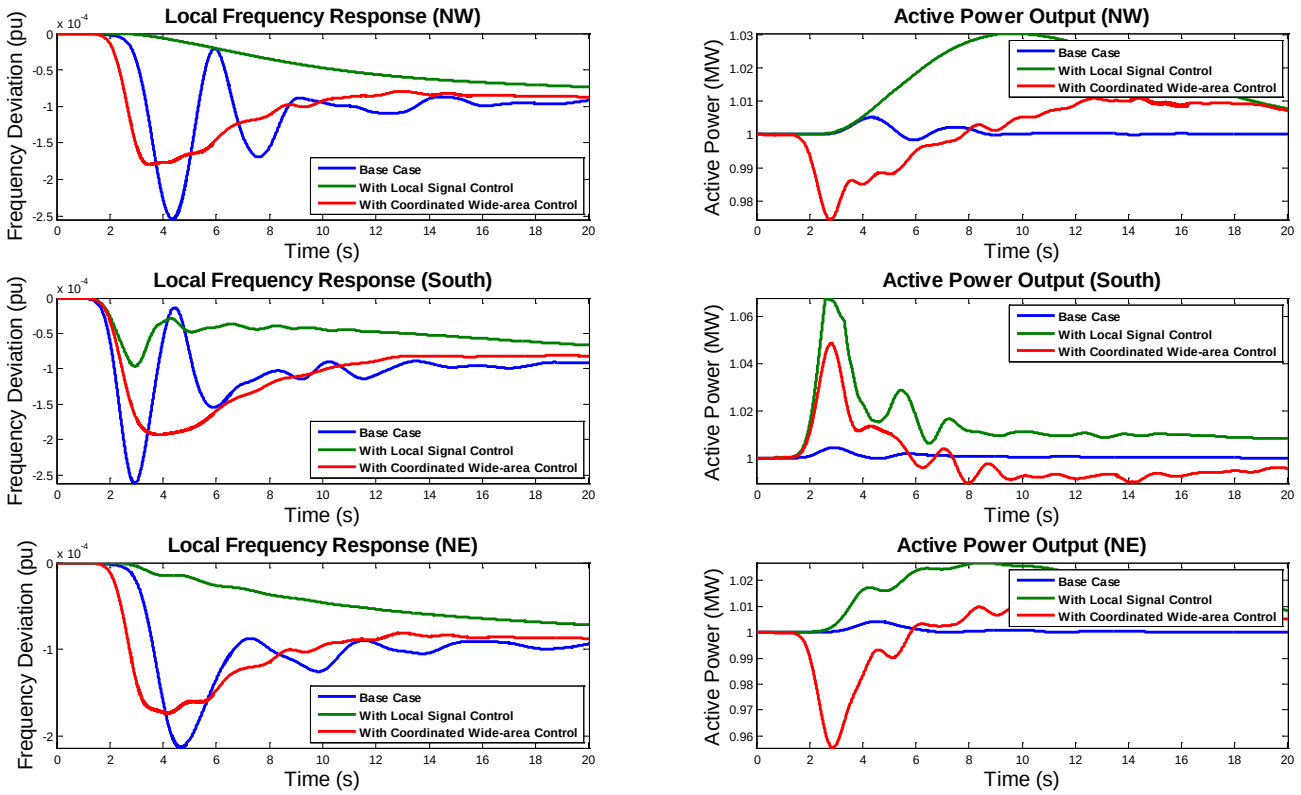

Figure 3-22 Wind Generator Active Powers and Local Frequency Responses using Coordinated Wide-area Wind PSS Control

3.5.5 Inter-area Oscillation Damping Movie Display

To demonstrate the overall effect of coordinated wide-area wind PSS control on the EI inter-area oscillation damping, a movie is also made based on the EI simulation data, one snapshot of which is given below in Figure 3-23. From this snapshot, it's clear that the EI inter-area oscillations can be damped effectively with the wide-area wind PSS control.

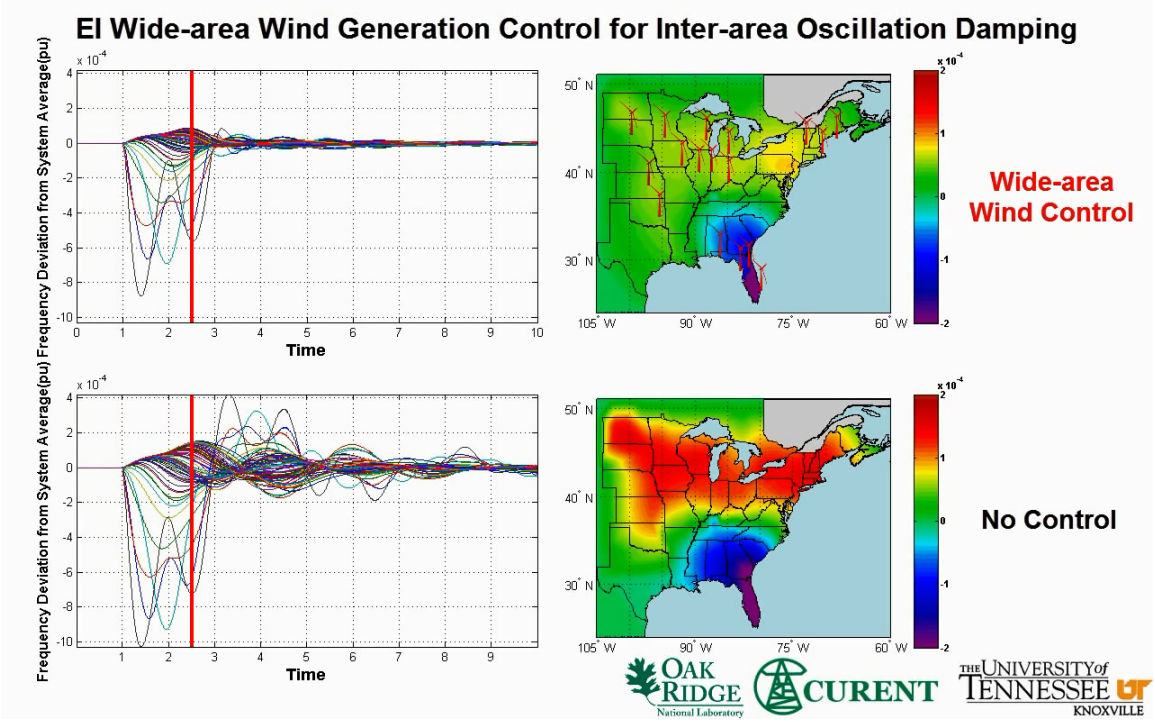

Figure 3-23 Movie Display of the Coordinated Wide-area Wind PSS Control for the EI Inter-area Oscillation Damping

3.5.6 Discussion

Though promising as shown in this section, only very traditional controller design is employed in this study so far. The controller design definitely needs to be improved and

the parameters need to be optimized. Furthermore, the majority of wind generation capacity is located in the Northwest the EI, which means only the oscillation involved by Northwest may be well damped. However, with the planned off-shore wind farms in Northeast and South of the EI system, wind generators has great potentials in the EI system oscillation damping.

3.6 Conclusions

In this chapter, several fast active power controllers, including wind inertia control, wind governor control, wind AGC control and wind PSS control, were developed and employed in the user-defined PSS/E DFIG electrical control model. Using the 16,000-bus EI system as the test-bed, the potential contributions of variable-speed wind generators to the EI frequency regulation and oscillation damping were evaluated. As demonstrated by the simulation results, though wind generation penetration is still very low, variable-speed wind generation already has the capability to effectively contribute to the frequency regulation and oscillation damping in the EI. If wind generation finally supplies 20% of the U.S. electric energy by 2030, wind generation will be the game-changer of the frequency regulation service market. Moreover, considering the fact that many other bulk power systems around the world have the similar wind penetration profiles, the control strategies discussed in this chapter also holds great merits for them.

Chapter 4 WIDE-AREA CONTROL OF PV PLANTS FOR FREQUENCY REGULATION AND OSCILLATION DAMPING IN THE EASTERN INTERCONNECTION (EI)

4.1 Introduction

Solar photovoltaic (PV) generation is another important category of renewable energy sources. Originally limited by the low efficiency of silicon solar cells, the capacity of PV system remained as low as kW-level and could only be treated as distributed generation (DG) in the local microgrids [47]-[51]. However, because of the dramatic enhancement of silicon solar cell technology in the recent years, the capacity of single PV plant finally reaches 100 MW-level now [52] and thus PV generation is widely expected to be able to reach a high penetration in the future generation mix. In fact, PV generation is gradually catching up the electric power market and their penetration has been steadily increasing in the U.S. now. Especially considering that the amount of solar energy reaching the Earth is more than 10,000 times the current energy consumption of human beings, solar energy and PV generation has been considered by some researchers as the ultimate solution to the energy problem.

Similar to variable-speed wind generators, maximum power point tracking (MPPT) operation of PV plant has been extensively studied by the academia in order to realize the maximum power extraction from PV panels [53]-[57]. And naturally, under MPPT operation mode, PV plants do not participate in any frequency regulation or oscillation damping service for the bulk power grid since they are not synchronized with the grid.

As discussed in Chapter 3, variable-speed wind generators may work in the “over-speed” zone instead of MPPT mode in order to retain some power reserve for frequency regulation and oscillation damping. And as shown by the simulation results in Chapter 3, variable-speed wind generators have great potentials to contribute to the EI system frequency regulation and oscillation damping even at a relatively low penetration (5%).

Thus, with the increasing penetration, it will also be beneficial to include PV plants in the bulk power system frequency support and small-signal stability control.

One important feature of PV generation system is that, unlike wind and conventional generators, it does not involve any rotating mechanical parts, and fully relies on the power electronic inverter/converter interface to be interconnected to the grid. Therefore, it means PV generation system inherently has a very small time constant and thus the significant capability to participate in frequency support and small-signal stability. As depicted by the P-V characteristic of PV panel in Figure 4-1, the active power of PV panel can be controlled flexibly by adjusting the output voltage. Again, due to the fast response speed of power electronics devices, PV plant's active power output can be controlled in a fast manner. Similarly, to retain some power reserve for frequency support and oscillation damping, PV plant needs to work in the "de-load" mode instead of MPPT operation mode (which is referred to as "over-voltage" in Figure 4-1, where P is the generated power by PV panel and V is the PV panel output voltage). In this way, the retained power reserve ΔP can be utilized to improve frequency regulation and oscillation damping in the bulk power system.

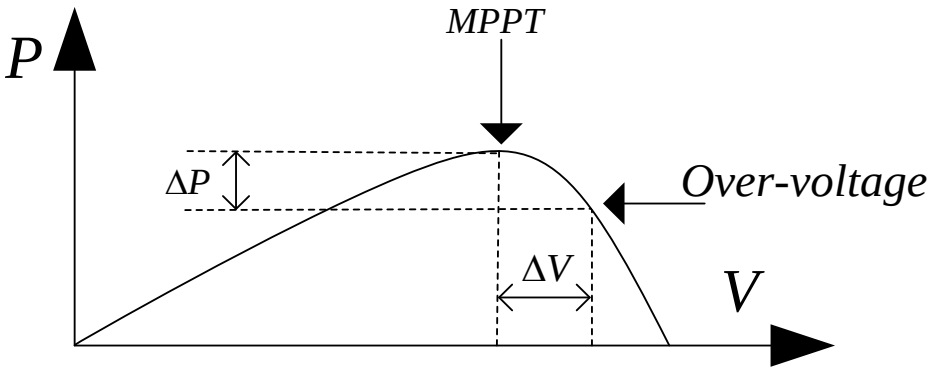

Figure 4-1 Over-voltage Working Condition of PV Panel

4.2 PV Plant Model

In order to investigate the role that PV generation may play in the EI system frequency regulation and oscillation damping, PV generation needs to be modeled in the EI model in PSS/E. In PSS/E version 32, due to the structure similarity between solar PV plant and PMSG wind generator, the solar PV unit dynamic stability model was developed in PSS/E based on the WT4 PMSG model to simulate the performance of PV plant connected to the grid via a power converter [43]. As depicted by Figure 4-2 [43], the PV generic wind model may include the following modules:

- PVGU: power converter/generator model
- PVEU: electrical control model
- PANEL: linearized model of a panel's output curve
- IRRAD: linearized solar irradiance profile

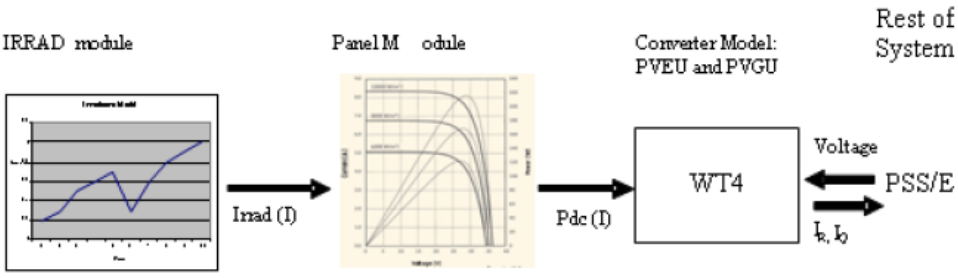

Figure 4-2 PV Model Connectivity Diagram

Apparently, IRRAD module introduces the impact of solar irradiance into the dynamic simulation. However, since this study only focuses on the short-term (tens of seconds-level) PV plant control, solar irradiance is unlikely to change dramatically for a large PV plant and thus the modules of IRRAD and PANEL are not included in this chapter's simulations.

To achieve the wide-area control of PV plant's active power output for frequency regulation and oscillation damping, additional controllers need to be designed and incorporated into the current PV electrical control module. Similar to what has been done in Chapter 3, a user-defined PV electrical control module that incorporates additional active power controllers is developed by the author in this chapter, whose active power control part is shown in Appendix C. Note that typical parameters from PSS/E are employed.

4.3 Contribution of PV Plants to the EI Frequency Regulation

Similar to the frequency regulation control of variable-speed wind generators, several active power control techniques are employed in the user-defined PSS/E PV electrical control model in order to enable PV plants engage in frequency regulation, including PV inertia control, PV governor control and PV AGC control.

4.3.1 PV Inertia Control

The PV inertia control here is of the same structure as wind inertia control introduced in Chapter 3, whose objective is to allow PV plants to provide the "artificial" inertial response. Again, droop control is utilized to produce active power output change that is proportional to the frequency deviation. The structure of PV inertia droop control is shown in Figure 4-3. The only difference between PV inertia droop control and wind inertia droop control is that the output of this controller is the change of active power order ΔP_{ref} for PV plant, not current command ΔI_P in the wind case.

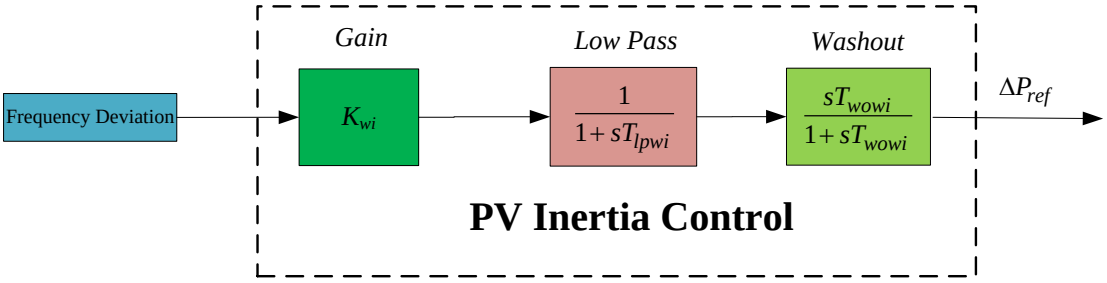

Figure 4-3 PV Inertia Control Structure

4.3.2 PV Governor Control

As discussed in Chapter 3, if working in "over-speed" zone, wind turbines can decrease their rotational speeds to release the power reserve in seconds and therefore, governor response can be emulated for wind generators utilizing the wind reserve. Similarly, if working in "over-voltage" zone, PV panel can decrease its output voltage to release the retained power reserve to emulate the governor response. The structure of PV governor controller is shown in Figure 4-4. Again, the output is active power order change ΔP_{ref}.

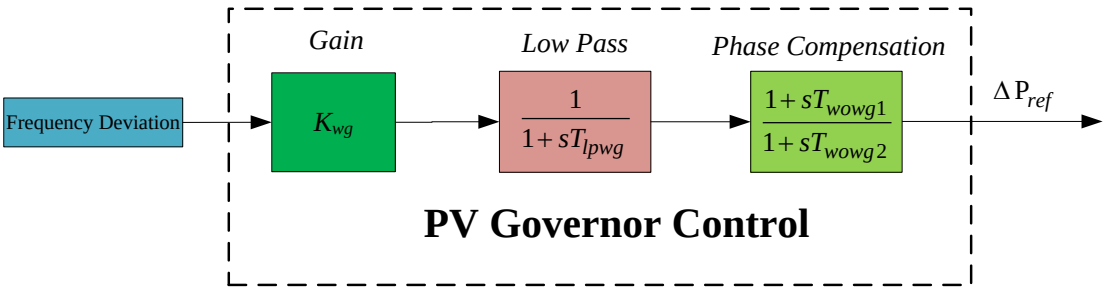

Figure 4-4 PV Governor Control Structure

4.3.3 PV AGC Control

As demonstrated by Chapter 3, variable-speed wind generators can also respond to the

AGC regulation order from the operators as effectively as conventional generators if reserve exists. Because of the fast response speed of power electronics converters, PV generation can also realize the AGC control easily, even faster. The only disadvantage is still the waste of reserve during normal operation conditions.

4.3.4 Case Study-Generation Trip

To demonstrate the effectiveness of the frequency support of PV plants, a generation trip in the EI (with 5% PV penetration) is simulated in this section as a case study. Figure 4-5 describes the frequency responses of the EI with different PV control schemes while in Figure 4-6 one typical PV plant's active power outputs are given.

Depicted by the green line in Figure 4-5 and Figure 4-6, PV inertia control can significantly reduce the frequency drop nadir by increasing the PV plant's active power temporally in the several seconds following the disturbance, but not help with the longer-term frequency recovery since the increased active power gradually diminish due to the control. Comparatively, if only with PV governor control (red line), PV plant is able to reduce not only the frequency drop nadir but also the long-term frequency deviation compared to the base case, because the existence of "governor" function propels the PV generation to generate an active power increase that is proportional to the frequency deviation. Of course, the active power increase is physically limited by the amount of reserve available.

Though the combination of PV inertia control and PV governor control does improve the frequency response further (light green line), it reveals that PV AGC control is still highly desirable since PV plants have the ability to respond to AGC regulation order in an unprecedentedly fast manner. From Figure 4-6, after receiving the AGC order at 10-th second, the active power of PV generation rises to its new operating point almost immediately due to the fast speed of power electronics devices.

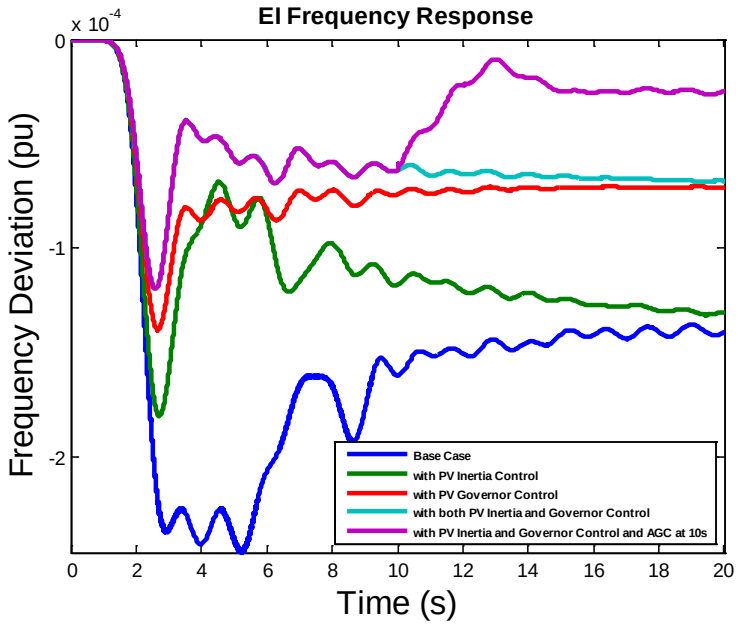

Figure 4-5 Frequency Responses of the EI after a Generation Trip with Different PV Controls

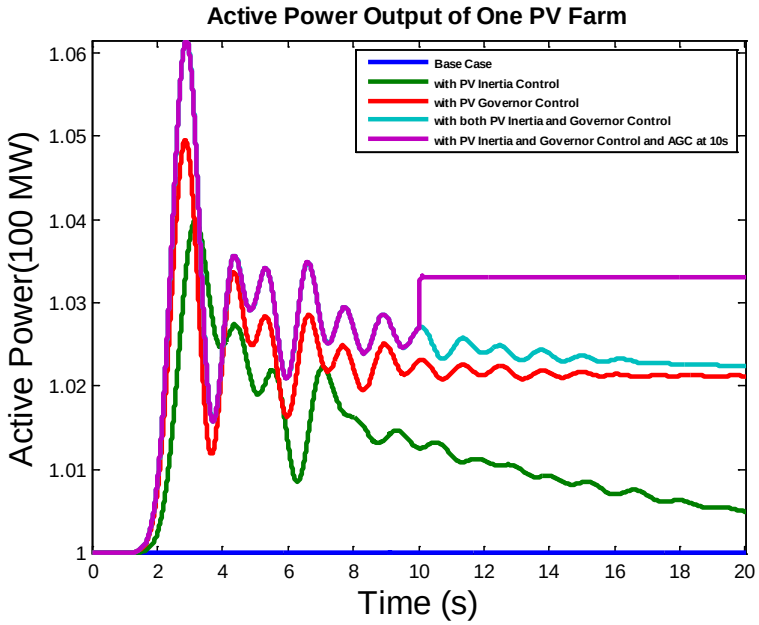

Figure 4-6 Active Power Outputs of a Typical PV Plant after a Generation Trip with Different PV Controls

4.3.5 Case Study-Load Shedding

Note that PV plant can also contribute to the frequency response improvement in the load shedding cases. In this scenario, instead of decreasing PV panel voltage and release the reserve, the panel voltage is increased to retain more reserve so that the frequency excursion will be reduced. To demonstrate this, a load shedding event of 724 MW is simulated in the EI. Similar to the generation trip case, power system frequency response and PV active power are given below in Figure 4-7 and Figure 4-8, respectively.

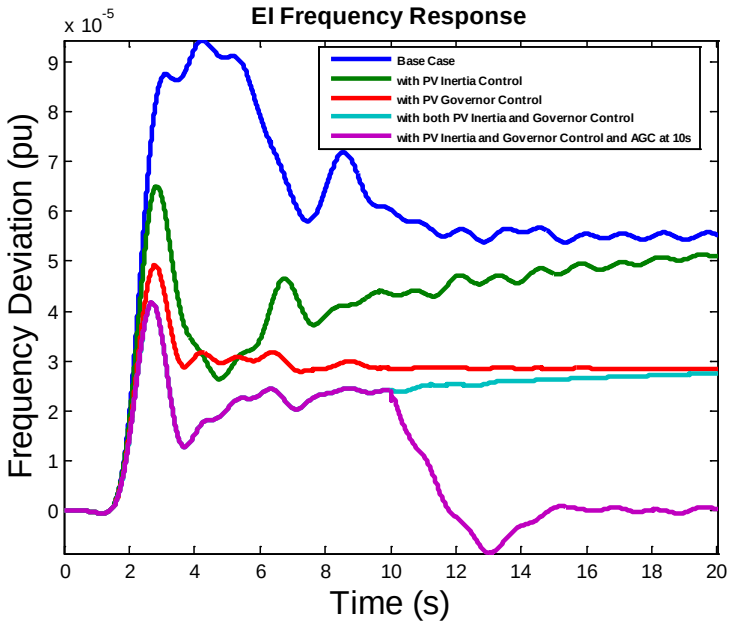

Figure 4-7 Frequency Responses of the EI after a Load Shedding with Different PV Controls

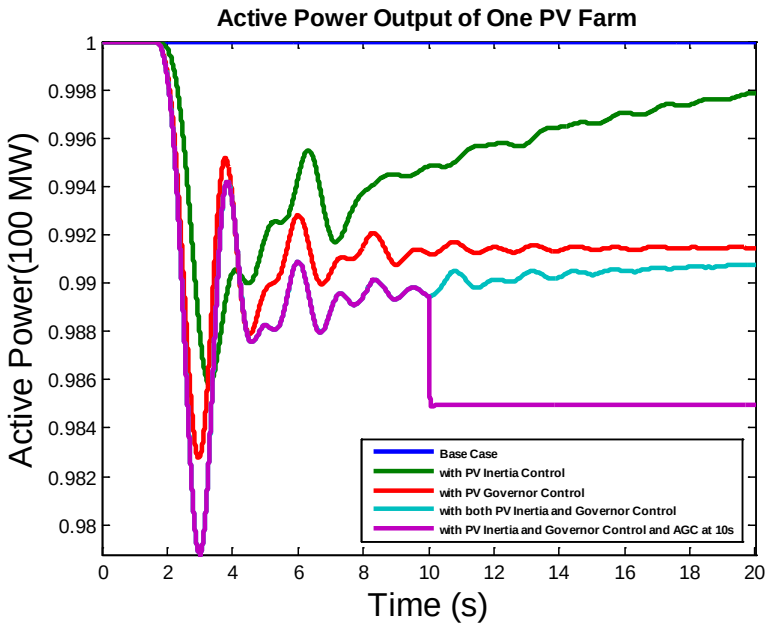

Figure 4-8 Active Power Outputs of a Typical PV Plant after a Load Shedding with Different PV Controls

4.4 Contribution of PV Plants to the EI Oscillation Damping

Besides the frequency regulation, oscillation damping is another important contribution that PV plant can make if with appropriate control schemes. Employing the same inter-area oscillation damping strategies developed in Chapter 3, the great potential of PV plant in the EI inter-area oscillation damping will be demonstrated in this section. The same disturbance (a generation trip of 814 MW) in Chapter 3 is simulated in the Florida region of the EI to incite the oscillations between Northwest and South (NW-South), and between Northeast and South (NE-South). The inter-area oscillation damping result using the coordinated wide-area PV control is shown in Figure 4-9. From the results, if with coordinated wide-area PV PSS control, the inter-area oscillation can be damped almost completely. One snapshot of a movie showing the overall damping effect of PV PSS is also given below in Figure 4-10.

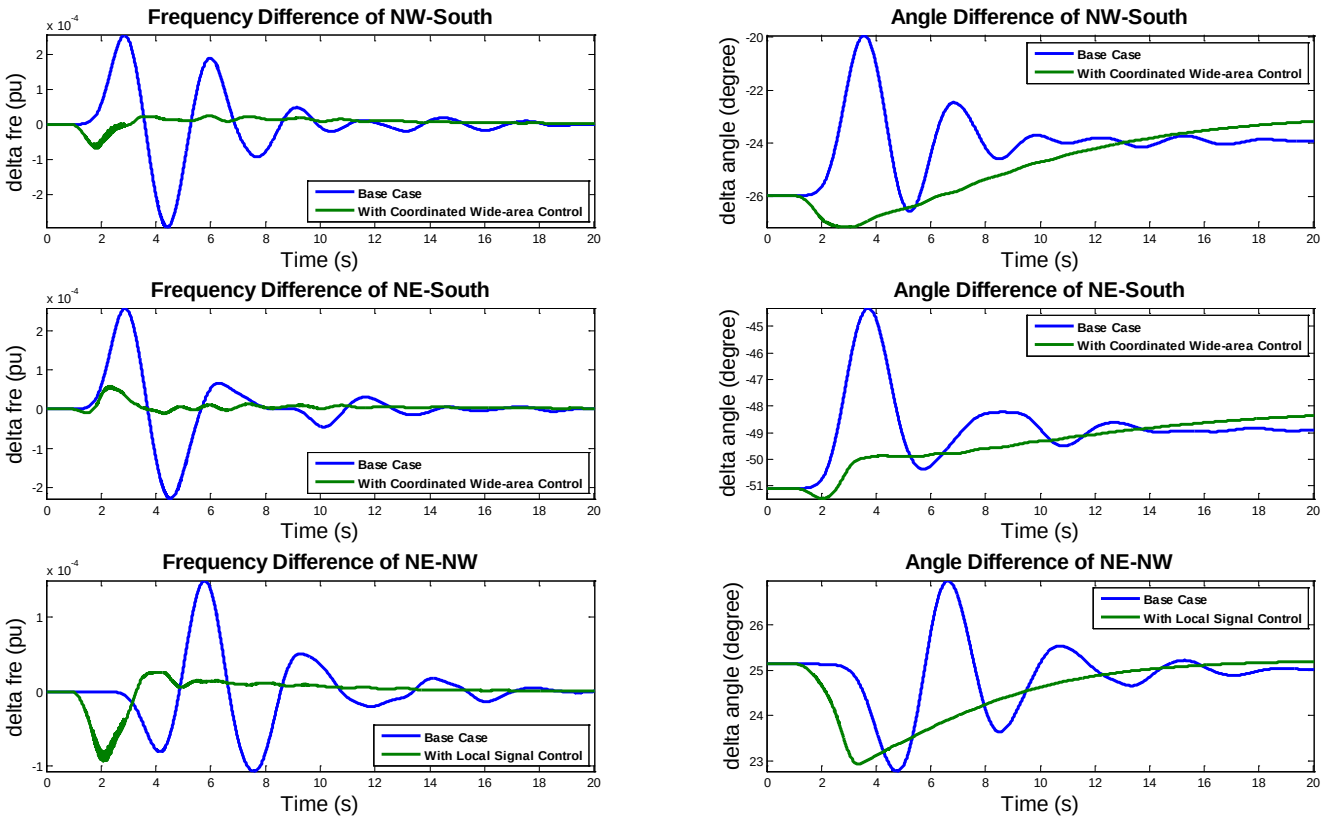

Figure 4-9 Inter-area Oscillation Damping using Coordinated Wide-area PV PSS Control

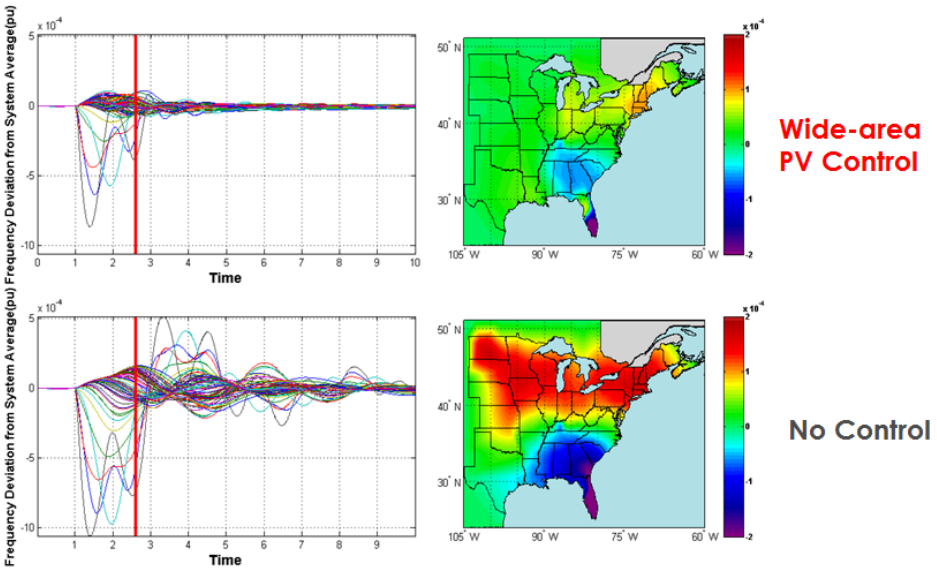

Figure 4-10 Movie Display of the Coordinated Wide-area PV PSS Control for the EI Inter-area Oscillation Damping

4.5 Comparison between Wind and PV Controls in Frequency Regulation

In this section, the characteristics of wind and PV generators will be compared in order to understand them thoroughly and develop corresponding strategies in the future EI system frequency regulation.

4.5.1 Comparison between Wind and PV Inertia Controls

Wind inertia control enables the wind generator increase its active power temporally in the several seconds (2-8s in Figure 4-11) following the generation trip by use of the kinetic energy stored in the wind blades. However, this active power increase cannot be sustained and after the temporal active power surge, the wind generator active power output would go through a “dip” (10-20 seconds in Figure 4-11), during which the inertial energy of the turbine blades is “recharged”. At the same time, the turbine speed goes through the phase of “deceleration” to “discharge” the kinetic energy and the phase

of “acceleration” to “recharge”. Unlike variable-speed wind generators, PV plant with the same inertia control scheme acts in a different way. Fully depending on the reserved solar power and the adjustment of PV panel output voltage to provide the inertial response for frequency support, PV plant doesn’t have a “dip” of active power output as wind generators. As a result, the EI frequency response with the PV inertia control also does not have an obvious “dip” (blue line in Figure 4-11).

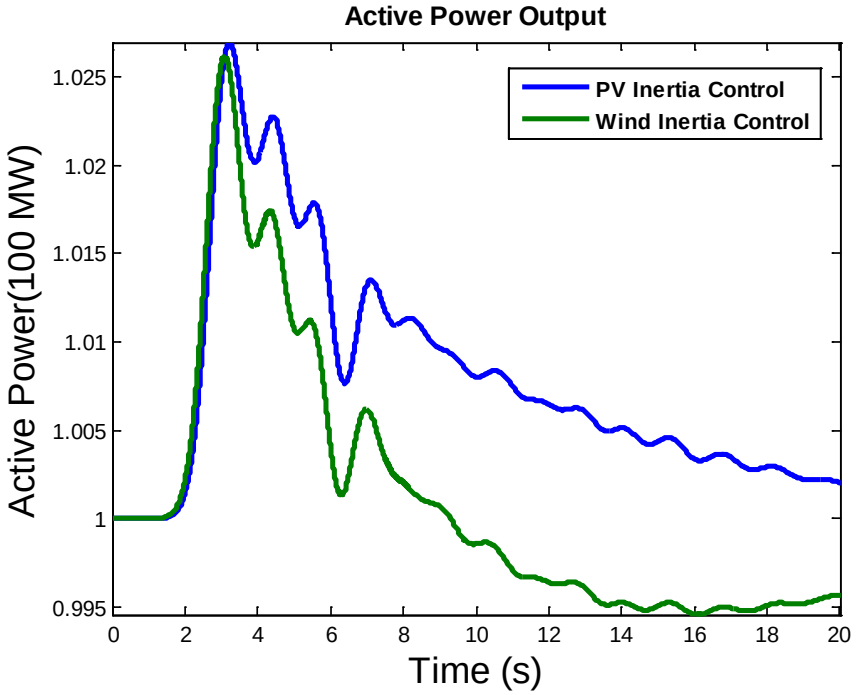

Figure 4-11 Comparison between Wind and PV Inertia Control-Active Power

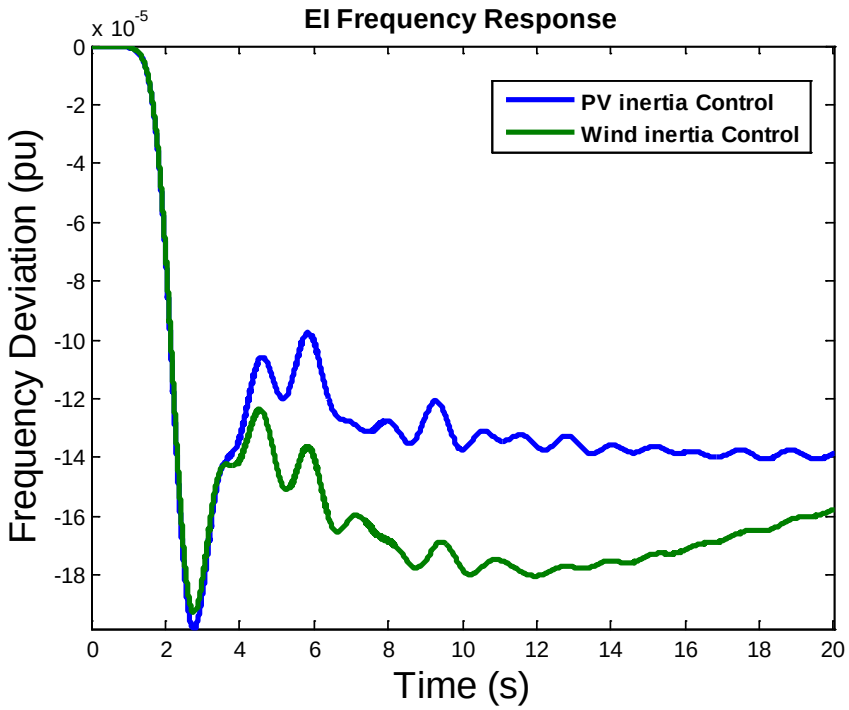

Figure 4-12 Comparison between Wind and PV Inertia Control-Frequency Response

4.5.2 Comparison between Wind and PV Governor Controls

In this subsection, the performance of wind and PV generators with the proposed governor control will be compared. The time constant of wind generators is expected to be much larger than PV due to the involvement of rotating mechanicals such as the wind turbines. This time constant difference should be reflected in the comparison between wind and PV governor controls. In Figure 4-13, due to the same droop parameter of wind and PV governor control, the final active power increases in two cases are identical. However, wind and PV display the totally different dynamics. Due to the small time constant, PV plant acts to the frequency change much more promptly than the wind generator, and thus proves to be more effective in reducing frequency drop nadir. Furthermore, it's interesting to point out that, PV governor control can also help damp the frequency oscillations to some extent, as shown by Figure 4-14.

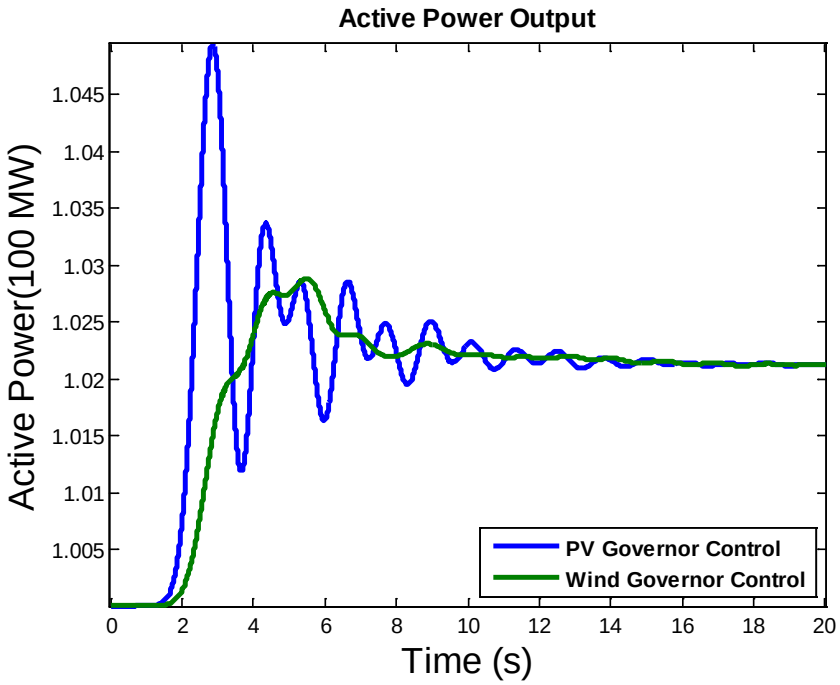

Figure 4-13 Comparison between Wind and PV Governor Control-Active Power

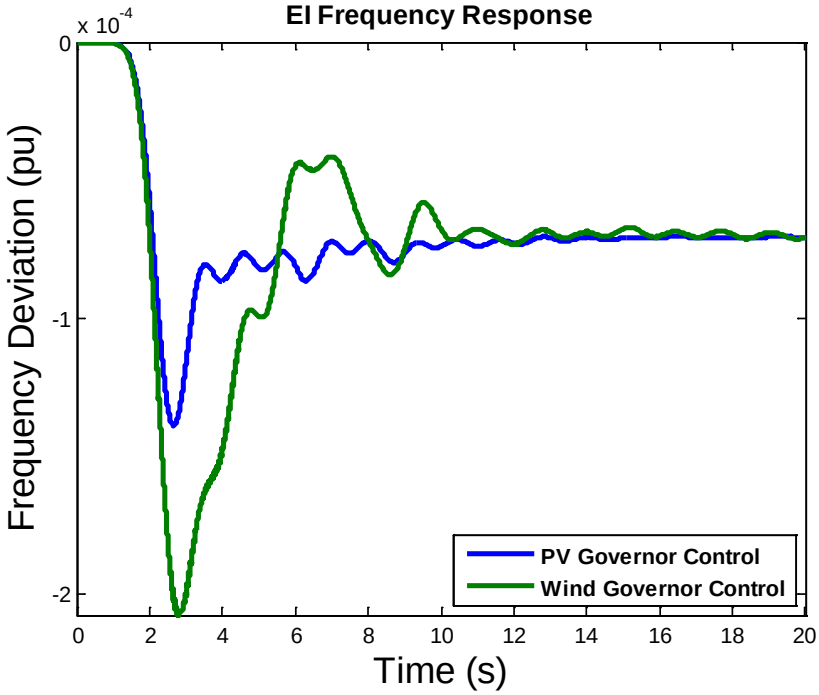

Figure 4-14 Comparison between Wind and PV Governor Control-Frequency Response

4.5.3 Comparison between Wind and PV AGC Controls

The effect of the smaller constant of PV plant is even more obvious in the AGC control cases. In Figure 4-15, after receiving the AGC control signal, it takes about 10 seconds for the wind generator to finally reach its new operating point, which is already much faster than the conventional generators. However, for PV plant, it almost manages to change to the new operating point immediately after receiving the AGC order, which demonstrates the great effectiveness of PV AGC control.

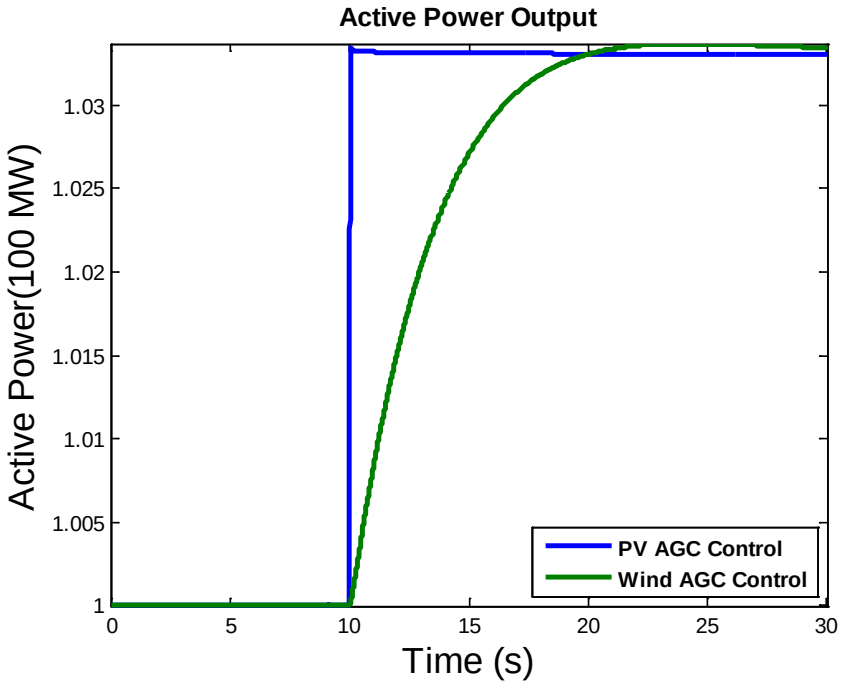

Figure 4-15 Comparison between Wind and PV AGC Control-Active Power

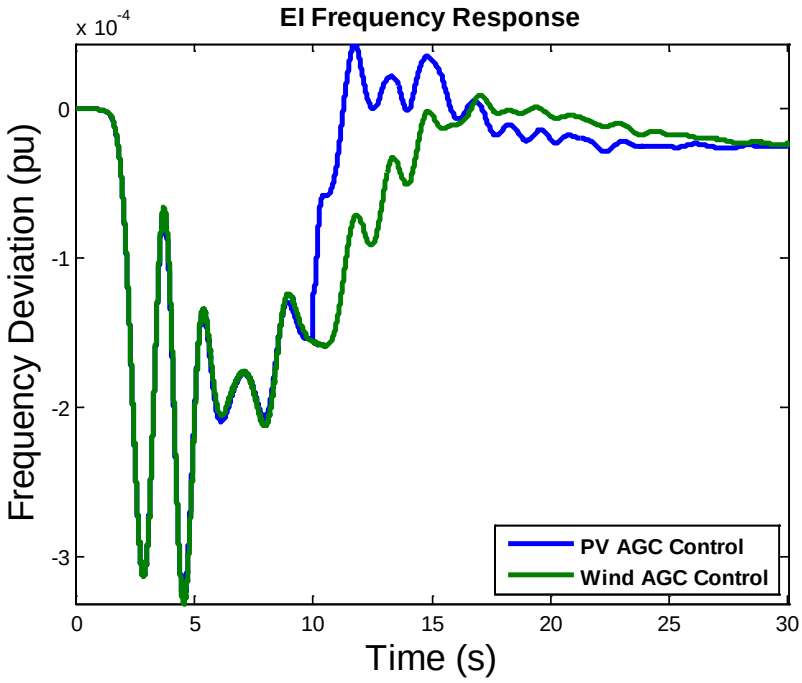

Figure 4-16 Comparison between Wind and PV AGC Control-Frequency Response

4.6 Construction of the EI Simulation Scenarios with High Penetrations of Renewable Energy Resources

In all the previous case studies, the EI simulation scenarios with 5% wind or PV penetration have been utilized to evaluate the potential contributions of variable-speed wind or PV generators to the EI system frequency regulation and oscillation damping. However, in the future the penetration of renewable energy resources in the EI is expected to far exceed 5%. Therefore, the EI simulation scenarios with high penetrations of renewable generation are highly desirable.

The similar method used in the 5% penetration simulation scenario was still used in this section: a certain portion of active power output of a selected list of conventional generators is converted to wind or PV generators, but the reactive power remains unchanged. In this way, voltage stability problem is unlikely to occur. Based on the

author's 16,000-bus EI system simulation experience, there are some other guidelines that should be noted in order to avoid numerical instability:

1. No more than 50% of the active power should be converted to renewables.

2. Generators whose capacity exceeds 1500 MW should not be converted.

3. Wind and PV generators may not be attached to the same bus.

Note that the guidelines are just for the 16,000-bus EI model. So far, the simulation scenario with 20% penetration of wind or PV has proved to be numerically stable.

4.7 Conclusions

Based on the 16,000-bus EI model and the user-defined PV generator electrical control model, a relatively realistic scenario of the EI with PV penetration was utilized to evaluate the potential contributions of PV plant to the EI system frequency regulation and oscillation damping. Simulation results demonstrate that current and future penetrations of PV system are promising in providing frequency regulation and oscillation damping service in the EI system.

Chapter 5 MEASUREMENT-BASED DYNAMIC MODELING

Dynamic models of power system play a vital role in power system planning and operations. An accurate dynamic model should be able to faithfully reveal system responses to different disturbances and help establish an accurate stability boundary so that a grid can be operated at its full capacity while staying within the stability region. Therefore, the construction and validation of power system dynamic models has always been a focus of researchers and engineers [58]-[59]. However, traditional power system simulation models can be very complex and inaccurate due to the intricacies of power system networks, not to mention that the power system topologies constantly change as breakers open or close, lines are taken out of service and generators are re-dispatched. In the present power grid operating paradigm, the detailed dynamic models are usually updated once every few months or less often, and thus, discrepancies in simulation models limit the performance of online applications for power system stability and control.

On the other hand, even for a high-dimensional complex power system, only a limited number of transfer functions (or models) of the system are critical to determine its stability and control actions [58], which means a reduced power system model may be developed and identified online for stability analysis and control purposes. Especially with the availability of a large number of synchrophasors being deployed, it is possible to dynamically construct that reduced power system model based purely on real-time synchrophasor measurements in order to reflect the most recent changes in the system.

In this chapter, the approach for creating a reduced power grid dynamic model by means of the autoregressive with exogenous input (ARX) model structure will be proposed. That grid model will be purely based on the synchrophasor measurements and identified by regressive least-square (RLS) technique to reflect the recent changes that occur in the bulk power system. Unlike the traditional linear system model around an operating point which is derived from nonlinear equations with some simplifications and constraints, the proposed model is able to overcome the computational burden and modeling errors when

it comes to the large-scale power systems. Assuming the operation point of the bulk power grids does not change dramatically, that model is expected to have good accuracy and fast speed needed for dynamics estimation and control [60]-[61].

This chapter is structured as follows: after a brief introduction of the ARX model structure and a preliminary power system linearity study, a concept of dynamic response estimation will be presented; then, a series of influencing factors, such as the locations and numbers of model inputs, will be examined and real synchrophasor measurement data will be utilized to validate the proposed method; last but not the least, this chapter will also explore the proposed model's potential applications in the early warning of power system instability issues.

5.1 Algorithm for ARX Model

As a generalized linear model structure, the ARX model provides a much simpler model identification method of a multi-variable system than state-space and other models [62]. The mathematical structure expression of the ARX model is given below:

$$\boldsymbol{A_k(z)\hat{y}_k(t) = \sum_{j=1}^{n_j} B_{jk}(z)u_j(t) + e(t)} \quad 5\text{-}1$$

where t is the sampled data number, j and k are the numbers of model inputs and outputs, $e(t)$ is the system noise, u_j and $\hat{y}_k$ are the model's j-th input and k-th output. $A_k(z)$ and $B_{jk}(z)$ are the ARX nominator and denominator polynomials respectively, which are given by:

$$\boldsymbol{A_k(z) = 1 + a_{k1}z^{-1} + \cdots + a_{kn_{a_k}}z^{-n_{a_k}}} \quad 5\text{-}2$$

$$\boldsymbol{B_{jk}(z) = b_{jk0} + b_{jk1}z^{-1} + \cdots + b_{jk(n_{b_{jk}}-1)}z^{-(n_{b_{jk}}-1)}} \quad 5\text{-}3$$

where n_{a_k} and $n_{b_{jk}}$ are the orders of the model. The model parameters of a multi-variable ARX model can be estimated by the regressive least-squares technique. The least-squares estimation problem is solved by means of QR factorization to optimize the ARX model parameters and the least-squares loss function is defined as:

$$\boldsymbol{V_{LS} = \sum_{t=n_s+1}^{N} \varepsilon_{ARX}(t)^2} \quad 5\text{-}4$$

where the equation error criterion $\mathcal{E}_{ARX}(t)$ is described by:

$$\boldsymbol{\varepsilon_{ARX}(t) = A_k(z)y_k(t) - \sum_{j=1}^{n_j} B_{jk}(z)u_j(t)} \quad 5\text{-}5$$

The details of ARX structure and algorithm are discussed in [62]. After obtaining the model orders and parameters, the identified models can be evaluated by comparing their outputs with the actual system outputs.

5.2 Power System Linearity Study

As discussed above, the application of the ARX-structured modeling method is under the assumption that the power system to be modeled is relatively linear around certain operation points. Though the electric power grid is a nonlinear system in nature, the operating point of the large-scale power system (such as the EI) does not change dramatically, which means the bulk power grids show linear characteristics in most of the time and thus the ARX-structured method enjoys great potentials in bulk power grid dynamic modeling. However, it's still necessary to study the linearity of bulk power grids in order to guarantee the validity of the proposed method.

Since it's difficult to quantify the power system linearity directly, an indirect method to test the power system linearity is explained in this section. Assuming there exists a bus with synchrophasor measurement (which is referred to as monitoring bus in this case study) in the Tennessee region, four pairs of disturbances are created in the 16,000-bus EI model based on their distances to the monitoring point (as shown in Figure 5-1). Please note that all the disturbances are of the similar magnitudes. For each pair, the two disturbances are simulated individually first, and then a simulation that includes both disturbances is carried out. Apparently, if the perfect linearity exists, the sum of two individual disturbances' responses should be identical to the response of the simulation that includes both events.

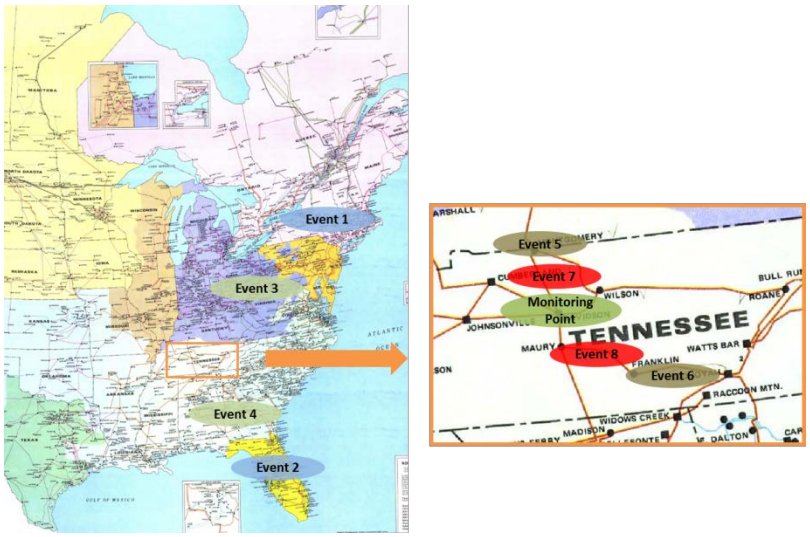

Figure 5-1 Disturbance Locations for the Bulk Power Grid Linearity Study

The simulation results based on event 1 and 2 are given in Figure 5-2. It can be seen that, no matter frequency, voltage magnitude or angle, the simulation result of event 1 and 2 together is almost identical to the sum of the two individual events' simulation results, which means the linearity of the monitoring point is high if the disturbance is far away enough. Similar conclusions can also be drawn based on the simulation results of event 3 and 4 (as shown by Figure 5-3).

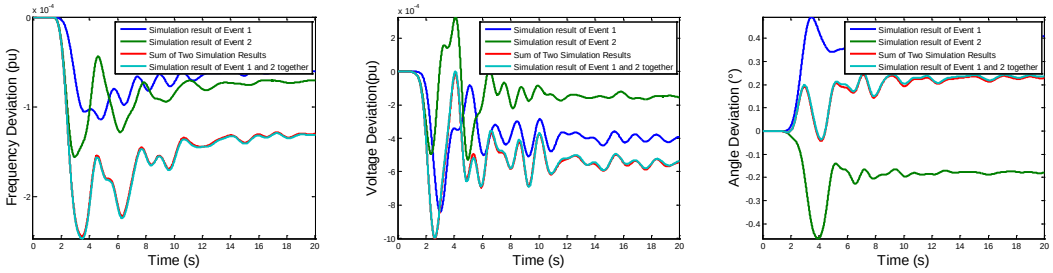

Figure 5-2 the Monitoring Point's Linearity after Event 1 and 2

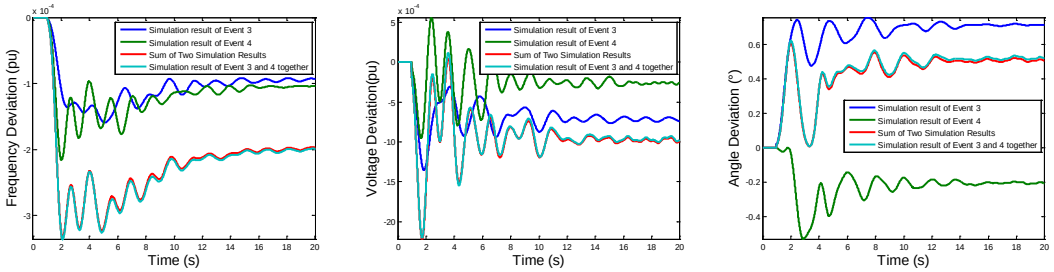

Figure 5-3 the Monitoring Point's Linearity after Event 3 and 4

However, if the disturbances are not far away enough from the monitoring point, like event 5 and 6, the linearity of the monitoring point may not be as strong as the previous cases. In Figure 5-4, though both frequency and angle still show the strong linearity, the voltage case has started to show some extent of nonlinearity, since the voltage result of event 5 and 6 together apparently differs from the sum of two individual events' simulation results. Therefore, it's possible to draw out a voltage nonlinearity zone around the monitoring point (as shown by Figure 5-5). Beyond this voltage nonlinearity zone, the disturbances of similar magnitudes won't influence the linearity of the monitoring point's voltage.

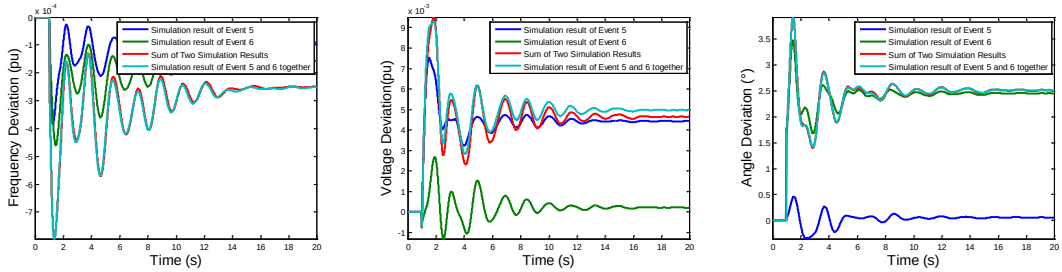

Figure 5-4 the Monitoring Point's Linearity after Event 5 and 6

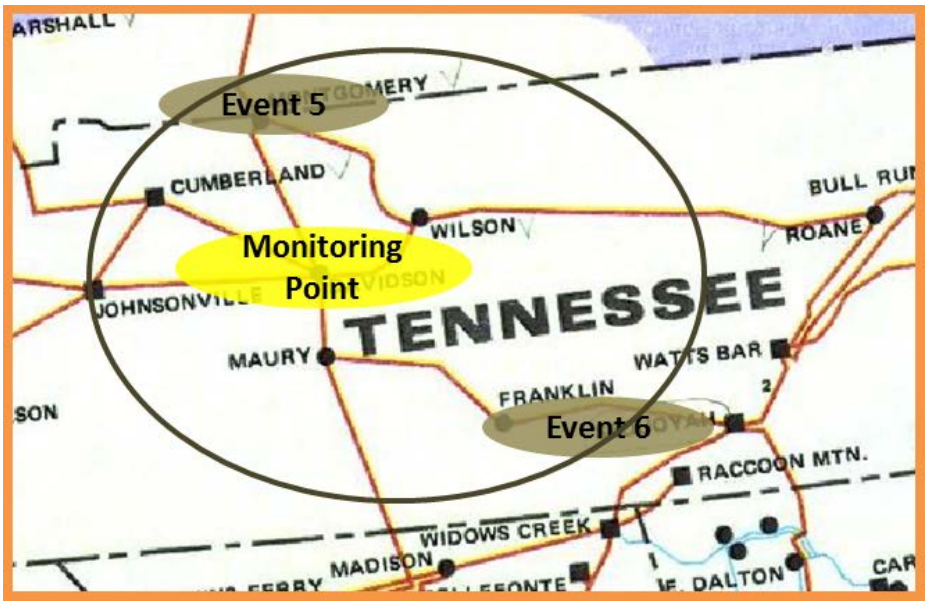

Figure 5-5 Voltage Nonlinearity Zone around the Monitoring Point

As shown by Figure 5-1, event 7 and 8 are even closer than event 5 and 6. Since event 7 and 8 are already in the voltage nonlinearity zone, it's understandable that the voltage response of event 7 and 8 together differs from the sum of two individual voltage responses. At the same time, the angle case also starts to show the discrepancy, which means event 7 and 8 probably lie on the border of the angle nonlinearity zone (as shown by Figure 5-7).

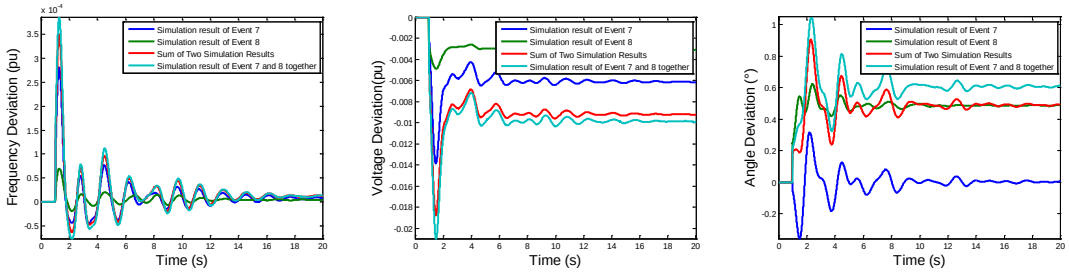

Figure 5-6 the Monitoring Point's Linearity after Event 7 and 8

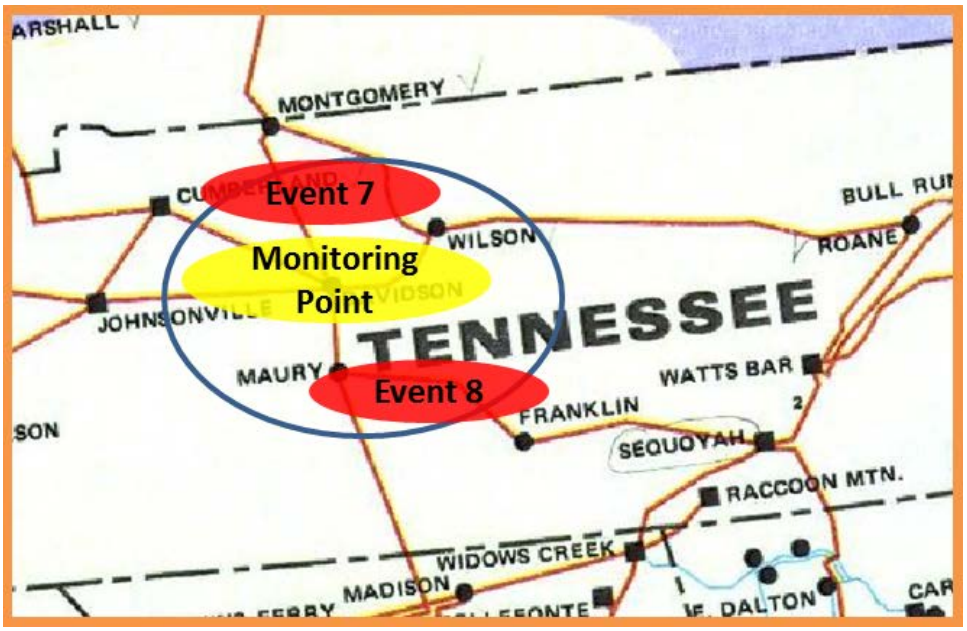

Figure 5-7 Angle Nonlinearity Zone around the Monitoring Point

Though the linearity study in this section is very preliminary, it still proves that the linearity of certain area in the bulk power grid can be significant, thus lending great support to the application of linear structure in power system dynamic modeling. Furthermore, it should be pointed out that, based on the observation in this section, the frequency and angle's linearity seems to be stronger than voltage.

5.3 Dynamic Response Estimation

To achieve the goal of system dynamics estimation in the power system, a concept of dynamic response estimation is proposed in this section. Unlike traditional state estimation and dynamic state estimation techniques that focus on estimating relatively stationary state vectors such as bus voltage magnitudes during steady and quasi-steady states [63], dynamic response estimation seeks to estimate the dynamic response of a power system during transient situations. The basic idea of dynamic response estimation is to identify the real-time dynamic model or transfer function of the power system and

use the obtained model to estimate the power system's dynamic response. ARX model structure and least-squares techniques will be employed to identify the necessary dynamic model for response estimation.

The detailed procedure of the proposed dynamic response estimation method is illustrated by a specific example below. Assuming there are five high voltage buses located in the Tennessee area with synchrophasor measurements in the 16,000-bus EI system, which are shown in Figure 5-8, the basic steps of dynamic response estimation is 1) to identify the power system dynamic model between the "output bus" (green ones in Figure 5-8) and the "input buses" (yellow ones in Figure 5-8) using synchrophasor measurement data of certain contingencies, and 2) to use the trained power system dynamic model and the measurement data from the "input buses" to estimate the dynamic response of the "output bus" of other contingencies. The contingencies (or events) which data are used to train the model are referred to as the "excitation sources" of the model, whose locations are also indicated in Figure 5-8.

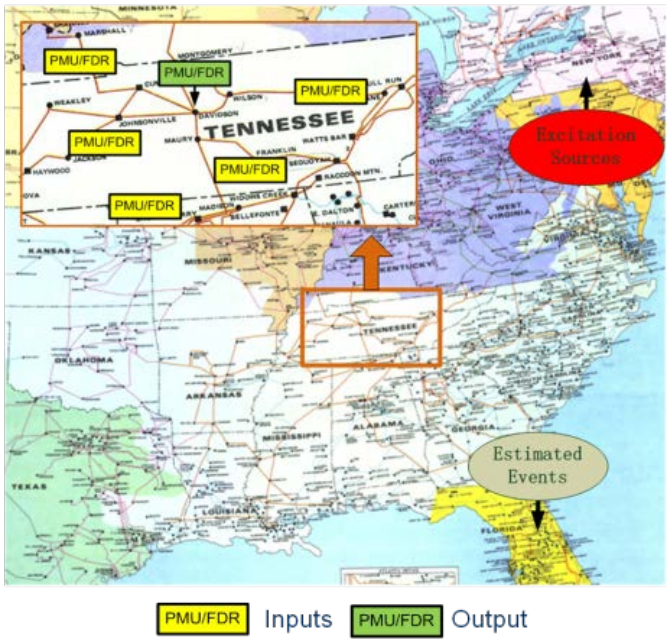

Figure 5-8 Illustration of Dynamic Response Estimation

5.4 Accuracy Index

As discussed above, a generalized linear model structure can be employed in the measurement-based model identification process to describe power system dynamics. In order to evaluate the identified models' quality, the model accuracy index defined below can be calculated for each output over a time window (assuming that the window has L data points):

$$\boldsymbol{Accuracy_k} = \left\{ \mathbf{1} - \frac{\sqrt{\sum_{l=1}^{L}[y_k(l)-\hat{y}_k(l)]^2}}{\sqrt{\sum_{l=1}^{L}[y_k(l)-\bar{y}_k]^2}} \right\} \times \mathbf{100} \qquad 5\text{-}6$$

where $y_k\,(l)$ and $\hat{y}_k(l)$ are the measured and estimated responses of the k-th output at the l-th data point, and $\bar{y}_k$ is the mean value of the measured response over the time window. This is the most widely used evaluation index in system identification [62]. It is mainly used to reflect the accuracy of the model in describing dynamic characteristics and thus suitable to describe the accuracy of the ARX model. The index of 100 means a perfect match between the estimated response and the measured response, and the model identified can fully reflect the dynamic characteristics of the system. If the index is 0, it means the estimated response is no better than the mean value of the measured response. In that case, the identified model cannot describe the system's dynamic characteristics.

When the state of the power system is around its stable equilibrium point and far enough from the boundary of instability, the power system should behave like a linear system. Then, the ARX model may achieve a high accuracy to estimate the power system responses. However, if the state of power system approaches the boundary of instability, the system will exhibit more nonlinearity in which case the accuracy index may be low. If the system loses stability, the accuracy index will probably be close to zero or even negative, which means the accuracy index may potentially be used as an indicator of the stability level of the system. In the later part of this chapter, the accuracy index will be calculated for two cascading outage scenarios that lead to angular and voltage instability.

5.5 Performance Test

In this section, a detailed examination will be introduced to test the reliability and accuracy of the proposed method. First, the influence of the model input numbers and locations will be discussed and then the real synchrophasor data provided by FNET will be utilized to validate this approach. Furthermore, an observability study is given in Appendix D. And the influence of "excitation source" types and locations on the model is respectively introduced in Appendix E and Appendix F. Please note that all the following case studies are based on the 16,000-bus EI model simulation results expect the real measurement validation part.

5.5.1 Influence of the Model Input Numbers

The number of model inputs is one important factor that influences the model accuracy. Generally speaking, increasing the number of inputs is able to improve the accuracy of the model to some extent [62]. However, it is highly likely that there exists a "saturation limit" for the number of inputs. Figure 5-9 shows one case study of how the model accuracy changes with the increase of the number of model inputs in all the frequency, voltage and angle estimation cases. Clearly, there indeed exists a "saturation limit" in all the estimation cases, beyond which the accuracy of the model does not improve significantly any more.

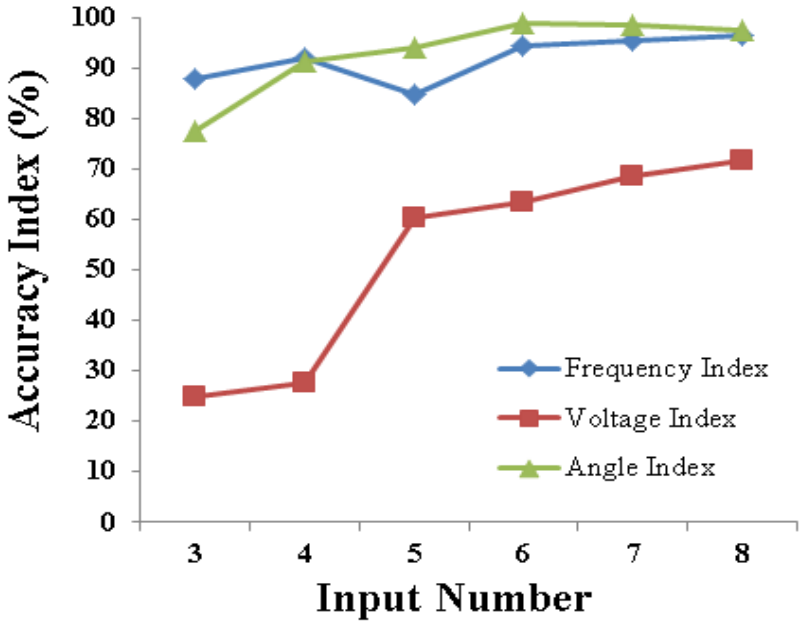

Figure 5-9 Accuracy Index Change with Different Numbers of Inputs

5.5.2 Influence of the Model Input Locations

It's understandable that the model input locations should also play a significant role in the model accuracy. In this subsection, four groups of input buses with different distances to the output bus are selected in the 16,000-bus EI model to give a case study. The input buses in group 1 are directly connected to the output bus by a 500 kV transmission line while groups 2, 3, and 4 are further and further away from the output bus. Considering the fact that all the input and output buses are all 500 kV high voltage buses, it means a long geographical distance between the inputs and output even it is only one transmission line away. The results of this case study are shown in Figure 5-10. For the frequency estimation case, it seems group 3 (three transmission lines away from the output bus) is still acceptable for the model inputs since it maintains the needed accuracy as well as the longest distance. For the voltage and angle cases, though the accuracy of the model does not strictly decrease with the increase of distance, the overall trend is that the accuracy of

the model is inversely proportional to the distance between the input buses and the output bus.

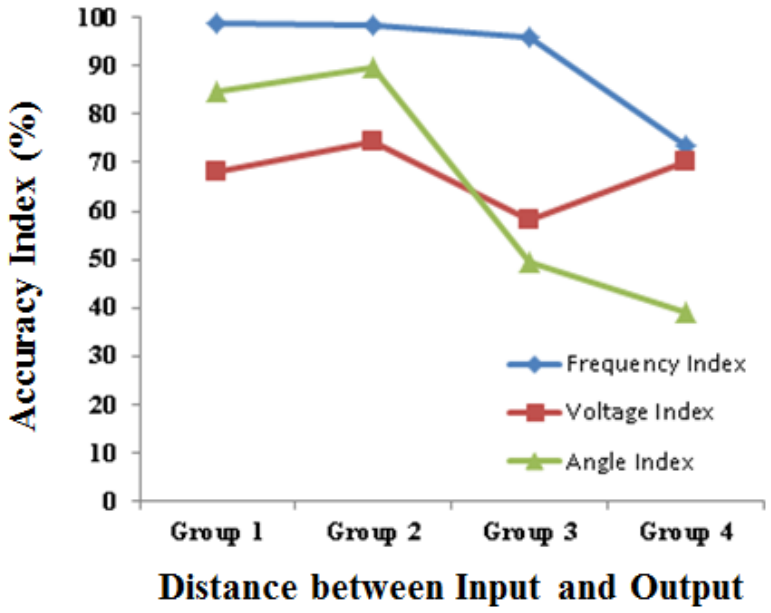

Figure 5-10 Accuracy Index Change with Different Distances between Inputs and Outputs

5.5.3 Method Validation Using Real Synchrophasor Data

Historical event data from FNET system are used to validate the proposed approach in this subsection. As shown in Figure 5-11, five FDRs deployed in the Michigan region are selected in this case study: four FDRs (the yellow ones in Figure 5-11) are considered as inputs and one FDR (the green one in Figure 5-11) as the output.

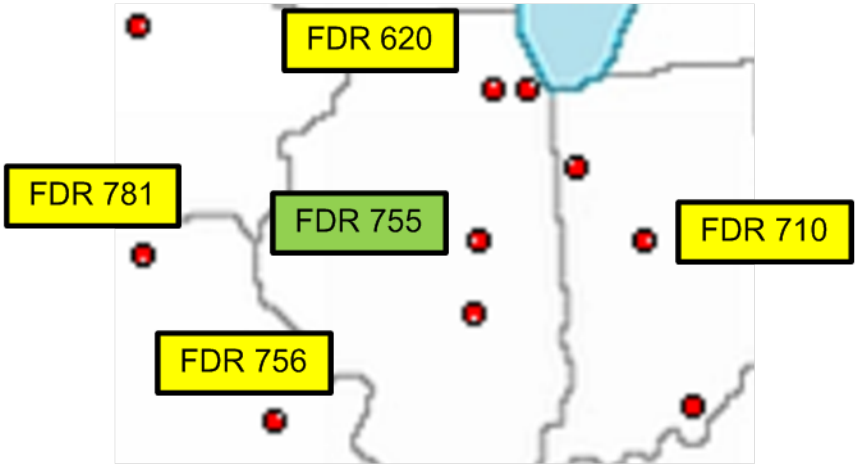

Figure 5-11 FDR Deployment of Michigan Area

In this particular validation case, one generation trip (as shown by Figure 5-12) detected by FNET system on UTC 21:42:37, Jan. 1, 2012 is used to train the model, and then a load shedding event that occurred 23 minutes later (as shown by Figure 5-13) is utilized to test the accuracy of the identified model. Because FNET can only provide the accurate frequency and voltage angle measurement, only frequency and angle estimation are considered in this test. The comparison between estimated frequency/angle response and the real measurement data (provided by FDR 755) are given in Figure 5-14 and Figure 5-15, respectively. Apparently, both the estimated frequency and angle responses match the real measurements well.

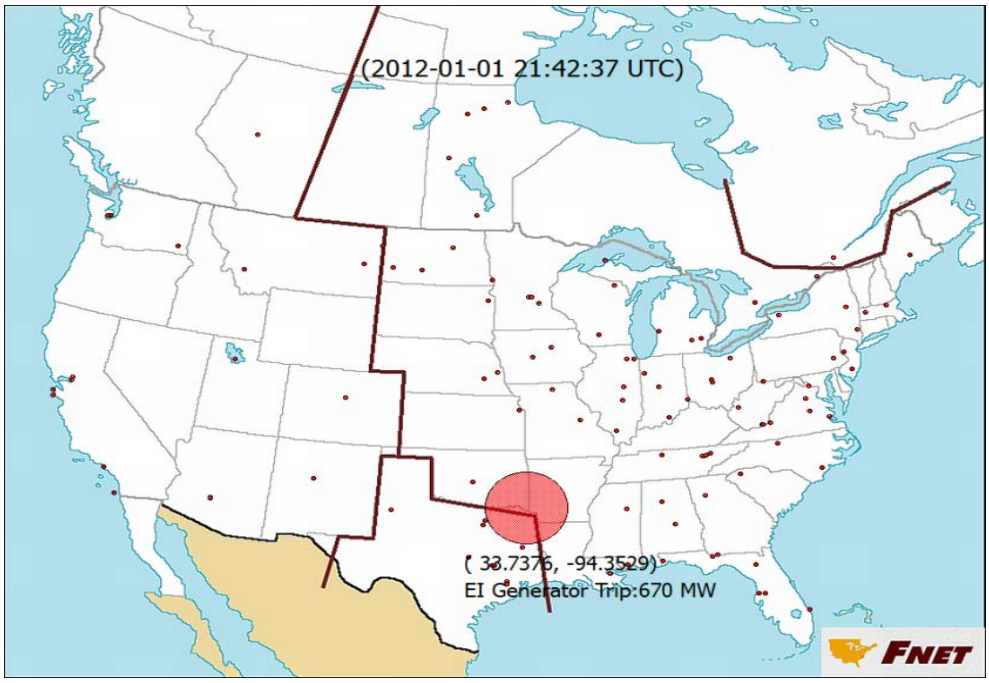

Figure 5-12 A Generation Trip Event Detected by FNET

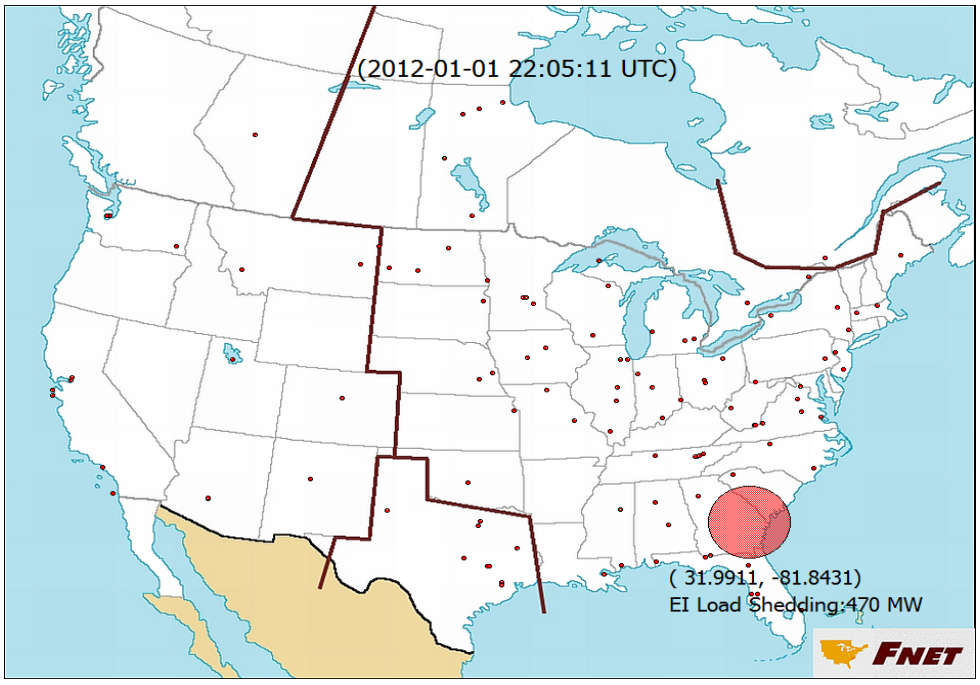

Figure 5-13 A Load Shedding Event Detected by FNET

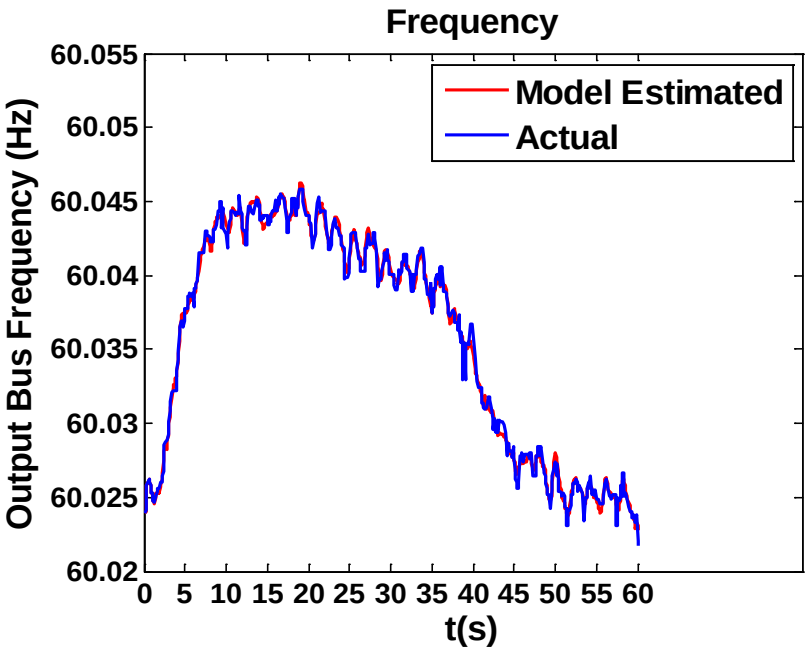

Figure 5-14 Comparison between Estimated Frequency Response and Actual Frequency Measurement

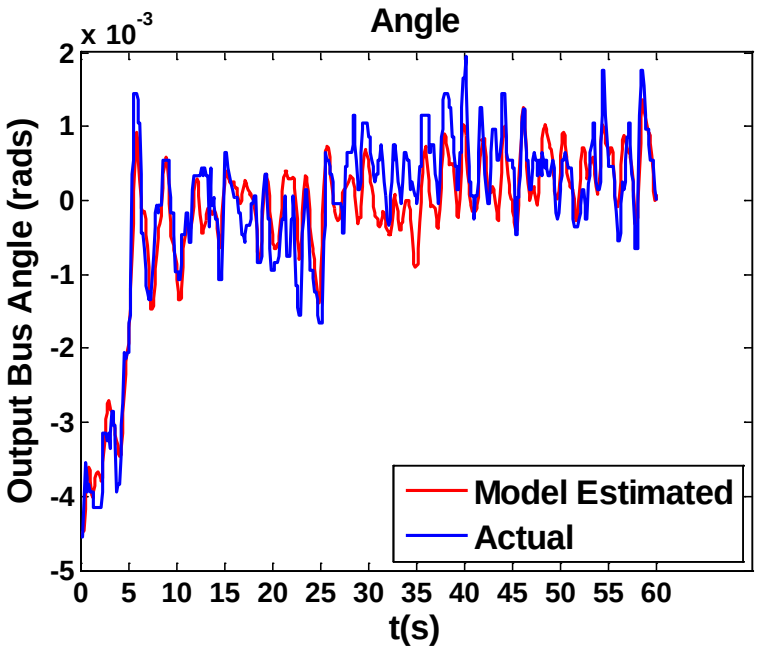

Figure 5-15 Comparison between Estimated Angle Response and Actual Angle Measurement

5.6 Potential Applications in the Early Warning of System Instability

Voltage collapse and out of step instability are two major power system stability issues. The potential of the proposed measurement-based dynamic model in the early warning of the two stability issues after cascading outages will be investigated in this section and case study results will be presented. The basic procedure for testing the proposed method in the early warning of voltage collapse and angular instability is given below:

- First, a voltage collapse or angular instability scenario following a sequence of disturbances will be designed and simulated on the 16,000-bus EI system using PSS/E®.
- Then, a model in the proposed ARX model structure will be identified using a period of system response data following the first disturbance.
- After obtaining that model, the system responses following the rest of the disturbance sequence will be applied to the model to perform the response estimations.

5.6.1 Angular Instability

As discussed above, case studies will be used to investigate the potential of the proposed model in predicting angular instability. The first step of this case study is to carefully design a sequence of disturbances, either trips of lines or generators, around the interface between two control areas without causing out of step until the last disturbance. Because the power grid of Florida area is relatively independent of the rest of the EI system, it can be considered as a separate control area with the rest of the EI (as shown in Figure 5-16). Therefore, a sequence of disturbances, including both generation and line trips, between those two control areas (in the purple rectangle in Figure 5-16) is designed and whether the identified model and estimation accuracy can indicate the out of step of Florida area power grid from the rest of the EI system correctly is investigated.

Figure 5-16 Model Input and Output Locations for Out of Step Case Study

The system responses of input and output buses after the sequence of line or generation trips are shown in Figure 5-17. It can be seen that the Florida area power grid kept synchronized with the other part of the EI until the 5-th disturbance, after which the Florida area power grid is out of step with the rest of the EI.

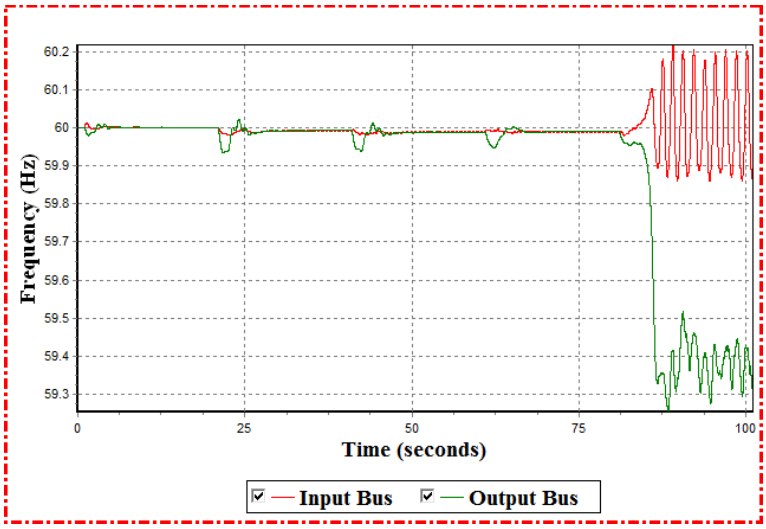

Figure 5-17 Frequency Response of the Input and Output Buses following the Sequence of Disturbances

After obtaining the simulation results, the system response (frequency in this case study) following the first disturbance is used to obtain the model and then the frequency responses following the 2-nd to 5-th disturbances are applied to the model to perform the frequency response estimations. The response estimation results are shown in Figure G-1 in Appendix G and how the accuracy index change is given in Figure 5-18. From Figure 5-18, it's clear that the estimation accuracy decreases gradually after the sequence of the disturbances. After the 4-th disturbance, the accuracy index already becomes negative, which implies the Florida area is going to lose synchronism with the rest of the EI.

Besides that fixed model used for dynamic frequency estimation, an adaptive model is also considered in the test. Unlike the previous fixed model, the adaptive model is trained using the response data following each disturbance in the sequence, and is used to estimate the frequency response after the next disturbance. The estimation results are given in Figure G-2 in Appendix G and how the accuracy index change in this case is given in Figure 5-19. From Figure 5-19, the adaptive model case also shows a change in

the sign of the accuracy index after the 4-th disturbance, indicating the loss of stability after the 5-th disturbance.

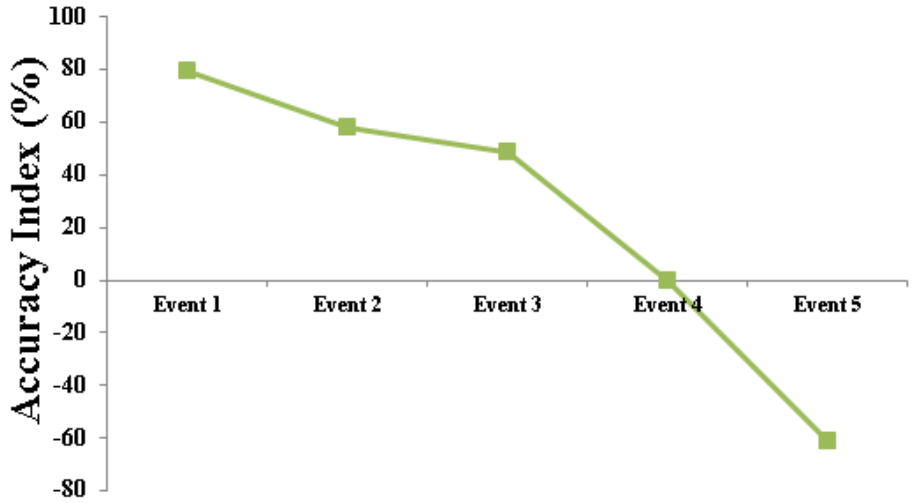

Figure 5-18 Accuracy Index Change of Frequency Estimation Following the Sequence of Disturbances-Fixed Model

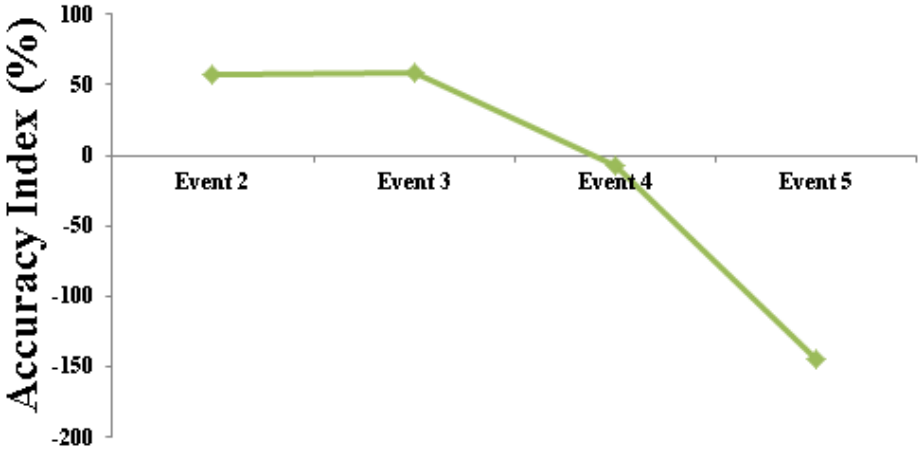

Figure 5-19 Accuracy Index Change of Frequency Estimation Following the Sequence of Disturbances-Adaptive Model

5.6.2 Voltage Collapse

In this voltage collapse case study, the power grid of Massachusetts area (indicated in Figure 5-20) is chose as the test system since it is a load center vulnerable to voltage instability. A sequence of trips of lines or generators around the boundary of the Massachusetts power grid is added to the boundary of that load center area to gradually reduce remote power supplies until an operating condition (at about 60s) very close to voltage instability and then a very slight 1% load increase is made in the area to trigger the voltage collapse at about 80s, as shown in Figure 5-21.

Figure 5-20 Model Inputs and Output Locations for Voltage Collaspe Case Study

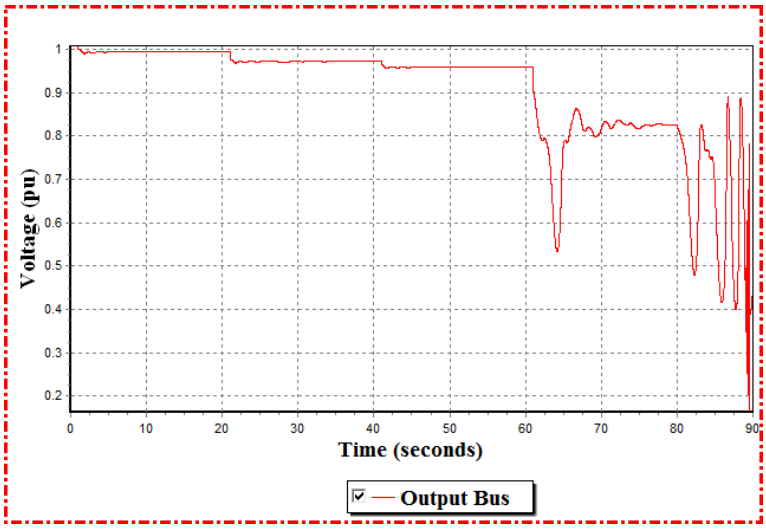

Figure 5-21 Voltage Response of the Output Bus Following the Sequence of Disturbances

Similar to the previous case study, the system response (voltage in this case) following the first disturbance is used to obtain the model and then the voltage responses following the 1-st~4-th disturbances are applied to the model to perform the voltage response estimations. The voltage response estimation results are shown in Figure H-1 in Appendix H and how the accuracy index change is shown in Figure 5-22. Figure 5-22 illustrates clearly that the accuracy of voltage estimation decreases continuously following the sequence of disturbances. That may imply the trend toward voltage collapse and the low accuracy following the 4-th disturbance indicates the possible voltage collapse following the next disturbance. Similar to the angular stability case, the results of an adaptive model strategy are given in Figure H-2 in Appendix H, and the corresponding accuracy index is given in Figure 5-23, which indicate higher estimation accuracies of the model before the system loses stability but suggests the same trend.

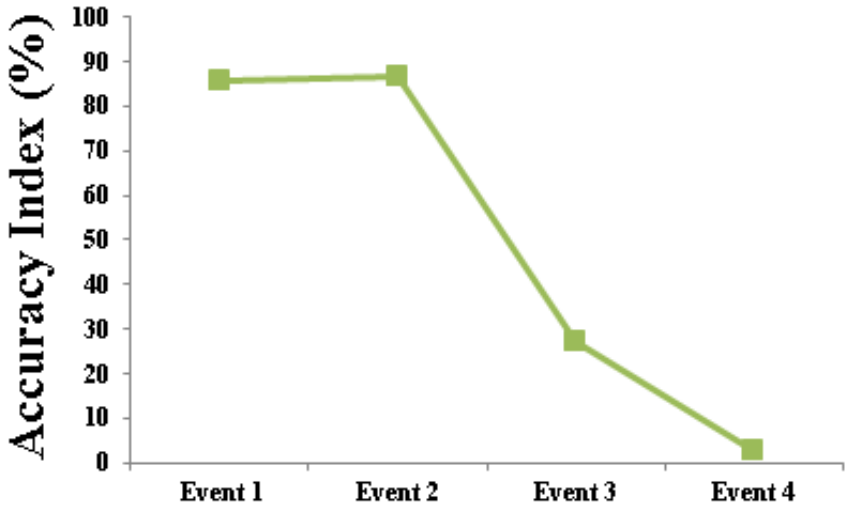

Figure 5-22 Accuracy Index Change of Voltage Estimation Following the Sequence of Disturbances-Fixed Model

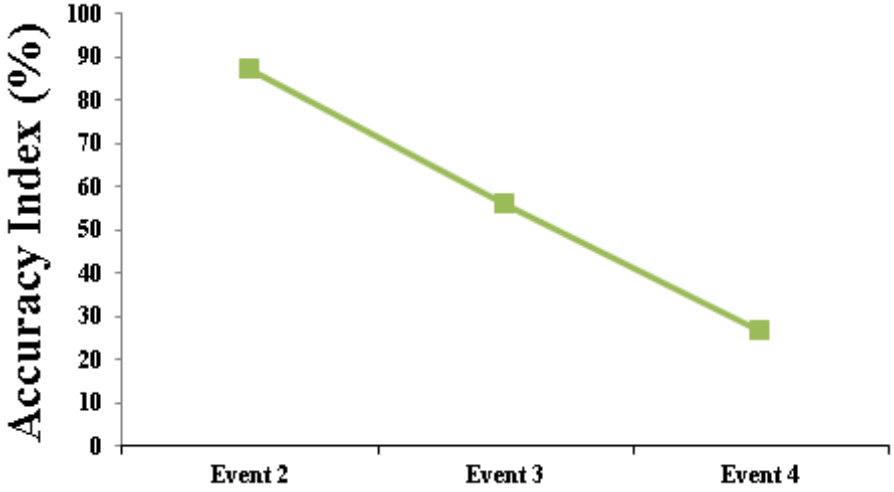

Figure 5-23 Voltage Response Change of Voltage Estimation Following the Sequence of Disturbances-Adaptive Model

5.7 Conclusions

This chapter focused on a measurement-based power system dynamic modeling method for power system response estimation and instability warning. The basic idea is to dynamically identify a reduced equivalent model for the power system and use that model to estimate the power system's dynamic response of interest. ARX model structure and least-squares techniques were employed to identify the parameters of that model for response estimation. For a large-scale power grid, the identification of the proposed model is computationally efficient and suitable for online applications.

Case studies were conducted to test the proposed model's observability, accuracy and reliability with different excitation sources, different numbers and locations of model inputs, and cascading events leading to out-of-step or voltage collapse. The results indicate that the proposed approach seems to be effective in estimating power system dynamic response from limited synchrophasor measurements and seems to be promising in the early warning of instability for out-of-step and voltage collapse caused by cascading outages.

Chapter 6 CONCLUSIONS AND FUTURE WORKS

6.1 Conclusions

This dissertation covered a wide variety of research topics around synchrophasor and its applications, including synchrophasors' calibration, dynamic performance test and timing techniques, as well as the applications in wide-area control of renewable energy sources and measurement-based dynamic model construction.

At the very beginning, this dissertation introduced the basic procedure for the FDRs' calibration and a preliminary test of their dynamic performance. Moreover, this dissertation also investigated the impact of GPS signal availability on FDRs' measurement accuracy and suggested both high-sensitivity GPS receiver and non-GPS based timing techniques, such as eLoran® technology, as a backup for current synchrophasor timing.

Secondly, the wide-area control of renewable energy sources (including both variable-speed wind generators and PV generators) for frequency regulation and inter-area oscillation damping was discussed in this dissertation as an example of synchrophasor applications. Specifically, based on the user-defined wind/PV electrical control model developed in this dissertation and the 16,000-bus Eastern Interconnection (EI) dynamic model, various controllers for frequency regulation and inter-area oscillation damping were developed and the potential contributions of renewable energy sources to the EI system frequency regulation and inter-area oscillation damping were evaluated. Simulation results demonstrate that even at a relatively low penetration level (5% in this dissertation's simulation) renewable energy resources have already been able to contribute significantly.

After that, this dissertation proposed a measurement-based power system dynamic modeling method, which is another important application of synchrophasor measurement. In this work, based on a linear ARX model structure, a concept of dynamic response estimation was proposed and its overall performance was examined by a series of tests.

Case studies also demonstrate that this measurement-based model can help with identifying angular and voltage stability issues.

6.2 Future Works

This dissertation explored some research territories around synchrophasor and its applications. Though very promising results have been presented in this dissertation, there is still a lot of interesting future work that can be done.

For the FDR dynamic test part, the new synchrophasor standards (IEEE C37.118.1-2011) released in 2011 gives very detailed specifications for synchrophasor dynamic performance. Therefore, new dynamic tests should be planned and performed in order to make sure FDRs meet the new standard.

As for the wide-area control of renewable energy sources part, better coordinated control strategies are necessary to be developed and a practical way of tuning controller parameters also needs to be proposed. Furthermore, how to consider the frequency regulation and oscillation damping together and how to create the simulation scenarios with higher renewable penetration are also highly desirable.

For the dynamic model construction part, more theoretical analysis needs to be done for quantifying the bulk power system linearity and analyzing the parameters that may contribute to system linearity. The future applications in power system control and small-signal stability of this proposed method also enjoys great potentials.

LIST OF REFERENCES

[1] B. Qiu, L. Chen, V. Centeno, X. Dong, and Y. Liu, "Internet-based Frequency Monitoring Network (FNET) ", in *IEEE Power Engineering Society Winter Meeting*, pp. 1166-1171, 2001.

[2] Z. Zhong, C. Xu, B. J. Billian, L. Zhang, S. S. Tsai, R. W. Conners, V.A. Centeno, A. G. Phadke, and Y. Liu, "Power System Frequency Monitoring Network (FNET) Implementation", *IEEE Transactions on Power Systems*, vol. 20, pp. 1914-1921, 2005.

[3] L. Wang, J. Burgett, J. Zuo, C. Xu, B.J. Billian, R.W. Conners, and Y. Liu, "Frequency Disturbance Recorder Design and Developments", in *IEEE Power Engineering Society General Meeting*, pp.1-7, 2007.

[4] IEEE Standard for Synchrophasors for Power Systems, IEEE Std C37.118.2005, Mar. 2006.

[5] B. Vandiver, A. Apostolov, and F. Steinhauser, "Testing of Phasor Measurement Units", in *Proc. the 63rd Annual Conference for Protective Relay Engineers*, pp. 1-5, 2010.

[6] G. Stenbakken and Ming Zhou, "Dynamic Phasor Measurement Unit Test System", in *Proc. 2007 IEEE Power Engineering Society General Meeting*, pp. 1-8, 2007.

[7] Y. Liu, Y. Jia, Z. Lin, Y. Liu, Y. Zhang, and L. Wang, "Impact of GPS Signal Quality on the Performance of Phasor Measurements", in *North American Power Symposium (NAPS)*, pp.1-7, 2011.

[8] Motorola, "M12 Oncore User's Guide Supplement", 2000, http://www.deetc.isel.ipl.pt/sistemastele/ST1/arquivo/M12%20_Supplement.pdf.

[9] Y. Zhang, P. Markham, T. Xia, L. Chen, Y. Ye, Z. Wu, Z. Yuan, Wang, J. Bank, J. Burgett, R. W. Conners, and Y. Liu, "Wide-area Frequency Monitoring Network (FNET) Architecture and Applications", *IEEE Transaction on Smart Grid*, 1(2): 159-167, 2010.

[10] Navsync, "CW12 Software User's Guide", 2010, http://www.navsync.com/docs/cw12-tim_um.pdf.

[11] S. Basker, P. Williams, M. Bransby, J. D. Last, G. Offermans, and A. Helwig, "Enhanced Loran: Real-time Maritime Trials", in *2008 IEEE/ION Position Location and Navigation Symposium*, pp.792-799, 2008.

[12] A. Abrantes, "Overview of Power Quality Aspects in Wind Generation", in *North American Power Symposium (NAPS)*, pp. 1-6, 2012.

[13] K. Shanthini, and N. Verappan, "Power Quality Enhancement of Wind Generators Connected to Grid", in *International Conference on Emerging Trends in Electrical Engineering and Energy Management (ICETEEEM)*, pp. 398-403, 2012.

[14] E. Muljadi, C. P. Butterfield, J. Chacon, and H. Romanowitz, "Power Quality Aspects in a Wind Power Plant", in *IEEE Power Engineering Society General Meeting*, 2006.

[15] A. Mullane, G. Lightbody, and R. Yacamini, "Wind-turbine Fault Ride-through Enhancement", *IEEE Transactions on Power Systems*, 20(4): 1929-1937, 2005.

[16] A. Causebrook, D. J. Atkinson, and A. G. Jack, "Fault Ride-Through of Large Wind Farms Using Series Dynamic Braking Resistors", *IEEE Transactions on Power Systems* 22(3): 966-975, 2007.

[17] N. W. Miller, M. Shao, S. Venkataraman, C. Loutan, and M. Rothleder, "Frequency Response of California and WECC under High Wind and Solar Conditions", in *IEEE Power and Energy Society General Meeting*, pp: 1-8, 2012.

[18] L. Ruttledge, N.W. Miller, J. O'Sullivan, and D. Flynn, "Frequency Response of Power Systems with Variable-Speed Wind Turbines", *IEEE Transactions on Sustainable Energy*, 3(4): 683-691, 2012.

[19] J. Haan, J. Frunt, and W.L. Kling, "Grid Frequency Response of Different Sized Wind Turbines", in *Universities' Power Engineering Conference (UPEC)*, pp: 1-6, 2011.

[20] P. Mackin, R. Daschmans, B. Williams, B. Haney, R. Hunt, J. Ellis, and J.H. Eto, "Dynamic Simulation Study of the Frequency Response of the Western Interconnection with Increased Wind Generation", In *International Conference on System Sciences (HICSS)*, pp: 2222-2229, 2013.

[21] J. Villena-Lapaz, A. Vigueras-Rodriguez, E. Gomez-Lazaro, A. Molina-Garcia, and J. A. Fuentes-Moreno, "Evaluation of Frequency Response of Variable Speed Wind Farms for Reducing Stability Problems in Weak Grids", in *Power Electronics and Machines in Wind Applications* (PEMWA), pp:1-5, 2011.

[22] J. G. Slootweg, and W. L. Kling, "The Impact of Large Scale Wind Power Generation on Power System Oscillations", *Electric Power Systems Research*, 67(1): 9-20, 2003.

[23] D. Thakur, and N. Mithulananthan, "Influence of Constant Speed Wind Turbine Generator on Power System Oscillation", *Electric Power Components and Systems*, 37: 478-494, 2009.

[24] N. Modi, T. K. Saha, and N. Mithulananthan, "Effect of Wind Farms with Doubly-fed Induction Generators on Small-signal Stability—A Case Study on Australian Equivalent System", in *IEEE PES Innovative Smart Grid Technologies Asia (ISGT)*, pp: 1-7, 2011.

[25] D. J. Vowles, C. Samarasinghe, M. J. Gibbard, and G. Ancell, "Effect of Wind Generation on Small-signal Stability: a New Zealand Example", in *IEEE Power Energy Society General Meeting*, pp: 1-8, 2008.

[26] N. A. Janssens, G. Lambin, and N. Bragard, "Active Power Control Strategies of DFIG Wind Turbines*", 2007 IEEE Lausanne Power Tech*, pp: 516-521, 2007.

[27] J. M. Mauricio, A. Marano, A. Gomez-Exposito, and J. L. Martinez Ramos, "Frequency Regulation Contribution through Variable-speed Wind Energy Conversion Systems", *IEEE Transactions on Power Systems*, 24(1): 173-180, 2009.

[28] J. F. Conroy, and R. Watson, "Frequency Response Capability of Full Converter Wind Turbine Generators in Comparison to Conventional Generation", *IEEE Transactions on Power Systems*, 23(2): 649-656.

[29] G. Ramtharan, J. B. Ekanayake, and N. Jenkins, "Frequency Support from Doubly-fed Induction Generator Wind Turbines", *IET Renewable Power Generation*, 1(1): 3-9, 2007.

[30] G. Lalor, A. Mullane, and M. O'Malley, "Frequency Control and Wind Turbine Technologies", *IEEE Transactions on Power Systems*, 20(4): 1905-1913, 2012.

[31] R. G. Almeida, E. D. Castronuovo, and J. A. Peas Lopes, "Optimum Generation Control in Wind Parks when carrying out System Operator Requests", *IEEE Transactions on Power Systems*, 21(2): 718-725, 2006.

[32] R. G. Almeida, and J. A. Peas Lopes, "Participation of Doubly-fed Induction Wind Generators in System Frequency Regulation", in *IEEE Transactions on Power Systems*, 22(3): 944-950, 2007.

[33] Y. Sun, Z. Zhang, G. Li, and J. Lin, "Review on Frequency Control of Power Systems with Wind Power Penetration", in *International Conference on Power System Technology (POWERCON)*, pp:1-8, 2010.

[34] WindINERTIA Control Fact Sheet, GE Energy, 2009. (http://site.geenery.com/prod_serv/products/renewable_energy/en/downloads/GEA17210.pdf)

[35] G. Tsourakis, B. M. Nomikos, and C. D. Vournas, "Contribution of Doubly-fed Wind Generators to Oscillation Damping", *IEEE Transactions on Energy Conversion*, 24(3): 783-791.

[36] P. Ledesma, and C. Gallardo, "Contribution of Variable-speed Wind Farms to Damping of Power system Oscillations", *Power Tech*, pp: 190-194, 2007.

[37] M. Zhixin, F. Lingling, D. Osborn, and S. Yuvarajan, "Control of DFIG-based Wind Generation to Improve Inter-area Oscillation Damping", In *Power and Energy Society General Meeting-Conversion and Delivery of Electrical Energy in the 21st Century*, pp: 1-7, 2008.

[38] X. Liu, D. McSwiggan, T. B. Littler, and J. Kennedy, "Measurement-based Method for Wind Farm Power System Oscillations Monitoring", *IET Renewable Power Generation*, 4(2): 198-209.

[39] F. Lingling, Y. Haiping, and M. Zhixin, "On active/reactive Power Modulation of DFIG-based Wind Generation for Inter-area Oscillation Damping", *IEEE Transactions on Energy Conversion*, 26(2): 513-521.

[40] T. Knuppel, J. N. Nielsen, K. H. Jensen, A. Dixon, and J. Ostergaard, "Power Oscillation Damping Capabilities of Wind Power Plant with Full Converter Wind Turbines considering its Distributed and Modular Characteristics", in *IET Conference on Renewable Power Generation*, pp: 1-6, 2011.

[41] T. Knuppel, J. N. Nielsen, K. H. Jensen, A. Dixon, and J. Otergaard, "Power Oscillation Damping Controller for Wind Power Plant Utilizing Wind Turbine Inertia as Energy Storage", in *Power and Energy Society General Meeting*, pp: 1-8, 2011.

[42] G. Tsourakis, B. M. Nomikos, and C. D. Vournas, "Contribution of Doubly-fed Wind Generators to Oscillation Damping", *IEEE Transactions on Energy Conversion*, 24(3): 783-791.

[43] PSSE Version 32 User Manual, 2012.

[44] Y. Zhiyong, X. Tao, Z. Yingchen, C. Lang, P. Markham, R. M. Gardner, and L. Yilu, "Inter-area Oscillation Analysis Using Wide-area Voltage Angle Measurements from FNET", in *Power and Energy Society General Meeting*, pp: 1-7, 2010.

[45] M. E. Aboul-Ela, A. A. Sallam, J. D. McCalley, and A. A. Fouad, "Damping Controller Design for Power System Oscillations using Global Signals", *IEEE Transactions on Power Systems*, 11(2): 767-773.

[46] I. Kamwa, R. Grondin, and Y. Hebert, "Wide-area Measurement based Stabilizing Control of Large Power Systems-a Decentralized/hierarchical Approach", *IEEE Transactions on Power Systems*, 16(1):136-153.

[47] S. W. De Haan, H. Oldenkamp, and E. J. Wildenbeest, "Test Results of a 130 W AC Module; a Modular Solar AC power Station", in *Conference Record of the Twenty Fourth IEEE Photovoltaic Specialists Conference*, pp: 925-928, 1994.

[48] R.H. Wills, F.E. Hall, S.J. Strong, and J.H. Wohlgemuth, "The AC Photovoltaic Module", in *Conference Record of the Twenty Fifth IEEE Photovoltaic Specialists Conference*, pp: 1231-1234, 1996.

[49] S. Yatsuki, K. Wada, T. Shimizu, H. Takagi, and M. Ito, "A Novel AC Photovoltaic Module System Based on the Impedance-admittance Conversion Theory", in *IEEE 32nd Annual Power Electronics Specialists Conference*, pp: 2191-2196, 2001.

[50] C. Prapanavarat, M. Barnes, and N. Jenkins, "Investigation of the Performance of a Photovoltaic AC Module", *IEE Proceedings-Generation, Transmission and Distribution*, 149(4): 472-478, 2002.

[51] J.J. Bzura, "The AC Module: An Overview and Update on Self-contained Modular PV Systems", in *IEEE Power and Energy Society General Meeting*, pp: 1-3, 2010.

[52] List of photovoltaic power stations, http://en.wikipedia.org/wiki/List_of_photovoltaic_power_stations

[53] M. I. Hossain, S. A. Khan, M. Shafiullah, and M. J. Hossain, "Design and Implementation of MPPT Controlled Grid Connected Photovoltaic System", in *2011 IEEE Symposium on Computers & Informatics (ISCI)*, pp: 284-289, 2011.

[54] H. P. Desai, and H. K. Patel, "Maximum Power Point Algorithm in PV Generation: An Overview", in *7th International Conference on Power Electronics and Drive Systems*, pp: 624-630, 2007.

[55] M. Veerachary, T. Senjyu, and K. Uezato, "Neural-network-based Maximum-power-point tracking of Coupled-inductor Interleaved-boost-converter-supplied PV System using Fuzzy Controller", *IEEE Transactions on Industrial Electronics*, 50(4): 749-758, 2003.

[56] T. Esram, and P.L. Chapman, "Comparison of Photovoltaic Array Maximum Power Point Tracking Techniques", *IEEE Transactions on Energy Conversion*, 22(2): 439-449, 2007.

[57] W. Xiao, N. Ozog, and W. G. Dunford, "Topology Study of Photovoltaic Interface for Maximum Power Point Tracking", *IEEE Transactions on Industrial Electronics*, 54(3): 1696-1704, 2007.

[58] P. Kundur, Power System Stability and Control, New York: McGraw-Hill, Inc., 1994.

[59] D. N. Kosterev, C. W. Taylor, and W. A. Mittelstadt, "Model Validation for the August 10, 1996 WSCC System Outage", *IEEE Transaction on Power Systems*, 14(3): 967-979, 1999.

[60] Monitoring and Estimation of Power System Dynamic Response Using Synchrophasors: Measurement-based Power System Dynamic Modeling. EPRI, Palo Alto, CA: 2012. 1026456.

[61] Y. Liu, K. Sun, and Y. Liu, "Measurement-based Power System Dynamic Model for Response Estimation", in *IEEE PES General Meeting*, pp: 1-6, 2012.

[62] Lennart Ljung, System Identification: Theory for the User (2nd Edition), New Jersey: PTR Prentice, 1999.

[63] Gharban C K, Cory B J, “Non-Linear Dynamic Power System State Estimation,” *IEEE Transactions on Power Systems*, 1(3):276-283, 1986.

APPENDIX

APPENDIX A TECHNICAL SPECIFICATIONS OF FREQUENCY DISTURBANCE RECORDER

Table A-1 Technical Specifications of FDR

Voltage range	90V to 140V with power supply 120 V. (a 50 Hz, 240V version is also available for installation in Europe, Asia, and Africa)
Sampling rate	Voltage input is sampled at 1,440 Hz
GPS	GPS synchronized data collection using UTC time
Output data rate	1.2 kB/second
Measurement accuracy	Frequency: ±0.0005Hz; Angle: 0.003 rad; Voltage: 0.2V
Other specifications	Outputs: frequency, absolute phase angle, UTC time, location, and voltage magnitude at 10 data messages per second
	Continuous data transmission with local LCD display
	Ethernet-enabled; data are transmitted via the Internet to the FNET servers

APPENDIX B USER-DEFINED WIND ELECTRICAL CONTROL MODEL (ACTIVE POWER PART)

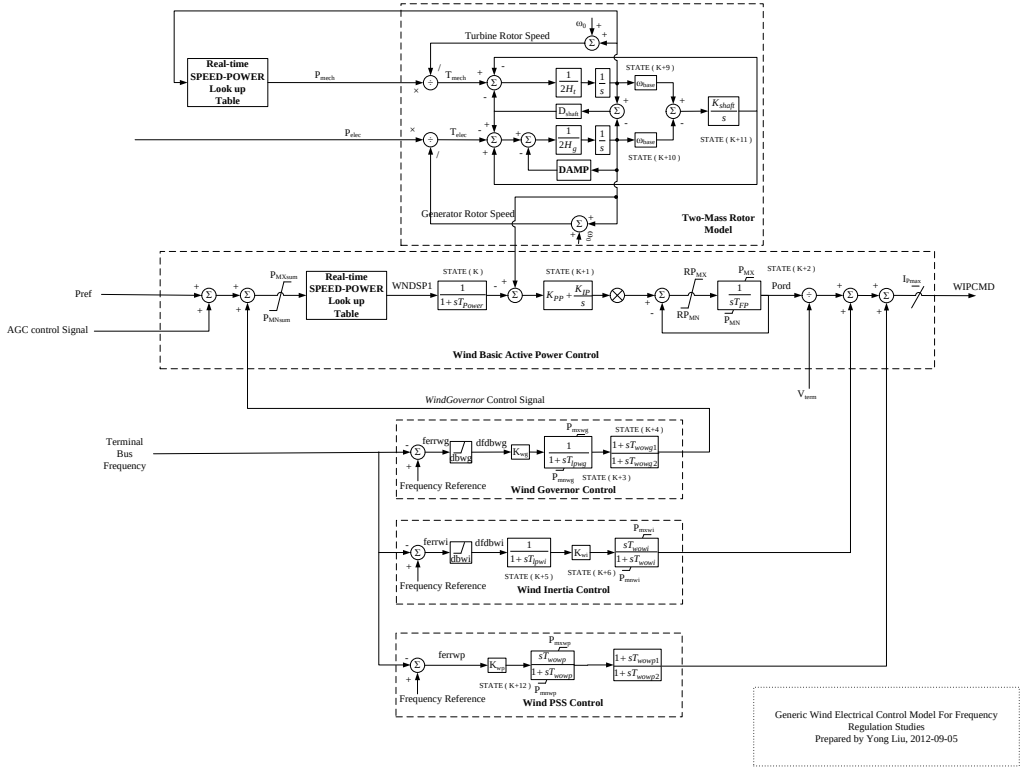

Figure B-1 User-defined WT3 Electrical Control Model (Active Power Part)

Table B-1 Parameters of User-defined Wind WT3 Electrical Control Model (Basic Power Control Part)

Constant No.	Constant Name
CON(J)	T_{Power}, Power filter time constant
CON(J+1)	K_{PP}, Proportional gain in torque regulator(pu)
CON(J+2)	K_{IP}, Integrator gain in torque regulator(pu)
CON(J+3)	RP_{MX}, Max power order derivative
CON(J+4)	RP_{MN}, Min power order derivative
CON(J+5)	P_{MX}, Max limit in torque regulator (pu)
CON(J+6)	P_{MN}, Min limit in torque regulator (pu)
CON(J+7)	IP_{MAX}, Max reactive current limit
CON(J+8)	T_{FP}, Filter time constant in torque regulator
CON(J+22)	Q_{MX}, Max limit in voltage regulator (pu)
CON(J+23)	Q_{MN}, Min limit in voltage regulator (pu)
CON(J+24)	V_{MAXCL}, Max voltage limit
CON(J+25)	V_{MINCL}, Min voltage limit
CON(J+26)	K_{qi} , MVAR/Voltage gain
CON(J+27)	XIQ_{max}
CON(J+28)	XIQ_{min}
CON(J+29)	K_{qv}, Voltage/MVAR gain
CON(J+37)	H, total inertia constant, sec
CON(J+38)	H_{tfrac}, turbine inertia fraction(Htur/H)
CON(J+39)	DAMP, machine damping factor, pu P/pu speed
CON(J+40)	D_{shaft}, Shaft damping factor (pu)
CON(J+41)	Freq1, First shaft torsional resonant frequency, Hz

Table B-2 Parameters of Wind Inertia Control Loop

Constant No.	Constant Name
CON(J+9)	db_{wi}, Wind inertia deadband
CON(J+10)	T_{lpwi}, Wind inertia filter time constant
CON(J+11)	K_{wi}, Wind inertia Gain
CON(J+12)	T_{wowi}, Wind inertia washout time constant
CON(J+13)	P_{mxwi}, Wind inertia maximum additional power
CON(J+14)	P_{mnwi}, Wind inertia maximum additional power

Table B-3 Parameters of Wind Governor Control Loop

Constant No.	Constant Name
CON(J+15)	db_{wg}, Wind governor deadband
CON(J+16)	T_{lpwg}, Wind governor filter time constant
CON(J+17)	K_{wg}, Wind governor gain
CON(J+18)	T_{wowg1}, Wind governor washout time constant1
CON(J+19)	T_{wowg2}, Wind governor washout time constant2
CON(J+20)	P_{mxwg}, Wind governor maximum additional power
CON(J+21)	P_{mnwg}, Wind governor minimum additional power

APPENDIX C USER-DEFINED PV ELECTRICAL CONTROL MODEL (ACTIVE POWER PART)

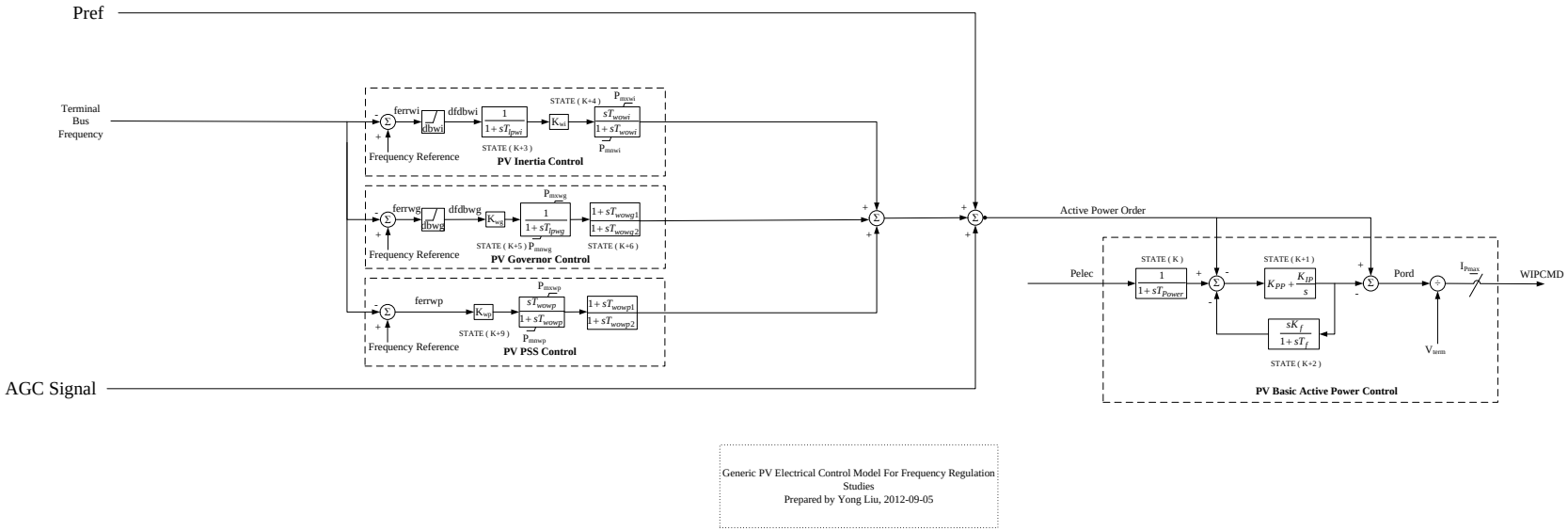

Figure C-1 User-defined PV Electrical Control Model (Active Power Part)

APPENDIX D OBERVERBILITY STUDY FOR POWER SYSTEM DYNAMIC MODELING

In power flow calculations, power transfer distribution factor (PTDF) is the relative change in power flow on a particular line due to a change in injection and corresponding withdrawal at a pair of buses. Therefore, by definition, PTDF is an index to describe the "connectivity" or "sensitivity" between two lines. In this appendix, an observability index can be defined in a similar way to describe the "connectivity" or "electrical distance" between any two points in the power system instead of two lines.

Specifically, the observability index between two points or buses is defined as the absolute value of voltage change at bus i if the current injection at bus k is varied by 1.0 pu. Since this index has the unit of impedance, $|Z\ (i,k)|$ is used to denote it. Actually, $Z\ (i,k)$ is the (i,k) element of the matrix Z_{bus}, which is the inverse of power system admittance matrix Y_{bus}. From the definition, it's apparent that larger observability index means better "connectivity" while smaller observability index indicates less "connectivity."

To verify the effectiveness of this observability index in describing two buses' "connectivity", a test based on the 16,000-bus EI model is carried out. In this test, one output bus and three different groups of input buses are carefully selected from the EI model based on the observability index between them (as shown in Figure D-1 and Table D-1). As for the observability index calculations, the EI system admittance matrix Y_{bus} is exported from PSS/E and the inverse process is completed in Matlab®.

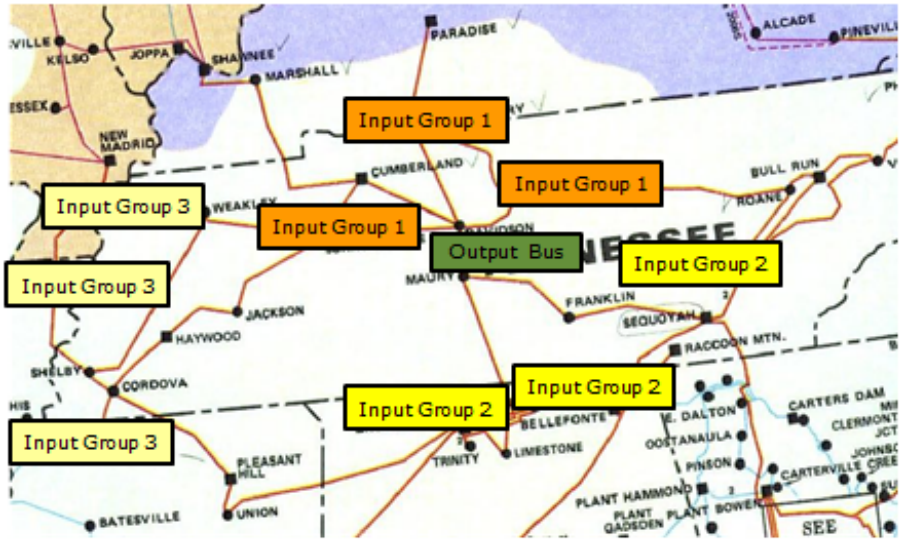

Figure D-1 Model Input and Output Locations for Observability Study

Table D-1 Observability Index between Input and Output Buses

	Z between Input Bus and Output Bus	Observability Index	Average
Group1	0.00039459+0.0045866i	0.0046035	0.0046969
	0.00040728+0.0046761i	0.0046938	
	0.00045713+0.0047715i	0.0047934	
Group2	7.6358e-005+0.00096488i	0.0009679	0.0009666
	0.000107+0.001166i	0.0011709	
	7.7666e-005+0.00075692i	0.0007609	
Group3	2.5415e-005-7.4279e-005i	7.8507e-005	3.0604e-05
	1.0593e-005-6.0988e-006i	1.2223e-005	
	1.1014e-006+1.0021e-005i	1.0081e-005	

The accuracies of the models with different input groups are examined to show the relationship between observability index and model accuracy. Frequency, voltage and angle estimation results are respectively shown in Figure D-2 to Figure D-4. From these results, it's clear that the model accuracy decreases from group 1 to group 3, which means the smaller the observability index, the smaller the accuracy index. Therefore, observability index may serve as an effective index of describing two buses' "connectivity" or "electrical distance" and can be used for the input selection for the proposed model construction method.

	Frequency	Model Accuracy Index
Group 1	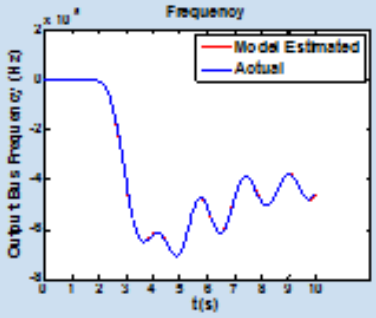	99.3600
Group 2	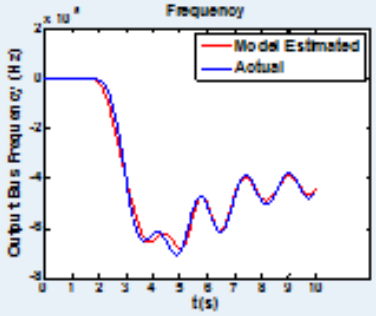	91.0240
Group 3	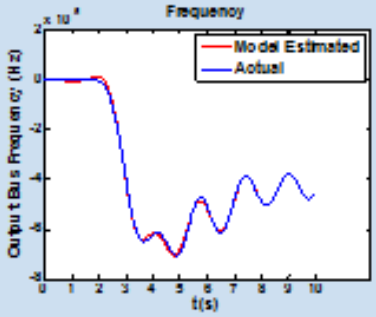	96.9087

Figure D-2 Frequency Response Estimation with Different Levels of Observability Indices

	Voltage	Model Accuracy Index
Group 1	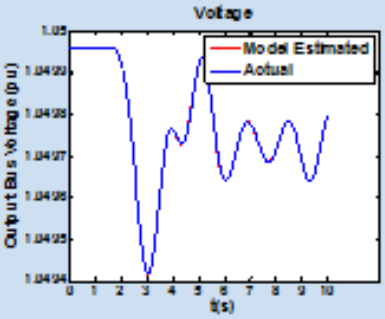	98.9736
Group 2	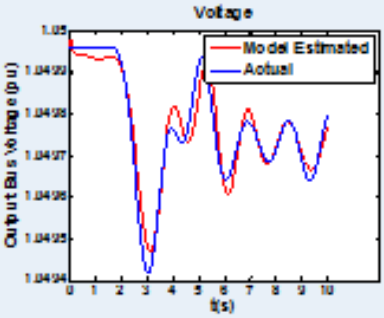	75.1822
Group 3	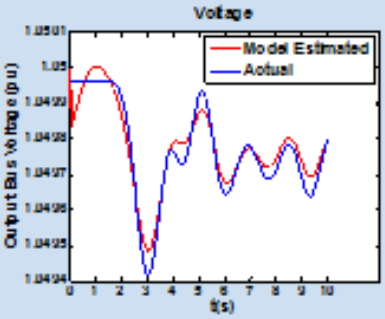	73.4245

Figure D-3 Voltage Response Estimation with Different Levels of Observability Indices

	Angle	Model Accuracy Index
Group 1	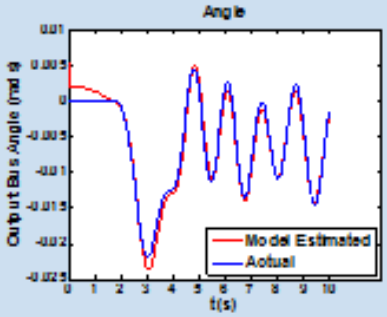	84.8769
Group 2	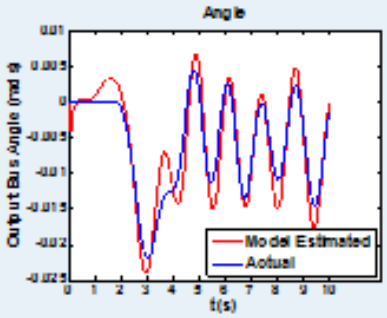	61.4481
Group 3	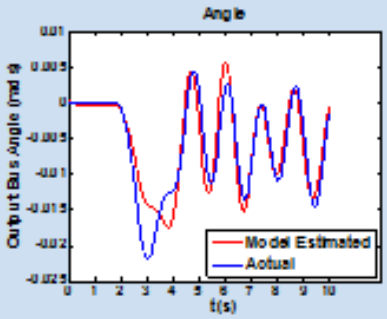	60.1225

Figure D-4 Angle Response Estimation with Different Levels of Observability Indices

The relationships between observability index and model accuracy index for voltage and angle cases are shown in Figure D-5 more clearly. Based on Figure D-5, it is possible to suggest a threshold for the observability index, for example 0.00003 for the EI system in

this particular case. This means the average observability index between the model inputs and output should be larger than 0.00003 in order to make sure that the model accuracy is able to reach 60%. Of course, different accuracy criteria derive different thresholds of the observability index, but here represents a very simple way to derive those thresholds. For frequency, the estimation accuracy is always acceptable (the accuracy index is above 90% in all the three cases).

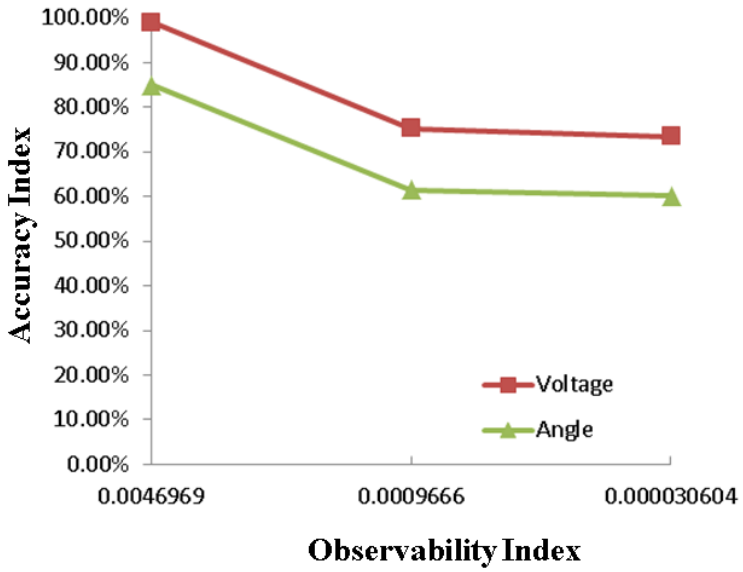

Figure D-5 Relationship between Observability Index and Accuracy Index (Voltage and Angle Cases)

Based on this observability index criterion, a coverage map can be obtained. For example, assume there are three buses with synchrophasor measurements in the Tennessee area that can be considered as the model inputs in the dynamic response estimation. According to the previous criterion, in order to make the response estimation results relatively accurate (60% in this particular case), the average observability index between these three input buses and the output bus should be larger than 0.00003. As a

result, all the possible output buses that meet this criterion can be obtained. It should be noted that the criterion of 0.00003 is only valid for this particular case and any other cases should find its own criterion.

Furthermore, since the observability index has already been defined, the impact of a topology change in the power system on the model accuracy can be studied by looking into the topology change's influence on the observability index between the inputs and output. Intuitionally, nearby events, no matter generation trips, load shedding, or line trips, should pose significant impacts on the observability index since they change the topology to a greater extent. If the observability index between the inputs and output is changed much, the model trained before this topology change will no longer be reliable and thus need to be updated.

A test is carried out to verify that. First, the observability index between bus 48 and 650 is calculated, then a series of line trips are created (one each time) from bus 650 in the radial direction until bus 15508 (as shown by the red arrow in Figure D-6), including line 650-15097, line 15097-15001, line 15001-15502, line 15502-15509, line 15509-15510, line 15510-15875, and line 15875-15508 (all the line numbers are from the 16,000-bus EI model). After each of the line trips, the observability index between bus 48 and 650 is re-calculated until it remains relatively stable. The results are given in Figure D-7.

Figure D-6 Line Trips for Observability Index Study

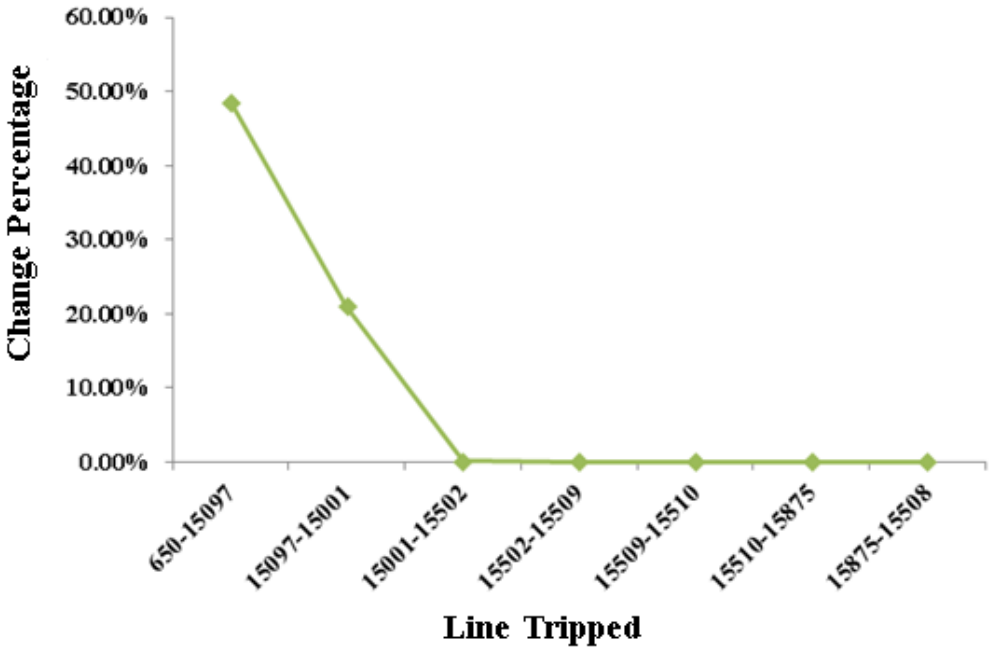

Figure D-7 Observability Index Changes after Line Trips in the Radial Direction

From Figure D-7, after the line 650-15097 tripped, observability index change is around 50% of the original value, which indicates a huge change due to the nearby event. Then after the second line trip 15097-15001, the observability index change is around 20% and after the third line trip 15001-15502, the change could be hardly noticed. Thus, based on this test, it can be concluded that only nearby events influence the observability index. Furthermore, it's interesting that, beyond line 15001-15502, the observability index will not be influenced dramatically by the topology change, which suggests that the line 15001-15502 can be considered as the "boundary" of the topology change's influence. Beyond this boundary, the topology change won't influence the observability index much. Therefore, using the similar method, it's possible to determine the "boundary" of topology change's influence in all the directions. After completing that, it's easy to obtain a rough "boundary map," as shown in Figure D-8. All the topology changes beyond the boundary will not change the observability index significantly, thus not harming the accuracy of the model.

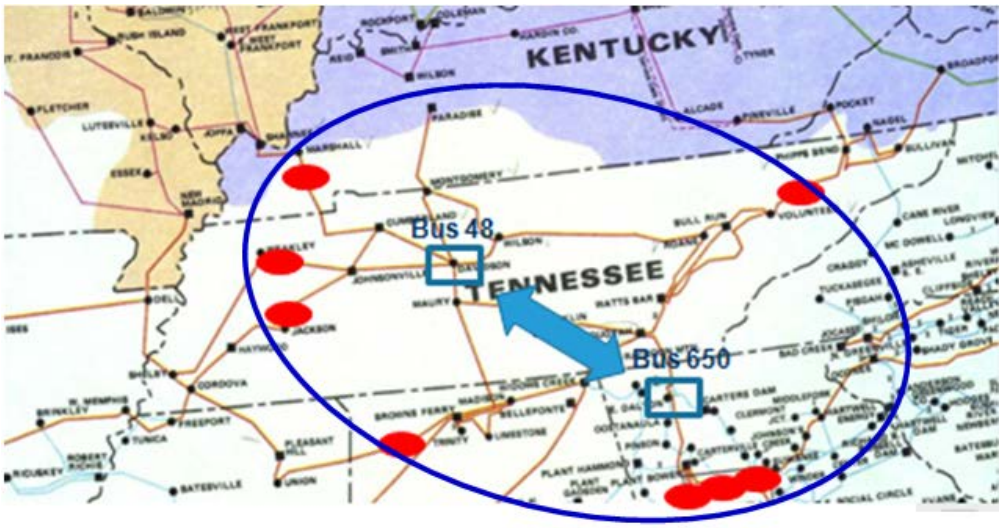

Figure D-8 Boundary Map of Topology Change's Influence

APPENDIX E INFLUENCE OF EXCITATION SOURCE TYPES ON RESPONSE ESTIMATION

Theoretically, all the disturbances in the power system, including generation trip, load shedding, line trip, and fault, can serve as the "excitation sources" of the proposed measurement-based model. However, while the system responses of generation trip and load shedding cases can be monitored in a wide-area sense, the line trip events can only be seen in a relatively small part of the system. Therefore, it is very likely that the models "excited" by different disturbances will have different system coverage extents and accuracy levels. In this appendix, the influence of excitation source types will be studied using simulation case studies. As shown by Table E-1, three different types of disturbances that occur in New York region are used to train the model respectively first and then the trained models are utilized to estimate the system responses following another two types of disturbances that occur in the Florida region.

Table E-1 Different Types of Excitation Sources for Dynamic Response Estimation

Location	Event Type	Amount (MW)
New York	Generation Trip	839
	Load Shedding	809
	Line Trip	790
Florida	Generation Trip	810
	Load Shedding	877

From the test results from Figure E-1 to Figure E-3, the dynamic responses estimated by the trained models match the actual responses well. However, the models using generation trip and load shedding events as the excitation sources have much better accuracies than the model trained by the line trip. This case study does indicate that generation trip and load shedding may serve as better excitation sources for this measurement-based model.

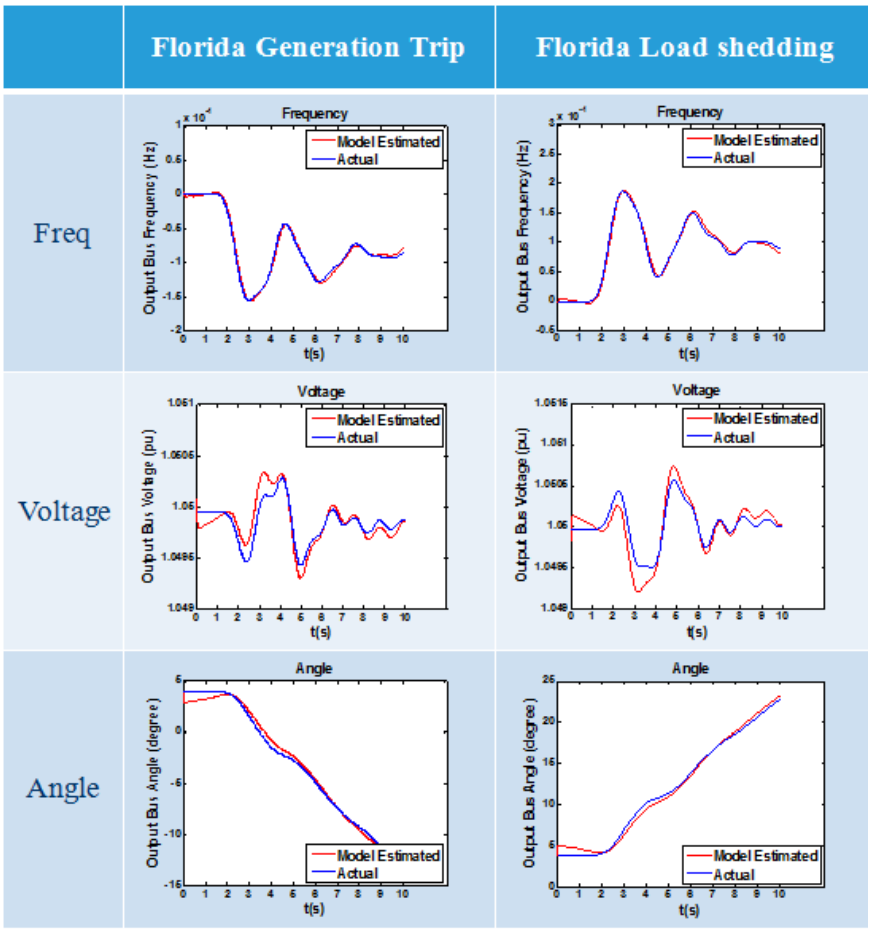

Figure E-1 Dynamic Response Estimation using Generation Trip as Excitation Source

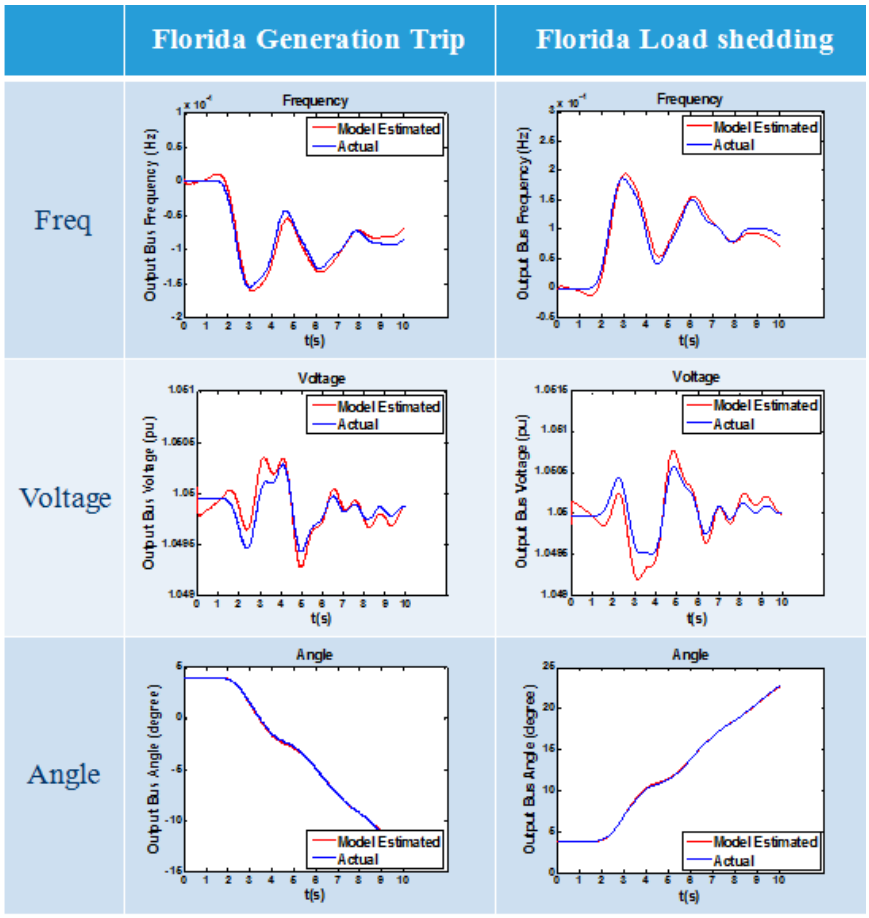

Figure E-2 Dynamic Response Estimation using Load Shedding as Excitation Source

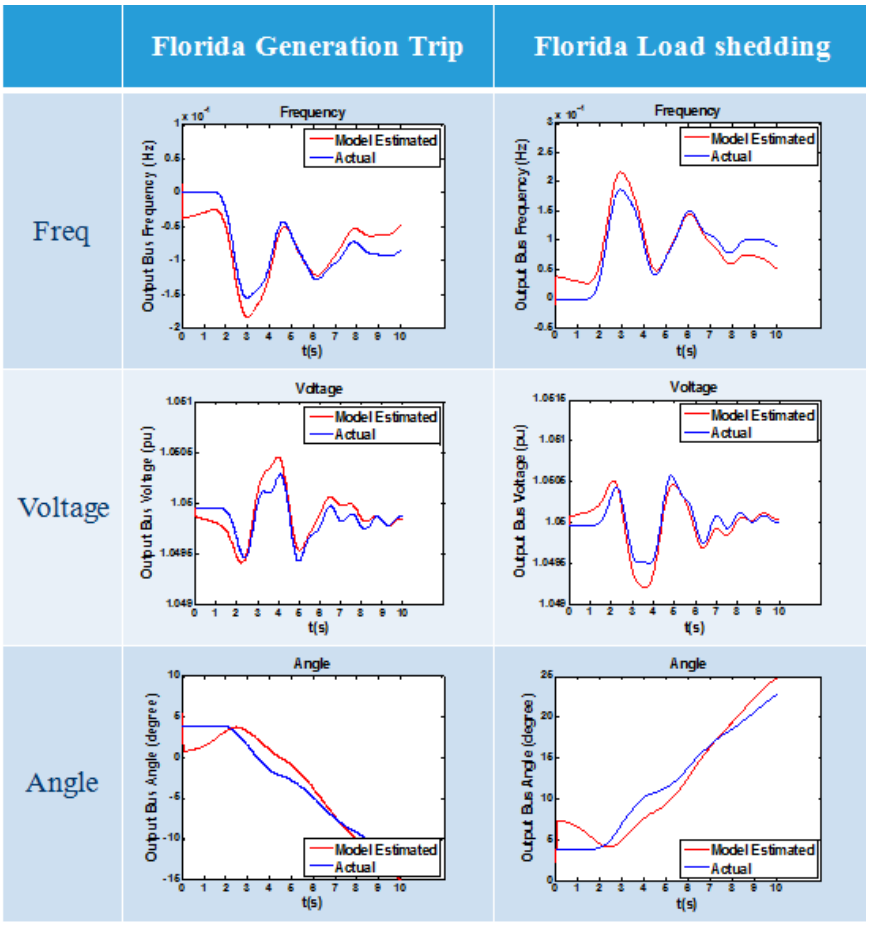

Figure E-3 Dynamic Response Estimation using Line Trip as Excitation Source

APPENDIX F INFLUENCE OF EXCITATION SOURCE LOCATIONS ON RESPONSE ESTIMATION

The locations of the excitation sources may also pose some influence on the accuracy of the proposed model and the response estimation method. However, if the accuracy of the proposed model really relies on the locations of the excitation sources heavily, that will lead to great difficulties for this method because the proposed model is supposed to be updated in near real-time and it's difficult to get the detailed location information of the excitation sources. Therefore, simulation case studies are used to examine whether the locations of the excitation sources pose significant influence on the accuracy of the proposed model.

In this case study, two generation trips that occur in different locations (one in the New York region and the other one in Florida) are used as excitation sources to train the model and another three events that occur in the North Carolina area are estimated (Table F-1). All the frequency, voltage and angle response estimation results are given in Figure F-1 and Figure F-2.

Table F-1 Different Locations of Excitation Sources for Dynamic Response Estimation

Location	Event Type	Amount (MW)
New York	Generation Trip	839
Florida	Generation Trip	810
North Carolina	Generation Trip	410
	Load Shedding	442
	Line Trip	460

	Frequency	Voltage	Angle
North Carolina Generation Trip	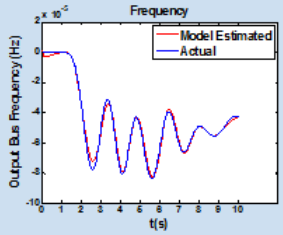	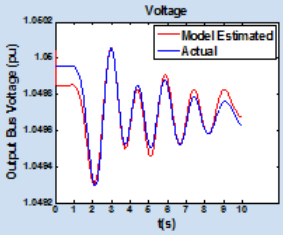	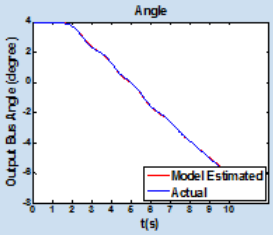
North Carolina Load Shedding	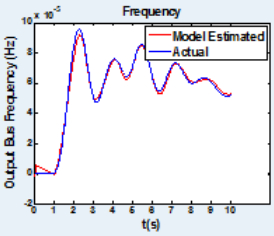	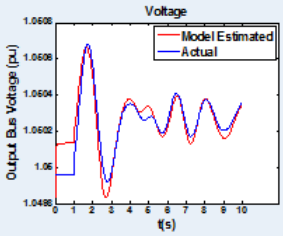	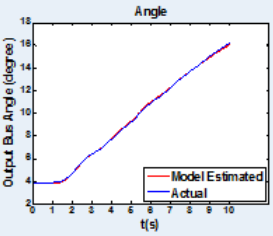
North Carolina Line Trip	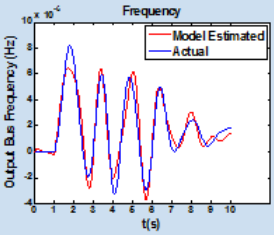	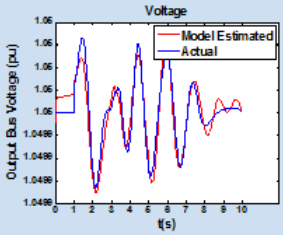	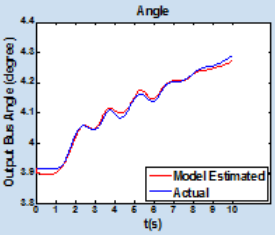

Figure F-1 Dynamic Response Estimation using New York Generation Trip as Excitation Source

Figure F-2 Dynamic Response Estimation using Florida Generation Trip as Excitation Source

From the comparison between Figure F-1 and Figure F-2, it's difficult to tell any noticeable differences between them. Therefore, it seems the excitation source in the New York region is no better or worse than that in Florida. That means the locations of excitations source will not pose significant influences on the accuracy of the model and it's not necessary to obtain the detailed location information of the excitation sources in order to perform the dynamic response estimation.

APPENDIX G APPLICATION IN OUT OF STEP PREDICTION

Event	Response Estimation	Accuracy Index
1	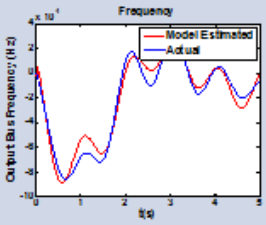	79.6553
2	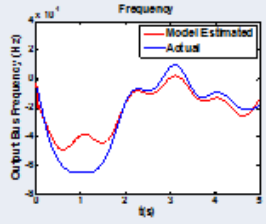	57.6229
3	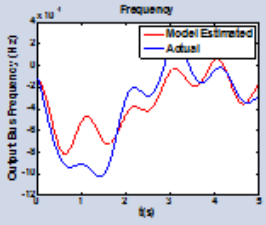	48.3426
4	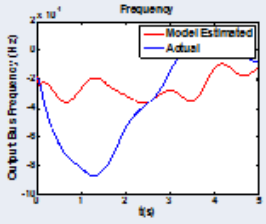	-0.2183
5	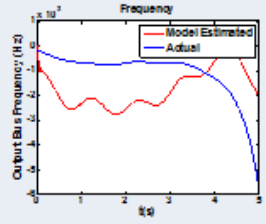	-61.2057

Figure G-1 Frequency Response Estimation Following the Sequence of Disturbances-Fixed Model

Event	Response Estimation	Accuracy Index
1→2	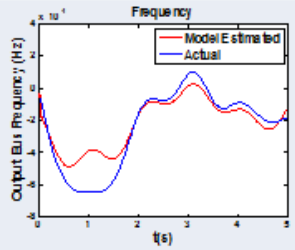	57.6229
2→3	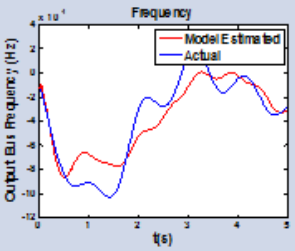	57.9916
3→4	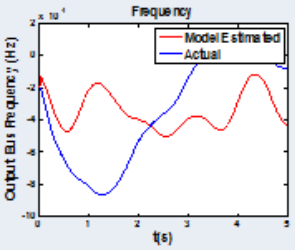	-6.9899
4→5	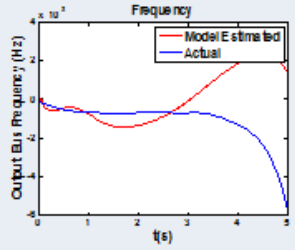	-144.3418

Figure G-2 Frequency Response Estimation Following the Sequence of Disturbances-Adaptive Model

APPENDIX H APPLICATION IN VOLTAGE COLLAPES PREDICTION

Event	Response Comparison	Accuracy Index
1	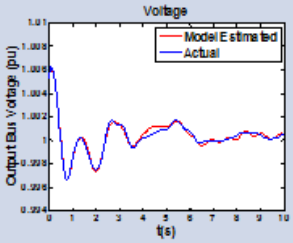	85.9054
2	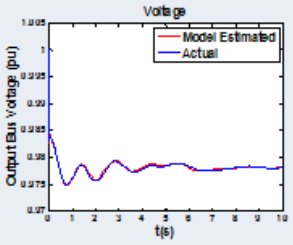	86.8629
3	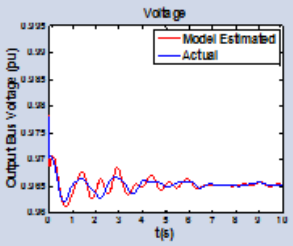	27.0388
4	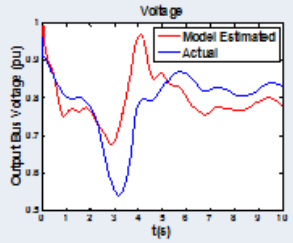	2.5952

Figure H-1 Voltage Response Estimation Following the Sequence of Disturbances-Fixed Model

Event	Response Comparison	Accuracy Index
1→2	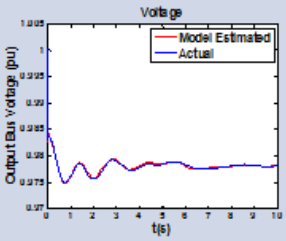	86.8629
2→3	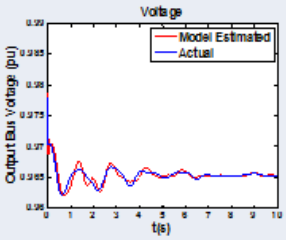	56.0767
3→4	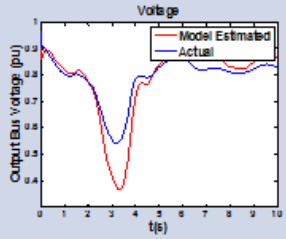	26.4890

Figure H-2 Voltage Response Estimation Following the Sequence of Disturbances-Adaptive Model

APPENDIX I SOME EI SYSTEM SIMULATION STUDIES

In this appendix, several individual EI system simulation studies will be briefly introduced.

- **Influence of Disturbance Locations on the Inter-area Oscillation**

The FNET inter-area oscillation monitoring since 2005 has demonstrated that the disturbances that occur in different locations may incite the inter-area oscillations with different characteristics. In this section, four generation trips of almost the same capacity were simulated in different regions of the EI system (detailed information given in Table I-1), and the incited inter-area oscillations were plotted in Figure I-1. Note that the frequency deviations from whole system average instead of nominal value were plotted. From Figure I-1, it can be observed that the disturbance that occurred in Tennessee incited much less oscillations than other disturbances, which confirms that it's easier to incite the inter-area oscillation if the disturbance occurs on the edges of bulk power grid. Another phenomenon that should be noticed from the simulation results is that the inter-area oscillations incited by generation trips are usually between the region where the disturbances occur and the rest of the EI. This can also be verified by the FNET measurement.

Table I-1 Generation Trips in Different Regions Used to Incite Inter-area Oscillations

Location	Capacity Tripped
Tennessee	692 MW
Northeast	681 MW
Florida	692 MW
North Dakota	721 MW

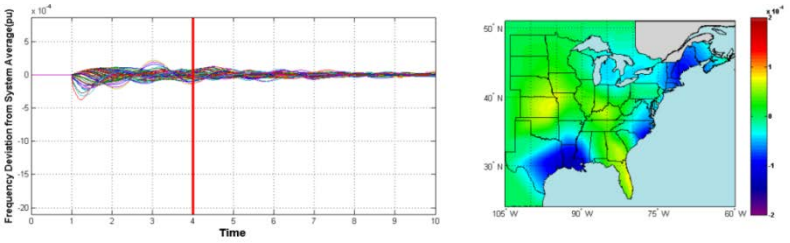

Disturbance Location in TN

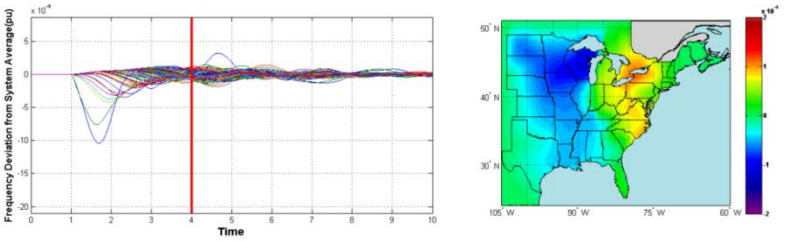

Disturbance Location in Northeast

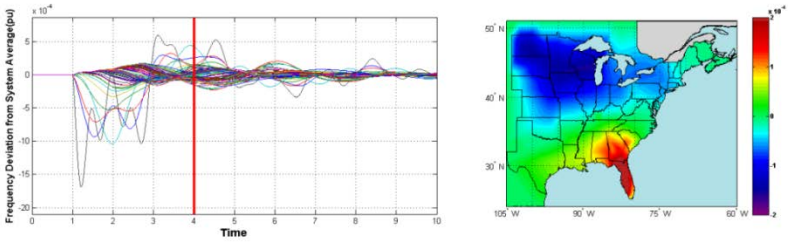

Disturbance in Florida

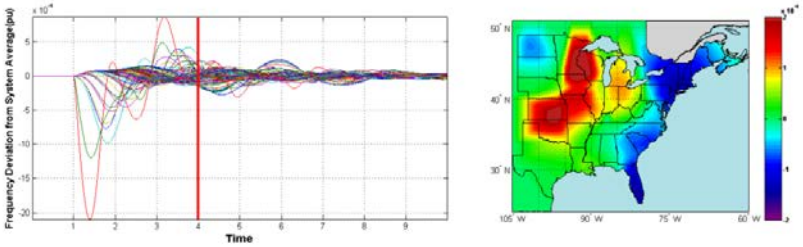

Disturbance in North Dakota

Figure I-1 Inter-area Oscillations in the EI Incited by Disturbances in Different Regions

- **Impact of the Penetration Levels of Renewables on the EI System Frequency and Voltage Response**

Hundreds of technical papers have focused on investigating the impact of renewables on the bulk power grid frequency and voltage response around the world since the very beginning of renewables development and these researches have repeatedly demonstrated that increasing penetration of renewables would change the traditional way of system operation and corresponding regulation policies needs to be modified to address those issues, such as the decrease of frequency and voltage support capabilities. However, up to now, there is no specific simulation study carried out for the EI system yet. Apparently, the lack of the appropriate EI system model (with high penetrations of renewables) is the largest hurdle preventing us from doing that.

However, it's not impossible to investigate this topic without the appropriate EI system model. One of the main differences between renewable and conventional generations is the "hidden" inertia of renewable generations and lack of frequency and voltage support capabilities under current control situations. Therefore, the whole system inertia can be scaled down proportionally and a portion of conventional turbine governors can be disabled to mimic the impact of a desired renewable penetration level on the EI system frequency response. In this way, the influence of different renewable penetration levels on the EI frequency response can be investigated. Similarly, for the voltage response study, a portion of conventional generator exciters can be disabled to mimic the influence of renewables on the voltage response. However, please note that disabling governors/exciters only means those conventional generators would lose frequency and voltage support capabilities and does not mean these generators would behave exactly the same as renewable generators.

An automated Python file is written to mimic the 30%, 40% and 60% three levels of renewable penetration and the simulation results are given below in Figure I-2 and Figure I-3. From the frequency response result, it can be concluded that the increasing penetration level would dramatically deteriorate the frequency response, including the frequency drop rate, frequency drop nadir and steady-state frequency recovery.

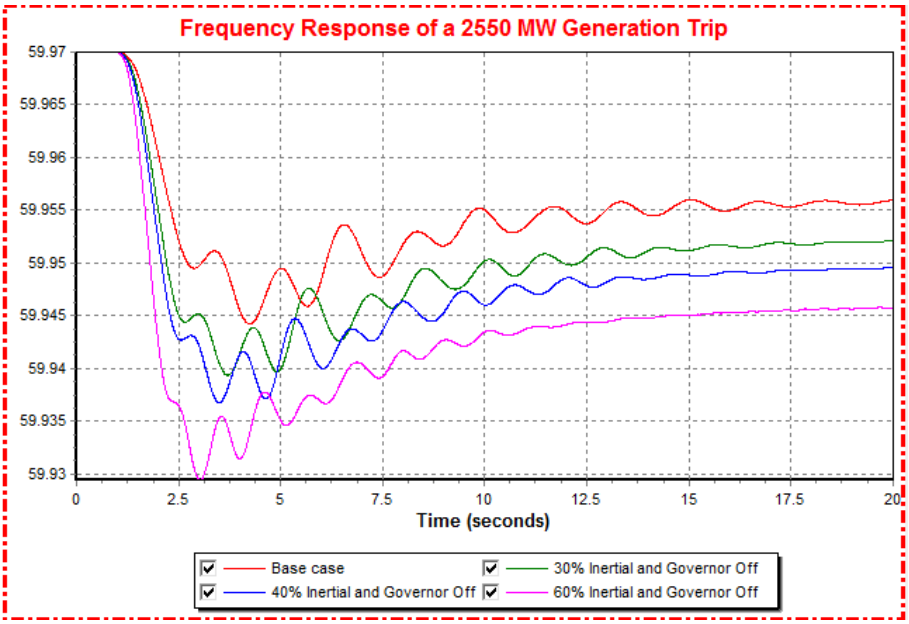

Figure I-2 Frequency Responses of the EI system with Different Penetration Levels of "Fake" Renewables

In the voltage case (Figure I-3), it's also obvious that the increasing penetration level would negatively influence the system voltage response. Please note that the 60% case is already unstable; however, it gives us some hints on how the renewable penetration levels impact the system voltage profile. From the simulation results, current regulation policies need to be modified to improve the system frequency and voltage response.

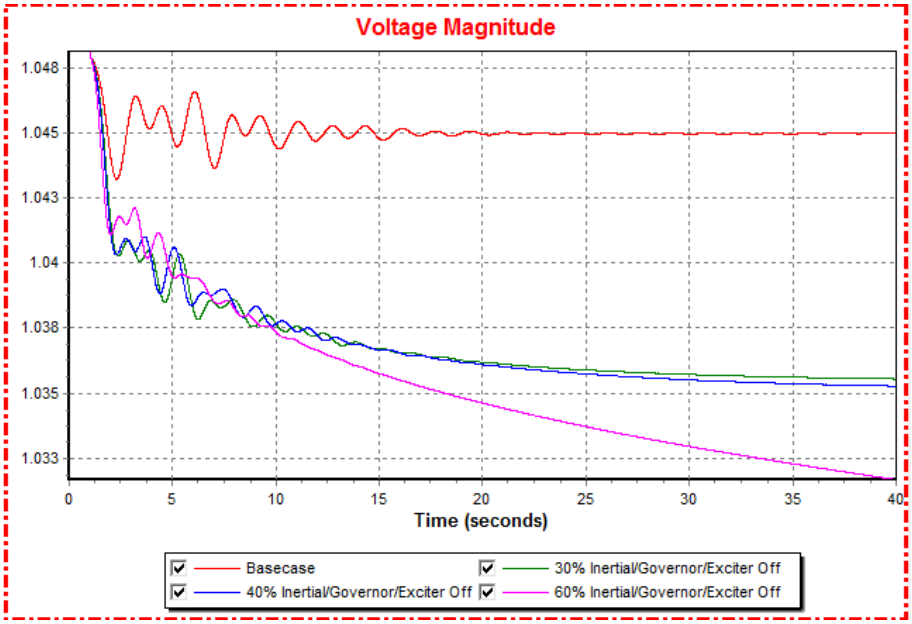

Figure I-3 Voltage Responses of the EI system with Different Penetration Levels of "Fake" Renewables

- **EI Model Validation Using FNET Measurement Data**

FNET-based model validation is an attempt to correct frequency response from simulations so that the simulation output is close to frequency measurement obtained from system events. Practically, model validation also needs to be periodically performed to ensure that system models are updated along with system changes. This section continues the FNET-aided model validation work by giving two more recent case studies.

- Case 1: The two nuclear reactors at North Anna Power Station (about 1800MW) in Mineral, Va., automatically shut down following a 5.8 magnitude earthquake in Central Virginia on Aug. 23, 2011, at 1:51 p.m. ET.

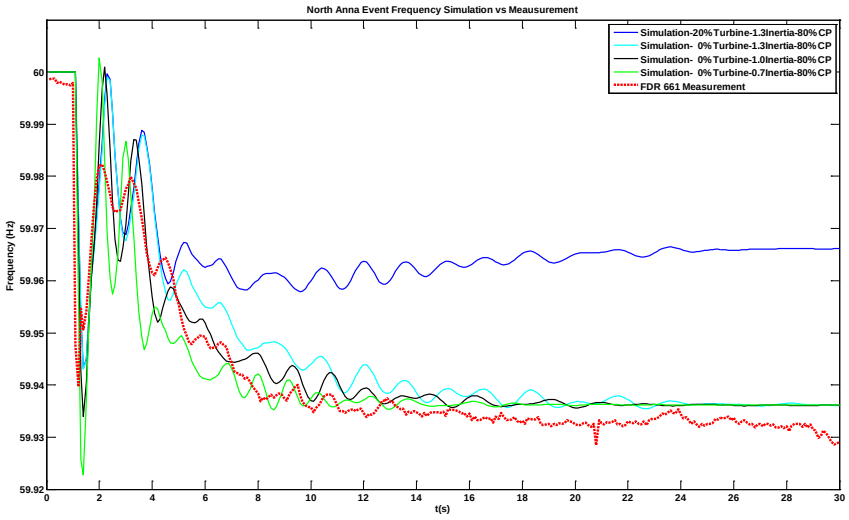

Figure I-4 16,000-bus EI Model Validation Using FNET Measurement Data-North Anna Event

To make the simulation result match the real frequency response, system inertial, governors, and load composition were carefully tuned. In this specific case, it turns out that disabling all the governors, scaling up the system inertia by 30%, and using 80% constant active power and 20% constant current power for the load composition gives the best match (as shown by Figure I-4).

- Case 2: Severe storms moving through the Southeast dealt a severe blow to the Tennessee Valley Authority on April 27, 2011, knocking out 11 high-voltage power lines in Mississippi and north Alabama.

To make the simulation result match the real frequency response of this TVA line trip case, it seems that disabling 80% of the governors, scaling down the system inertia by 30%, and using 80% constant active power and 20% constant current power for the load composition would give the best match (Figure I-5). From these two case studies, it tells

that, the system model validation process may need to be done periodically and the system-level tuning process may also have its limitations.

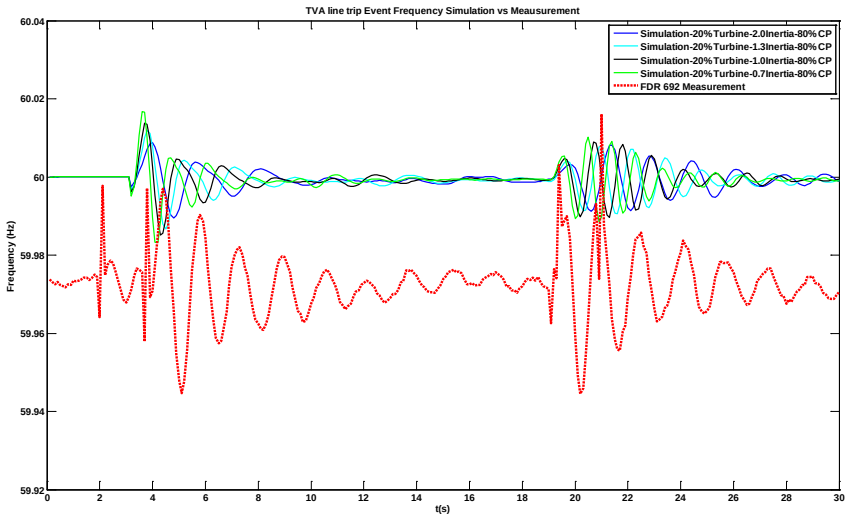

Figure I-5 16,000-bus EI Model Validation Using FNET Measurement Data-TVA Line Trip Event

VITA

Yong Liu received his B.S. and M.S. in electrical engineering from Shandong University in 2007 and 2010, respectively. He started his Ph. D study at the University of Tennessee, Knoxville, in August 2010 and his current research interests involve synchrophasor applications, renewable energy integration and power system dynamic analysis.